



Laser-Based Flowfield Imaging in a Lean Premixed Prevaporized Sector Combustor

Yolanda R. Hicks
Glenn Research Center, Cleveland, Ohio

Randy J. Locke
NYMA, Inc., Brook Park, Ohio

Robert C. Anderson
Glenn Research Center, Cleveland, Ohio

The NASA STI Program Office . . . in Profile

Since its founding, NASA has been dedicated to the advancement of aeronautics and space science. The NASA Scientific and Technical Information (STI) Program Office plays a key part in helping NASA maintain this important role.

The NASA STI Program Office is operated by Langley Research Center, the Lead Center for NASA's scientific and technical information. The NASA STI Program Office provides access to the NASA STI Database, the largest collection of aeronautical and space science STI in the world. The Program Office is also NASA's institutional mechanism for disseminating the results of its research and development activities. These results are published by NASA in the NASA STI Report Series, which includes the following report types:

- **TECHNICAL PUBLICATION.** Reports of completed research or a major significant phase of research that present the results of NASA programs and include extensive data or theoretical analysis. Includes compilations of significant scientific and technical data and information deemed to be of continuing reference value. NASA's counterpart of peer-reviewed formal professional papers but has less stringent limitations on manuscript length and extent of graphic presentations.
- **TECHNICAL MEMORANDUM.** Scientific and technical findings that are preliminary or of specialized interest, e.g., quick release reports, working papers, and bibliographies that contain minimal annotation. Does not contain extensive analysis.
- **CONTRACTOR REPORT.** Scientific and technical findings by NASA-sponsored contractors and grantees.

- **CONFERENCE PUBLICATION.** Collected papers from scientific and technical conferences, symposia, seminars, or other meetings sponsored or cosponsored by NASA.
- **SPECIAL PUBLICATION.** Scientific, technical, or historical information from NASA programs, projects, and missions, often concerned with subjects having substantial public interest.
- **TECHNICAL TRANSLATION.** English-language translations of foreign scientific and technical material pertinent to NASA's mission.

Specialized services that complement the STI Program Office's diverse offerings include creating custom thesauri, building customized databases, organizing and publishing research results . . . even providing videos.

For more information about the NASA STI Program Office, see the following:

- Access the NASA STI Program Home Page at <http://www.sti.nasa.gov>
- E-mail your question via the Internet to help@sti.nasa.gov
- Fax your question to the NASA Access Help Desk at 301-621-0134
- Telephone the NASA Access Help Desk at 301-621-0390
- Write to:
NASA Access Help Desk
NASA Center for Aerospace Information
7121 Standard Drive
Hanover, MD 21076



Laser-Based Flowfield Imaging in a Lean Premixed Prevaporized Sector Combustor

Yolanda R. Hicks
Glenn Research Center, Cleveland, Ohio

Randy J. Locke
NYMA, Inc., Brook Park, Ohio

Robert C. Anderson
Glenn Research Center, Cleveland, Ohio

National Aeronautics and
Space Administration

Glenn Research Center

Acknowledgments

The authors wish to thank Robert Tacina, John Deur, and Michelle Zaller for technical information, Kelly Ockunzzi for technical assistance, and the facility operations engineers and technicians: C. Joe Morgan, Dean Kocan, Wade Arida, Jeff Bobonik, Bob McCluskey, Ray Williams, Al Studnika, and Kevin Roberts.

Document History

This research was originally published internally as HSR051 in February 1997.

Note that at the time of writing, the NASA Lewis Research Center was undergoing a name change to the NASA John H. Glenn Research Center at Lewis Field. Both names may appear in this report.

Available from

NASA Center for Aerospace Information
7121 Standard Drive
Hanover, MD 21076

National Technical Information Service
5285 Port Royal Road
Springfield, VA 22100

Available electronically at <http://gltrs.grc.nasa.gov>

Laser-Based Flowfield Imaging in a Lean Premixed Prevaporized Sector Combustor

Yolanda R. Hicks
National Aeronautics and Space Administration
Glenn Research Center
Cleveland, Ohio 44135

Randy J. Locke
NYMA, Inc.
Brook Park, Ohio 44142

Robert C. Anderson
National Aeronautics and Space Administration
Glenn Research Center
Cleveland, Ohio 44135

Abstract

OH and fuel planar laser-induced fluorescence (PLIF) is used qualitatively in this study to observe the flame structure resultant from different fuel injector dome configurations within the 3-cup sector combustor test rig. The fluorescence images are compared with some computational fluid dynamics (CFD) results. Interferences in obtaining OH fluorescence signals due to the emission of other species are assessed. NO PLIF images are presented and compared to gas analysis results. The comparison shows that PLIF NO can be an excellent method for measuring NO in the flame. Additionally, we present flow visualization of the molecular species C_2 .

Introduction

The 3-cup sector combustor was tested at NASA Glenn in conjunction with a larger 5-cup sector at GE Evendale. The tests were used to assess the performance in relation to emission requirements for the HSR program. The 3-cup sector is the first to be examined at expected HSR conditions using advanced optical diagnostic techniques in addition to standard gas sampling. This lean premixed prevaporized (LPP) concept combines integrated mixer flameholders (IMFH) with cyclone injectors which are used as pilots.

To aid in the design and to provide a better understanding of phenomena within the combustor, measurements were necessary which could provide a clear visualization of the fuel injection, mixing and combustion processes occurring in the flow field. Such measurements are precluded by standard diagnostic methods such as gas extraction probes and thermocouples, which are limited to pointwise measurements. Of the numerous optical, non-intrusive diagnostic techniques available, only PLIF provides the degree of quantification and two-dimensionality required to evaluate this type of flowfield.

Previous results from flame tube studies using LDI injection (refs. 1 and 2) have shown that OH PLIF can be very useful as an effective two dimensional visualization tool for examining flow uniformity and mixing. The OH radical indicates combustion reactions and is also a relative indicator of temperature. This paper presents an extension of that earlier work to the 3-cup sector.

Our purpose was to establish the efficacy of PLIF as a diagnostic tool for evaluating species, temperature, mixing and other reacting flowfield parameters. Comparisons of the PLIF data with gas

analysis and CFD combustor modeling are used to demonstrate the strengths and validity of PLIF as a valuable diagnostic. Detailed analysis of the OH PLIF data is used to discern trends dependent on the inlet parameters and upon injector configuration. Such analysis should prove useful for fuel injector design, performance analysis, and flame code validation.

A final goal of this study was to assess the applicability of the PLIF technique to the imaging of NO in this environment. NO PLIF measurements have never before been attempted in realistic, multi-component, liquid-fueled hydrocarbon flames at high pressure. Previous laser-induced fluorescence (LIF) measurements (ref. 3) made in diffusion flames at 14 atm established a detection limit for NO of ~1 ppm for this single point measurement technique. Recently, PLIF of NO has been successfully used at 10 atm in small flat flame laboratory burners (refs. 4 and 5) using gaseous fuels. We present the first images of NO in the sector and compare those PLIF results with the corresponding NO_x gas sample data.

We present here the first detailed account of an advanced optical diagnostic investigation of the 3-cup sector at HSR conditions.

Experimental Apparatus

Test Hardware

Figure 1 shows a schematic drawing of the sector shell. The housing is water-cooled and the liner is made by casting a ceramic material, Greencast 94+. Rather than using a true arc, this sector has a rectangular flow path that measures 8.5 in. by 8.5 in. Within this area, three fuel injector domes are fitted. The outer domes (top and bottom) are composed of two rows of IMFH injectors. The center dome can be either another IMFH dome or a pilot dome consisting of one row of three cyclone injectors (3-cup). The center dome may be positioned with varying upstream offset relative to the top and bottom domes. Downstream of the windows, the chamber necks down to an exhaust area that measures 4 in. high by 8 in. wide, as illustrated in figure 1. The exhaust is water-quenched to cool the gas stream to below 140 °F.

The window assemblies (one is shown in fig. 2 with a metal plug) are designed to safely withstand flame temperatures up to 3200 °F and rig pressures up to 20.5 atm. The design limits the maximum ignition thermal cycle (in order to avoid window fracture) to a ΔT of 1600 °F, from an inlet temperature of 1100 °F to an ignition temperature of 2700 °F. Water cooling and nitrogen film cooling are used to ensure that the windows can survive this severe environment. Metal plugs instrumented with thermocouples are used initially in place of the windows to determine the appropriate cooling flows for the windows within the test parameters. Through use of the plugs, we found that the total nitrogen film cooling mechanism for safe operation of the four windows provides no more than 12.5 percent of the aggregate mass flow rate through the shell. The window assemblies are designed so that, other than the small offset (approximately 0.14 in.) to accommodate the nitrogen film cooling, the windows are flush with the hot gases that pass by. The windows are made of ultraviolet grade synthetic fused silica and measure 1.5 in. (38 mm) in the axial direction, 2.0 in. (50.8mm) in the direction perpendicular to the rig centerline, and are 0.5 in. thick (12.7 mm).


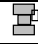


The window assemblies are located so that the exit plane of the top dome can be seen. The top and bottom windows are centered on their respective sides. The two side windows are offset from the center by 1 in., so that the field of view encompasses the intermediate region between the top and middle domes. Radially mounted gas sampling probes are located 5 in. downstream from the window trailing edge. Figure 3 shows the configuration of the windows and the gas sampling probes.

Four different fuel injection configurations were tested: two with a center IMFH dome, one in the upstream (stepped) and one in the downstream position, “flush” with the upper and lower domes; and two with a center pilot cyclone dome, one in the upstream and one in the downstream position. The top and bottom domes were always in the downstream position with their exit plane projecting into the field of

view of the window through which light is collected, 90° from the laser input window. The bottom dome is not in the field of view. The exit plane of the center dome in its upstream position was approximately 1.8 in. ahead of the exit plane of the outer domes; in its downstream position, the center dome exit plane was approximately 0.7 in. ahead of that of the outer domes. The four configurations are listed in table 1 and figures 4 - 6 illustrate the hardware. Both the IMFH and cyclone injectors are designed to be LPP. The standard configuration, A, uses the cyclone injectors. Staged operation uses the cyclone injectors as the pilot, which is always on; the IMFH domes are brought on-line as the power level increases.

Figures 4 and 5 show upstream-looking views of the stepped domes with either a pilot cyclone or an IMFH dome in the center. In each, the approximate field of view is overlaid; it shows the area accessible to the laser systems when two adjacent windows are used. The area measures 2 in. by 2 in. The actual images are slightly larger; their size depends on the position of the collection optics and the distance of the optics from the imaged area. Figure 6 shows a view looking slightly upstream through a side port. A rectangular box is overlaid showing the approximate window position. The overlay shows that the top dome projects into the window's field of view.

TABLE 1.—FUEL INJECTOR DOME CONFIGURATIONS USED IN THE SECTOR TESTS.

Combustor Configuration	Center Dome/Position
A: 3-cup stepped	Pilot/Upstream 
B: 3-cup "flush"	Pilot/Downstream 
C: Triple IMFH stepped	IMFH/Upstream 
D: Triple IMFH "flush"	IMFH/Downstream 

Laser Diagnostics Facility

The laser system used for acquiring the PLIF images consists of a Continuum Nd:YAG-pumped (NY-81C) dye laser (ND60) with ultraviolet wavelength extension (UVX). The Nd:YAG laser 2nd harmonics provides approximately 750 mJ/pulse at 10 Hz. The dye laser, using Rhodamine 590 (R-590) dye, produces pulses of 180 mJ at 564 nm. The dye laser output was doubled to provide the desired UV 283 nm wavelength at ~16 mJ/pulse for OH excitation. In order to achieve the shorter UV wavelengths necessary for exciting NO electronic absorption transitions, 80 parts of R-590 dye solution were mixed with 20 parts of R-610 dye solution. The doubled dye output was then mixed with the residual Nd:YAG infrared ($\lambda = 1064$ nm) to provide wavelengths around 225.5 nm at ~4 mJ/pulse for NO excitation. The UV wavelengths used in this study possessed bandwidths of 1.0 cm^{-1} , as measured by a Burleigh UV pulsed wavemeter. The UV light was separated from the residual dye and fundamental light output by a pellin-broca prism. The desired transition was verified by directing the laser beam through the flame of a Bunsen burner at atmospheric pressure for OH, or a high pressure vessel containing 250 ppm of NO, and observing the fluorescence with a photomultiplier boxcar-averager system.

Detectors

The detector used for the PLIF work is a Princeton Instruments gated, intensified charge-coupled device (ICCD) camera with an array size of 384 by 576 pixels. The camera intensifier is synchronously triggered with the laser pulse through a Princeton Instruments FG-100 pulse generator. A Princeton Instruments ST-100 detector controller was used to gate the camera for typical periods of 75 ns. The ICCD camera was also used for visualization of C_2 .

The fluorescence signal normal to the incident excitation sheet was collected through a Nikon 105 mm f/4.5 UV Nikkor lens. Princeton Instrument's WinView software was used to acquire the ICCD

images. Elimination of flame luminosity and scattered laser light for OH was accomplished with a 2 mm thick WG-305 Schott glass filter in combination with a 1 mm thick Schott UG-11 bandpass filter. The UG-11 colored glass filter passes a peak wavelength of 340 nm and has a bandpass from 245 nm to 410 nm. The pair transmits approximately 56 percent of the incident radiation in the band between 310 nm and 320 nm. The bandpass filter also passes light above 650 nm and has a peak transmittance at 720 nm of 0.27. For NO detection, a 2 mm thick narrow band interference filter from Andover (#100FC00-50) was used. It has a peak transmittance of 10 percent at 238 nm with a full width at half maximum (FWHM) of 8.2 nm.

Additionally, a Photometrics Star 1 CCD camera system, with an array of 384 by 576 pixels, was used for visualization of C_2 .

Laser Beam Path, Positioning, and Coordinate Systems

As mentioned previously, the sector is rectangular instead of arced. The rectangular cross section simplifies the implementation of laser diagnostics and makes it easier to change the type and positions of the domes. The coordinates are defined as follows and obey the right-hand rule. Z is the axial direction with higher numbers farther downstream. X is the azimuthal (horizontal) direction with positive x to the left when looking downstream. Y is the radial (vertical) coordinate with positive numbers above the zero position. The zero position for z is the exit plane of the top dome; for x, zero coincides with the rig centerline; and for y, zero is the bottom of the top dome.

The beam path illustrated in figures 7 and 8 uses five or six mirrors (controlled remotely), depending on whether the laser sheet is inserted horizontally or vertically. Mirror 4 sends the beam through a cylindrical lens down to mirror 5, which is the final mirror when the laser sheet passes horizontally through the test rig. When employing a vertical laser sheet, mirror 5 is positioned higher and directs the beam to mirror 6, which is placed directly above the test rig. Mirror 6 directs the beam down through the combustor. The total laser beam path length is 25 meters. Figure 8 sketches the layout of the beam input systems and camera orientation for both horizontal and vertical laser beam insertion.

Mirror 4 is placed on a traversing stage that moves in the streamwise (axial) direction. Mirror 5 traverses streamwise when using the vertically applied laser sheet, and traverses vertically (y) for the horizontally applied sheet. Mirror 6 traverses horizontally (x). Each camera is mounted on a set of stages to allow movement in two or three dimensions. When the laser sheet passes through the combustor horizontally, the camera is mounted above the rig (top view). When the laser sheet is vertical, the camera is mounted on the side (side view). Motion controllers control the movement of all stages. Just after the final mirror, a quartz plate is used to split off approximately 5 percent of the incident laser sheet, which is directed into a laser beam energy profiler, located at the focus of the laser sheet. The beam profiler and imaging cameras have their movement coordinated with laser beam positioning in order to maintain alignment.

Experimental Procedure

The dye laser/UVX system was tuned so that its output was one of six rovibronic resonant transitions (lines) in the OH $A \leftarrow X$ (1,0) band: $R_1(10)$ @ 281.607 nm, $R_1(11)$ @ 281.824 nm, $R_1(12)$ @ 282.055 nm, $Q_1(7)$ @ 283.5, $Q_1(9)$ @, 284.01 nm, and $P_1(8)$ @ 285.67 nm; and one transition in the NO $\gamma(0,0)$ band near 225.4 nm. The OH lines selected were chosen for their low temperature sensitivity, low absorption, and in the case of $P_1(8)$ and $Q_1(9)$, to determine their usefulness for two-line temperature imaging. Earlier studies demonstrated that certain OH lines are susceptible to strong attenuation (by absorption). The absorption of excitation wavelengths is inappropriate in the present study because we would not be able to account for any nonuniformity in the flow; therefore, excitation lines which are uniformly transmitted.

NO excitation wavelengths must be carefully selected to avoid interferences from the O₂ absorption spectrum which overlaps that of NO at elevated pressures.

In all cases, the laser beam was allowed to freely expand through the beam transport system (divergence ≈ 5 mrad). The beam was formed into a sheet by passing it through a 50.8 mm square cylindrical lens with focal length 3000 mm, resulting in a sheet with approximate dimensions of 25 mm by 0.3 mm.

The fluorescence from OH or NO was collected using the Princeton Instruments intensified camera system described above. The acquired data consisted primarily of sets of five single-shot images. Some on-chip averages were also collected at selected points. An on-chip average is the integration of the gated fluorescence signal on the CCD array over two or more laser pulses. On-chip averages were of 4 shot, 5 shot, 100 shot, 300 shot, or 600 laser shot duration. The laser sheet was traversed across the combustor typically at nine positions in x or y: 0, ± 5 mm, ± 10 mm, ± 15 mm, and ± 20 mm. The zero position for horizontal laser sheets (y-traversal) is at the interface between the upper and center domes. The zero position for the vertically applied laser sheet (x-traversal) is the plane made by the center of the window and the test rig centerline. The error in positioning the horizontal beam is ± 1 mm; for the vertically applied beam the error in positioning is ± 2 mm.

Table 2 lists the typical rig operating conditions. The inlet temperature ranged from 870 to 1060 °F, the inlet pressure from 8 atm to 14.3 atm, and the equivalence ratio, ϕ , from 0.44 to 0.57, to produce flame temperatures from 2600 to 3200 °F. The air flow rates ranged from 4.1 lb/s up to 9.0 lb/s. The rig was operated using JP-5 fuel.

TABLE 2.—TYPICAL TEST RIG OPERATING CONDITIONS.

Nominal Inlet Temperature, °F	Inlet Pressure, atm	Equivalence Ratio (ϕ)
1060	8.0, 9.0, 10.3	0.44, 0.50, 0.54, 0.57
950	8.0, 9.0, 10.3	0.44, 0.50, 0.54, 0.57
870	9.0, 10.3, 12.0 14.3	0.44, 0.49, 0.51, 0.57

A complete experimental run in which all data points were taken included five hours of actual burning. Some tests were incomplete because of technical facility delays in getting started, shutdowns triggered by high temperature readings on the windows, or other systems failures. One test run was aborted shortly after lightoff because of a building-wide power failure.

Beam alignment was monitored through the use of video cameras to observe the beam location on key mirrors. By covering each mirror mount with white paper, which visibly fluoresces when the laser beam strikes it, we were able to judge if the laser beam moved off the mirror surface. A beam profiler was also used to monitor the laser sheet location.

Image Analysis

Standard procedures for handling images include subtracting the background, removing noise spikes, scaling, and standardizing the image display. Only the scaling procedure is described here.

Intra-image scaling is used to highlight the low-level features within an image. The user defines a sub-region within the overall image. The small region is then scaled based on its maximum and minimum values (self-scaled). The outside region is then scaled so that its maximum value is the same as the maximum value of the sub-region. Figure 9 shows an example of this process. The image on the left is the unprocessed image. The only discernible aspect to the image is the yellow, blue, and green-colored structure at the top of the image. No other structure is visible. The image on the right is the same image after it has been processed through intra-image scaling. Distinct structure is now observable in the lower part of the image.

Some images are displayed so that they all have the same scale. They are scaled based on the lowest and highest values found among all of the images to be displayed.

Results and Discussion

In all images, the direction of flow is left to right. As a reminder, figure 10 sketches the region in the sector that is accessible to the optical systems, detailing the field of view and the laser sheet positions that were used. For figures that show a sequence of traversed positions, the images are laid out so that the position -20 is at the upper left, 0 is in the center, and $+20$ is at the bottom right. Figure 11 is a template displaying the layout of laser sheet positions for both horizontal and vertical laser sheet implementation; the direction the laser travels; and the coordinates x , y , and z . The figures that show image sequences are displayed in two forms. One format displays the sequence so that all images have the same scale, which allows one to observe variation with position. The second format displays each image self-scaled, which emphasizes the structure at each location.

The color bar on the left side of each set of images shows the relative scale from low (bottom of bar) to high (top). The bar contains 25 colors plus black and white, and represents a total span in signal from 0 counts to 255 counts. Black represents the lowest 2 counts (0 and 1), white the highest 3 counts (253, 254, 255). Each color represents a span of 10 counts, or 4 percent, of the total range within that image or set of images that corresponds to the color bar.

The field of view for the images is approximately 1.8 in. (46 mm) in the axial direction and 2.7 in. (69 mm) in the direction normal to the rig axis. The actual dimensions vary because the camera cannot be precisely repositioned the same distance away from the focal plane once the setup is torn down. Also, recall from figure 10 that the top dome overlaps the window's leading edge by approximately 0.5 in., so that the laser sheet does not fill the entire field of view; therefore the left side of the images does not reveal any flow structure generated by PLIF.

All images are compared qualitatively for several reasons. First, signal strength cannot be calibrated easily without a precisely known reference. Second, it is not always possible to generate the same inlet conditions from day to day, particularly at the highest inlet temperature. On any given run day, initial air temperature, heat losses in the facility, and the operations of other facilities can affect the maximum inlet temperature measured immediately upstream of the domes. Third, the center pilot and premixer domes have different areas. The area of the IMFH center dome is larger than that of the pilot by a factor of about 1.1, thus requiring (in order to maintain ΔP) higher air and fuel flow rates, increasing the OH number density. Finally, the quality of the laser sheet varies on a day-to-day basis, especially in terms of streamwise positioning of the beam.

Although several OH excitation lines were used in this effort, for the purposes of this discussion, the particular line selected is not important; we provide the specific line only for completeness in conveying the results.

The limited space and access within the facility means that the optics cannot be set up permanently in the test cell. Any change in test rig hardware (such as a dome change or replacement of a broken window) or a change in laser beam input orientation requires a teardown and rebuildup of the optics. Therefore, the systems are never set up exactly the same way twice. We found during the course of the work that the combustor grows axially about 5 mm between the onset of test rig warm-up through lightoff of the combustor. Thus, traversing stages to position mirrors 4 and 5 are a necessity. Temperature changes within the cell during the warm-up procedure also tended to change the mirror alignment, so that minor adjustments were needed to maintain alignment within the combustor.

The windows survived the test runs in good shape, often acquiring a thin coating of fuel or other deposits but generally acceptable to run again after minor cleaning. Some windows did crack, but the cracks occurred after a test, presumably during rig cool-down. After the first occasion, the cooling water supply to the window assemblies was left on overnight. However, that had no apparent effect. At present, there is no explanation for window cracking upon cool-down. This situation never occurred on the flame tube rig. The best hypothesis for the failures is that the rig does not cool down as uniformly as it warms up, so that tensile stresses are applied to the windows beyond their fracture point.

Effect of Dome Configuration on OH Fluorescence Signal

Figure 12 plots signal strength as a function of position in dome configuration A. In figure 12a, peak signal strength is plotted for vertical laser sheet positions. The fluorescence signal is high when the laser sheet passes through the effluent from LPP injectors and low when it does not. Figure 12b plots the average cross-beam intensity for three horizontal laser sheets. The signal at $y = +20$ is due to fluorescence from the LPP jets. The plots show no loss in image intensity as the fluorescence signal travels through a greater bulk of fluid to reach the camera. For example, the signal that emerges from sheet position $x = -20$ must travel through 40 mm additional fluid than does the signal from $x = +20$ (fig. 12a). Although the signal from the lower horizontal sheet positions ($-y$) are on the order of four to five times less than the uppermost positions, a loss in signal strength is not evident as the fluorescence passes upwards through the LPP jets (fig. 12b). Therefore, it is unlikely that self-absorption via fluorescence trapping occurs for the excitation wavelengths employed in this study.

The profiles shown in figure 12 are typical of all flow conditions in configuration A. Similar results were obtained for configuration B. The following section addresses in further detail the differences we observed in signal strength.

Interferences to the OH Fluorescence Signal

Previous work in a single cup flame tube (refs. 1 and 2) was relatively free from interferences to the OH fluorescence signal, primarily because the interrogated area was well downstream of the primary reaction zone. There was little off-line signal; therefore, we were assured that the observed signal was due to fluorescence from OH. The sector rig, however, focuses on the area immediately downstream of the fuel injector exit plane, and we now see strong interferences to the OH fluorescence signal, primarily in the region near the IMFH injectors.

A possible interference if the flame is highly luminous derives from soot and its precursors: polycyclic or polynuclear aromatic hydrocarbons (PAH). Allen et al. (ref. 6) found PAH to be a major source of interference to the OH fluorescence signal in the sooting zones of high pressure heptane-air spray flames. That study found the signal from flame-generated PAH to be as much as an order of magnitude over the OH signal.

Given that the current data are taken immediately downstream of the injection point in a system (LPP) that theoretically produces very little soot, and that PAH formation within flames generally requires times that are too slow to account for the interferences encountered here, the PAH that we see must be from the fuel itself. JP-5 can contain up to 25 percent aromatics on a volumetric basis (ref. 7), with a large fraction of those being PAH. PAH compounds are broadband absorbers and emitters. For example, naphthalene is a major constituent that absorbs strongly in the region of laser excitation of OH, about 283 nm (ref. 8). It also fluoresces in the region 310 nm to 315 nm, which falls within the OH detection band.

Figure 13 displays graphs showing the relative strength of the peak signal resonant and non-resonant OH excitation at different horizontal laser sheet positions for dome configurations A and B. The laser sheet is directly in line with the effluent from the IMFH injectors at positions $y = +20$ and $y = +15$. The curves clearly show that there is PAH fluorescence interference at those positions. The geometry of the system is such that when the laser sheet is inserted vertically, it can intersect the effluent from an IMFH injector; the signal that results is typified in figure 12a. The region below the jets has signal an order of magnitude less than that of the area near the injectors, as shown in figures 12b and 13. To determine if that low-level signal results from OH, we compared the signal of an off-line image with an on-resonance image. The results of that comparison are displayed in figure 14. The on-line and off-line images have been self-scaled in the sub-region below the jets based on their maximum and minimum values, independent of the entire image. Figure 14 also plots the average on-line and off-line signals over the

entire image (bottom left) and in the sub-region (bottom right) at different laser sheet positions. These data show that the signal in the sub-region below the jets is due to fluorescence from OH because the off-line signal is distinctly smaller than the on-line signal. In systems using triple IMFH domes, configurations C and D, we found no region that was free of laser-induced interferences resultant from aromatics.

As previously stated, in regions not aligned with the premixed injectors, the fluorescence signal is roughly an order of magnitude lower than the off-line signal. This restricted the overall dynamic range of the images for the OH fluorescence signal because the intensifier gain was set low enough to avoid saturation of the detector and was consequently not optimized for the OH signal.

General Characteristics

On the time scale of a single-shot exposure (laser pulse width = 7 ns FWHM, within a gate time of typically 75 ns), the flow is not steady (repeatable). Figure 15 shows two series of five single-shot exposures at different laser sheet positions within the combustor for configuration C. The sheet positions are $y = +20$ and $y = -20$. The time between consecutive exposures is 100 milliseconds, which coincides with the laser repetition rate. As can be seen, images can vary widely from shot to shot.

We determined the number of single shots that should be averaged to produce a representative time-averaged sample by averaging successive shots until there was no change in image structure. Figure 16 shows images at $y = 0$ averaged over 5, 10, 20, 25, and 600 shots, respectively. Figure 17 is a graph showing the average cross-beam intensity in the z direction for each image in figure 16. A 600 shot average results from data collection over a one minute time window and can be considered an average sample. The graph in figure 17 illustrates that a twenty-five shot average is enough to provide a representative sample.

While twenty-five shots is adequate for a representative average throughout the span of locations sampled, the number of shots required can depend on the beam position. For example, when the laser sheet is positioned so that it intersects the effluent of an IMFH injector, fewer shots are required to interpret the flow structure. Figure 18 shows that only five shots are needed. Although the magnitude of the peaks is different between 5 shots and 300 shots, the trends are identical. This effect is primarily attributable to a lack of mixing of the jet effluent with its surroundings immediately downstream of the IMFH injectors.

Comparison of Fuel Injector Dome Configurations via OH and PAH Imaging

Figures 19 through 34 show images obtained from the four combustor configurations. Each image consists of a five shot average unless otherwise noted. Common to all configurations are the combusting jets that arise from the fuel/air mixture emerging from the IMFH upper dome. As noted earlier, the predominant signal immediately downstream of the IMFH injectors is due to laser-induced interference arising from PAH. Nonetheless, these images show that the jets do not interact with one another over the distance within the field of view (approximately 1 in.). This observation is important in terms of overall stability for this LPP system. There is no evidence of interaction between IMFH injectors and therefore little probability that instabilities which may develop for one injector will influence adjacent injectors.

Figures 19 through 22 display sets of images obtained using dome configuration A (pilot upstream), with $\phi = 0.44, 0.50, 0.54$, and 0.57 . The inlet temperature and pressure are 1040 °F and 9 atm, and the laser sheet is inserted horizontally. Resonant excitation is $R_1(10)$. Via PAH fluorescence, the $y = +20$ and $y = +15$ positions show the structure of the IMFH jets as they emerge from the dome. As the laser sheet is moved down to $y = +10$, lower fluorescence signal and a more uniform distribution is observable, indicating that the laser sheet is no longer directly in line with the IMFH injectors and that we are imaging

OH. All positions at $y = +5$ and below display a fairly uniform distribution of OH, with increasing uniformity as the equivalence ratio is increased. Figure 23 shows data obtained using a vertical sheet and $R_1(10)$ resonant excitation. $T_3 = 1040$ °F, $P_3 = 9$ atm, and $\phi = 0.44$. In the interface region between the top IMFH and center pilot domes, the OH concentration increases with height in the combustor. This trend may be the result of buoyancy within the combustor, inefficient mechanical distribution of the fuel and air, or may occur from expansion into the larger volume just beyond the top and bottom domes.

Further experiments are required to explain these trends. Analytical work (ref. 9) suggests that buoyancy is minimal, because the axial velocities are higher than any gravitational effect could overcome. Experimentally, the thermocouple readings from the instrumented window plugs show higher temperatures on the top plug than on the bottom plug. As mentioned earlier, OH PLIF measurements can provide a relative indication of temperature variations. Thus far, the OH PLIF data tentatively supports the thermocouple readings. The interface region between the middle and bottom domes becomes optically accessible by rotating the combustor housing 180 degrees. This access would then allow a study to be performed which can help to determine the factors important in trends we see.

Figures 24 through 27 show images obtained with dome configuration B (pilot downstream) at $T_3 = 1023$ °F and $P_3 = 9$ atm, using a horizontal laser sheet with resonant excitation of $R_1(12)$. The equivalence ratios are $\phi = 0.44, 0.50, 0.54$, and 0.57 . Distinct jets can be seen at the $y = +20$ and $y = +15$ positions. While there remains strong evidence of the jets at the $y = +10$ position, additional signal is present on the $-x$ side of the images, probably due to pilot interaction at this point. At $y = +5$, the strongest OH signal is on the $-x$ side of the images for all equivalence ratios above $\phi = 0.44$; at $\phi = 0.44$, presence of the premixing jets is still evident. The $y = 0$ plane is similar to the $y = +5$ position, but appears more uniform overall. At the $y = -5$ position, with $\phi = 0.44$, distinct structure can be seen (indicated by the diagonally-running streaks of high intensity), which may be an indicator of the direction of air swirl from the pilot. The other equivalence ratio cases in this plane indicate a more uniform distribution of OH. The $y = -10$ and $y = -15$ planes are very similar overall to the preceding sheet location.

Figure 28 is typical of all sets in dome configuration B taken at $T_3 = 928$ °F and $P_3 = 8$ atm. The equivalence ratio is 0.50 . Again, resonant excitation is $R_1(12)$. The $y = +10$ position shows clearly two distinct jets. Note that at the higher inlet temperature just described, the IMFH jets could be seen at $y = +10$, but there was interaction with the pilot. The lowest inlet temperature ($T_3 = 850$ °F) also produced images similar to those seen in figure 28.

Our results emphasize the importance of having the ability to shift the domes with respect to the windows, which allows observation of the flame structure farther downstream of the fuel injectors. The ability to traverse the laser beam to different areas in the combustor has similar value, as demonstrated by the images obtained. In comparing dome configurations A and B, the effect of the pilot cyclone injectors on the IMFH injectors is apparent. When the pilot dome is downstream (“flush”) rather than upstream (stepped) in relation to the outer domes, we do not see the pilot’s interaction with the IMFH injectors at the $y = +15$ mm and $+20$ mm positions (e.g., compare figs. 21 and 26). The effect of swirl on the flame structure also becomes clearer when the pilot dome is downstream. We see in configuration B structure that may result from pilot injector swirl at positions $y = +5$ mm and below. Regions of high signal appear as diagonal streaks in dome configuration B, whereas the signals in configuration A are more uniformly distributed. Shifting the domes farther upstream can provide up to 3 additional inches in which to observe flame behavior within the sector.

Configurations C and D utilize the IMFH center dome and the PLIF images suggest that the IMFH injectors do not necessarily behave like “LPP” injectors. In all images, the predominant signal is due to aromatics rather than to OH. The images in figures 29 through 32 are from the combustor operating with the center dome in its upstream position, configuration C, using a horizontal laser sheet and $R_1(12)$ excitation. The inlet temperature and pressure are 1020 °F and 9 atm. The equivalence ratios are $0.44, 0.50, 0.54$, and 0.57 . In all cases, the fluorescence signal becomes more uniform with increasing equivalence ratio. As expected, there is strong signal in the region in front of the jets, including the region

below $y = 0$. In those planes below $y = 0$ (downstream of the center IMFH dome), considerable jet cohesiveness, structure, and PAH signal remain. These images provide further evidence that little interaction occurs between the individual IMFH flames. They also suggest that because such structures are seen approximately 2 in. downstream of the injector exit, this system does not truly premix the fuel and air very well. The images at y positions +5, 0, and -5 correspond to the interface region between the upper and center domes and have generally appeared uniform with this combustor configuration. Although the images are uniform, the signal strength is six to seven times lower when compared to images at other y positions.

The images obtained with a vertical laser sheet display a characteristic not seen in the combustor configurations that used a pilot. Figure 33 is representative. The inlet temperature is 1020 °F, the pressure is 9 atm, and $\phi = 0.53$. Laser excitation is $R_1(12)$. A small area of moderately high intensity appears in red in the center region between the IMFH domes, around the $x = 0$ to $x = -10$ positions. It is possibly a secondary combustion zone resulting from air that leaks in between the top and center domes. Again, regions of high intensity are seen downstream of the center IMFH injectors.

Those images obtained from configuration D (center IMFH dome downstream) with a vertical laser sheet (fig. 34, with $T_3 = 1020$ °F, $P_3 = 9$ atm, $\phi = 0.44$, $Q_1(9)$ resonant excitation, and 300 shot on-chip average) show that the signal resultant from the positions that lie in front of the center dome IMFH injectors ($x = -20$ and $x = -15$) is greater than at positions directly in line with the top dome IMFH injectors ($x = +20$ and $x = +15$). Recall that the area of the center dome is larger than the area of the outer domes. The increased signal from the center reflects a larger absolute number of aromatics because more fuel is injected from the center dome than from the outer domes, which have smaller flow rates.

Comparison of OH and fuel imaging with Analytical Results

Analytical data for the 3-cup stepped configuration, solved using similar inlet conditions, yield results similar to the experimental. Figure 35a is an image taken at $T_3 = 1040$ °F, $P_3 = 9$ atm, $\phi = 0.44$ and $x = -10$. Figures 35b and 35c are the predicted OH and temperature distributions for configuration A at $T_3 = 1100$, $P_3 = 10$ atm, and $\phi = 0.58$. The CFD results are displayed to match the field of view of the fluorescence data. The computational data (ref. 10) confirm that the fluorescence signal that arises from the IMFH injector does not emanate from OH. CFD also verifies that little interaction occurs between the IMFH jet with its immediate surroundings. In fact, the temperature contour suggests that the fuel is being vaporized rather than consumed. Another similarity is that the area of highest OH concentration lies in the region just downstream of the pilot dome. One difference of note is that although the CFD results show the IMFH jet rising as it travels downstream, the experimental data do not. Rather, the jet appears to maintain a parallel course, a pattern that is generally repeated in the experimental data for all configurations and all inlet conditions.

Fuel Distribution from IMFH Injectors

Figures 36 to 45 use fuel fluorescence via PAH to visualize fuel “mass” distribution near the exit of selected IMFH injectors. Fuel is injected into the mixing tube from the top for those IMFH injectors we can observe in the top dome, and is injected from the bottom for the injectors we observe in the center IMFH dome. The images include an overlay that projects the mixer tube boundaries and centerline onto the camera’s field of view. The images are composed of either 5, 100, or 300 shot averages. The images and plots within a figure are displayed on the same scale for direct comparison; however, direct comparisons of signal cannot be compared across figures. The typically red-colored vertical contour seen on the upstream side of the images reflects the laser sheet energy falloff near the boundary of the laser sheet; that also is true on the downstream side in figures 42 and 44. The plots show the average jet

transverse cross section and indicate that the inlet temperature and pressure conditions are the primary determinants of the average cross-sectional distribution.

The 3-cup stepped configuration (A) shows that the fuel mass distribution from top dome injectors falls primarily within the bounds of the mixer tube diameter, with some slight expansion indicated. This is also true for the top dome of the triple IMFH configurations, C and D. However, when the domes are “flush” (configuration B), the images typically show a contraction of the fuel mass distribution, indicating that fuel is being consumed. In no other dome configuration is this effect seen. This difference is probably due to the position of the high-swirl pilot injectors, which in the “flush” configuration, has greater opportunity to interact with the effluent from the LPP injectors.

The mixer tube diameter of the upper dome is 12.7 mm and is 15 mm in the center dome. Unfortunately, we cannot compare directly the effects of mixer tube diameter because the offset between the upper and center domes (0.75 in. in the “flush” configuration) does not provide the ability to observe equivalent distances from the injector exit for each dome. We can say that jets that emanate from the center dome (figs. 40 and 41) show evidence of contraction, signaling the end of the flame front, but re-emphasizing that fuel extends beyond four IMFH tube diameters downstream for the 15 mm diameter injectors.

As indicated in the images showing fuel distribution and in plots of the transverse jet cross sections, the fuel mass in the region immediately downstream of the mixer tube exit is distributed near the mixer tube centerline. These results are qualitatively similar to those obtained within the mixer tube by Santavicca and Steinberger (ref. 10) at The Pennsylvania State University. In their experiments, Santavicca and Steinberger found that the fuel mass within the mixer tube at the tube exit was primarily confined to the central core region around the injector centerline, providing evidence that the NASA PLIF images of the fuel region are not a result of entrained air. Their results were obtained by imaging (within a transparent quartz IMFH mixing tube) the fluorescence from both the fuel vapor and from the exciplex in the liquid fuel. They used tetradecane fuel doped with 1-methylnaphthalene and NNN'-N' tetramethyl P-phenyldiamine and inlet temperatures of 650 and 900 °F, a pressure of 4 atm, air flow rates of 0.049 and 0.063 lb/s, and equivalence ratios of 0.4, 0.5, 0.6, 0.7, and 0.8, with fuel injection from the bottom.

Deur and Kline (ref. 11) used CFD analysis to look at fuel mass distribution within the mixing tube for several fuel and air injection parameters, for inlet conditions of 1100 °F, 11.5 atm, air flow rate of 0.161 lb/s and $\phi = 0.485$. Their study concluded that the majority of fuel is located at the bottom half of the mixer tube (for fuel injected from top to bottom) as the fuel/air mixture exits the injector.

Figure 46 shows a series of x-y plane cross sections (end views) of the IMFH jets as they progress downstream from the top dome in configuration A. The inlet temperature, pressure and equivalence ratio are 1040 °F, 9.2 atm and 0.44. These images were produced using the Flow Analysis Software Toolkit (FAST) developed under NASA Ames contract NAS2-11555. The software is designed for processing and display of the results from CFD computations. It allows the user to input a grid array and then to provide an array of solution values to that grid. Two grids were used for this work. One grid (the CFD grid) defines the flow path of configuration A used in the CFD calculations (ref. 10); the other grid (the IMAGE grid) is a box whose boundary is determined by the dimensions of the PLIF laser sheets used to excite the fuel. In this case, a series of twenty-one images using a vertical laser sheet ($Q_1(7)$ excitation) taken every 2 mm and spanning a distance of 40 mm (from $x = +20$ mm to $x = -20$ mm) was used. An individual image is composed of a 100 shot on-chip average and has a field of view (determined by camera setup calibration images) that measures 66 mm high, with a laser sheet width of 24 mm. Therefore, the bounds of the IMAGE grid measure 24 mm in z, 40 mm in x, and 66 mm in y. In order to ease the processing burden of incorporating 576 by 384 pixel images into the array, by pixel binning we reduced the number of pixels by a factor of 8 to produce images with 72 by 48 pixels. The spacing between points in the IMAGE grid becomes 0.9 mm in the y-z plane and remains 2 mm along x.

Solution values were put only in the IMAGE grid. The solution value in the IMAGE grid for a particular coordinate is the pixel value corresponding to that location in the set of images. The absolute location of the points in the IMAGE grid relative to the CFD grid is determined by matching landmark

points that are known in both grids. The landmark is the upper dome surface; the downstream surface marks $z = 0$ in the axial direction and the upper dome bottom surface is set for $y = 0$ mm in the vertical direction.

The FAST module called SURFER is used to display the IMAGE grid data. The images of figure 46 are constructed by extrapolation using the available data points in the x-y plane to form smoothly colored polygons.

Selected x-y image planes are shown in figure 46, beginning 4.2 mm downstream of the exit plane. Low fuel mass is indicated in blue, high fuel mass in red. The CFD grid that corresponds to the IMFH injector exit plane is overlaid for reference; it specifies the location of the IMFH injectors. The vertical streaks at planes $z = 22.6$ mm and $z = 24.5$ mm result from obscuration of the laser sheet by a protruding thermocouple on the window housing. In the first plane shown, at $z = 4.2$ mm, we see indication of the effects of the dilution holes which are evenly spaced around the circumference of the IMFH mixing tubes and positioned approximately 5 mm upstream of the exit. The dilution holes are indicated by the six regularly spaced indentations about the circumference, which produces a star-shaped image. The circularly symmetric pattern provides further confirmation that the fuel mass is distributed about the centerline, rather than predominantly below the centerline.

While the CFD work of Deur and Kline showed some similarities in fuel distribution, their finding that the fuel mass is predominantly distributed below the IMFH mixer tube centerline and along the lower wall does not agree with experimental findings at Pennsylvania State University or with the present NASA GRC study. The experiments, using 100 laser shot averages, find that the fuel is distributed about the centerline. Images using single laser shots indicate that the fuel can be above, below, or located about the tube walls in any direction.

Possible explanations for the discrepancy between the CFD and the NASA experimental results could be that the mixing rates are different, that the fuel inlet temperature is underpredicted, or that the fuel vaporization rates are higher than expected. There may be significantly more heat transferred to the fuel within the hypodermic-sized fuel tube prior to injection into the mixing tube, resulting in faster vaporization than predicted and in more fuel distributed along the mixer tube centerline. Consider figure 47, which shows fuel PLIF images that compare inlet temperatures of 580 and 1040 °F in dome configuration C (triple IMFH, center upstream) using a vertical laser sheet at 9 atm and $\phi = 0.44$. Although the optical system is not optimized to resolve the small drops that are typically expected from atomizers, about 20 to 30 μm in size, large conglomerates of fuel are clearly evident downstream of the injector exit for $T_3 = 580$ °F. The smallest aggregate of fuel seen in the image is on the order of 400 μm in size. Under the typical inlet temperatures of this study (≥ 870 °F), drops of this size are not expected, nor have they been encountered. For all data taken at $T_3 = 580$ °F, we found that the majority of fuel is distributed well below the mixer tube centerline, which agrees with Deur and Kline's study.

Additional Considerations

Plots of peak signal versus equivalence ratio (fig. 48) show some interesting trends. We expect to see the OH fluorescence signal increase with increasing equivalence ratio for these fuel-lean cases. In general, the data follows that pattern, although the percentage increase is low when compared to the increase based on calculation of the adiabatic equilibrium concentrations. The increase between $\phi = 0.44$ and $\phi = 0.57$ is typically on the order of 150 to 200 percent, versus a 360 to 410 percent theoretical increase. Most of the discrepancy can probably be attributed to pressure effects on the OH fluorescence signal. That type of trend is not necessarily followed, however, for the PAH fluorescence encountered when the laser sheet intersects the IMFH injector effluent. As indicated in the cross sections plotted in the previous section, in some cases, the signal increases with ϕ , and in other cases, the signal decreases as ϕ increases. In still other cases, the tendency is oscillatory. These effects may be a function of chemistry, kinetics, flow phenomena, or some combination of factors. Preliminary comparison of image appearance as a function

only of pressure or temperature does not provide an answer. More detailed analysis is required to explain the observed results. It may also be useful, when conditions are acceptable for the windows, to extend the equivalence ratio range and observe the fluorescence response.

An observation that cannot presently be explained is demonstrated in figure 49, which plots fluorescence signal versus equivalence ratio for two excitation lines, $P_1(8)$ ($\lambda = 285.67$ nm) and $Q_1(9)$ ($\lambda = 284.01$ nm). These data were taken under the same inlet conditions during the same test run and were composed of 100 shot averages. The inlet temperature was 935 °F and the inlet pressure was 8 atm. Both graphs show a drop in signal from $\phi = 0.44$ to $\phi = 0.50$, but from that point they differ. $Q_1(9)$ continues on its downward trend, but the $P_1(8)$ curve reverses and the fluorescence signal begins increasing with ϕ . One possible explanation is that one of the excitation lines is sensitive to temperature, and this sensitivity becomes apparent around the combustion temperature corresponding to $\phi = 0.5$ (flame temperatures are 2890 to 2960 °F for the range of inlet temperature and pressure). Another explanation could be that the $P_1(8)$ line is near the edge of or removed from the absorption region of any of the aromatics in the fuel, whereas the $Q_1(9)$ line is being absorbed by PAH. A third possibility considers chemistry and kinetics in conjunction with temperature and spectral sensitivity. A reaction may have achieved sufficient activation energy at an equivalence ratio of 0.5 to pyrolyze more of the fuel and to promote formation of OH. (This hypothesis would be reflected by the $P_1(8)$ curves.) Another reason may be due to flow phenomena, although this reason seems unlikely, because the data were taken under the same combustion environment with a sufficiently large sample. Further study is needed to explain the differences.

A determination of planar temperature distribution will be attempted by ratioing two OH images obtained at the same position and condition using two different OH excitation transitions. A temperature map is derived from this ratio, which is proportional to the Boltzmann distribution. These images will provide the first ever planar temperature measurement at HSR conditions. Previously, the two-line OH technique has been attempted only on simple 2-component, shock-heated flows at sub-atmospheric pressure (ref. 12) and 2-component flat flames at atmospheric pressure (ref. 13). Due to the many parameters involved and the complexity of both the spectroscopy and flowfield, the data reduction to accomplish this is laborious and time-consuming. Preliminary calculations have indicated that interferences create difficulties that were not encountered in the previous “simple” temperature mapping experiments. However, we are confident that the data collected will allow the first ever successful application of the Boltzmann temperature technique to a realistic HSR-type combustor flowfield.

Nitric Oxide Imaging

Figures 50 and 51 present NO PLIF data from the 3-cup stepped dome configuration. For analysis of the data, we looked only at the region directly downstream of the interface region between the top IMFH and the pilot domes. Our OH PLIF images suggested that this zone is the hottest area in this dome configuration. The images have been averaged by binning groups of 31 by 31 pixels and displaying the average signal for that group. Each image is an on-chip average of 600 shots.

Our NO PLIF measurements were highly successful. Figure 50 shows NO images at each equivalence ratio tested. We saw a drop in fluorescence signal between $\phi = 0.54$ and $\phi = 0.57$, which might be explained by some anomaly in the local flow rates at the time data was taken. This hypothesis is supported by the data, shown in figure 51 acquired coincidentally by the gas sampling probe. Figure 51 compares the gas sampled NO_x signals to the PLIF NO signal. The NO_x gas analysis data tracks nearly point-for-point with the PLIF NO signal, which verifies that PLIF of NO is a viable diagnostic method in this combustion environment.

Only two runs were allowed to acquire all of the data needed to quantify NO. All NO data presented were acquired on the first day. The poor condition of the windows on the second day precluded obtaining the full set of data needed for quantification. NO concentrations ranged from 10 to 100 ppm, as measured by the gas analysis system. The PLIF technique employed here has displayed the capability of easily

imaging NO at these concentration levels and indicates that with additional refining/tuning of the technique, the ability to image much lower concentrations.

Other Flow Visualization Methods

Advantage was taken of spectra emitted by other species in the flame and used to say more about the system than can be explained by OH fluorescence spectroscopy alone. The constituent species examined was C_2 . Most of the visible emission is from C_2 , which has bands from 400 nm to 600 nm (ref. 14). Figure 52 shows images taken at $T_3 = 1040$ °F and $P_3 = 9$ atm for equivalence ratios $\phi = 0.44, 0.49$, and 0.54 using dome configuration A. Light was collected through the $f/4.5$ UV Nikkor lens used for the PLIF images. These images were acquired using the Princeton Instruments ICCD camera without gating. An Andover 488FS03-50 narrowband filter was used, centered at 488.3 nm with a bandwidth of 2.7 nm FWHM. The shutter speed was 5 ms. The camera was oriented to observe the flow near the interface region between the top and center pilot domes, as with vertical PLIF. The images are displayed using 255 shades of orange. The images show an expanding jet emerging from the IMFH dome. While the signal strength increased with ϕ , the relative visibility of the jet decreased. OH images should look similar to the C_2 images in the region near the jet, but the strong signal from PAH probably overcomes the smaller OH signal. Observation of the naturally occurring OH fluorescence in the flame, using a narrowband filter centered around 313 nm, may provide confirmation.

The image shown in figure 53 was taken at $T_3 \approx 855$ °F, $P_3 \approx 9.5$ atm, and $\phi \approx 0.43$. The camera used was the Photometrics Star 1 CCD camera. Again, the lens was the UV Nikkor lens, which was filtered with an Andover 532FS03 narrowband filter centered at $\lambda = 532.4$ nm having a bandwidth of 2.9 nm FWHM. The shutter speed was 100 ms. The image was taken just after lightoff of the combustor. The long exposure allowed observation of the flow from the pilot region as it curled upward in front of the top dome. The C_2 image agrees with the OH PLIF images and the CFD calculations in the region downstream of the pilot dome, reflecting a temperature rise near the bottom edge of the top dome.

Another molecular system that may be useful and that is reasonably accessible includes direct excitation of the C-H bond in the fuel. PLIF of CH would provide images of the fuel-rich side of the flame zone, and can help assess the quality of the premixing within the IMFH dome. CH can be excited in its (0,0) band, at about $\lambda = 428$ nm, with detection around $\lambda = 431$ nm. Alternatively, the naturally occurring fluorescence can be observed, again at around $\lambda = 431$ nm.

Conclusions

This study provides the first images of OH and NO via planar laser-induced fluorescence in the primary combustion zone of a gas turbine sector combustor burning JP-5, simulating a variety of HSR combustor operating points. The OH PLIF allowed us to look at where mixing and combustion occurred. We observed little evidence of mixing with the surroundings near the IMFH injectors.

We have shown that discerning the OH signal from PAH in a “premixed” high pressure flame system is problematic, depending both on the orientation of the laser sheet and on the orientation of the fuel injector domes. When probed close to the premixer exit, the PAH signal exceeded that of OH. However, the PAH also served as a marker of fuel location. We saw that the distribution of fuel leaving an IMFH injector lies about the centerline of the mixer tube, and as we showed in the triple IMFH stepped configuration, a significant amount of nonpyrolyzed PAH exists relatively far downstream of the injection point of the IMFH injectors. In order to assess mixing and to determine the extent to which the PAH exists, further investigation is warranted, with the hardware oriented to position the windows farther downstream of the fuel injectors. Additionally, with further refinement of the technique, this visualization

method may also indicate blockages in IMFH tubes by indicating abnormally low or high fluorescence signals.

We have also shown that NO images can be obtained within this combustion environment. Although further investigation is required to determine the extent to which we can quantify the fluorescence signal and to determine the lower detection limit, the observed trends are in complete agreement with the gas sample data.

References

1. Locke, R.J., Y.R. Hicks, R.C. Anderson, and K.A. Ockunzzi [1996]. "OH Imaging in a Lean Burning High Pressure Combustor," *AIAA Journal*, vol. 34, no. 3, pp. 622–624.
2. Hicks, Y.R., R.J. Locke, R.C. Anderson, and K.A. Ockunzzi [1995]. "Planar Imaging of Hydroxyl in a High Pressure, High Temperature Combustion Facility," *Proc. SPIE* 2546, pp. 465–476; NASA TM-107074, October 1995.
3. Reisel, J.R. and N.M. Laurendeau [1994]. "Laser-Induced Fluorescence Measurements and Modeling of Nitric Oxide in High-Pressure Premixed Flames," NASA Contractor Report 195404.
4. DiRosa, M.D., K.G. Klavuhn, and R.K. Hanson [1995]. "PLIF Imaging of NO and O₂ in High-Pressure Flames," *Proc. SPIE* 2546, pp. 509–518.
5. Battles, B.E., J.M. Seitzman, and R.K. Hanson [1994]. "Quantitative Planar Laser-Induced Fluorescence Imaging of Radical Species in High Pressure Flames," AIAA Paper 94-0229, 32nd Aerospace Sciences Meeting, Reno, NV.
6. Allen, M.G., K.R. McManus, and D.M. Sonnenfroh [1994]. "PLIF Imaging Measurements in High-Pressure Spray Flame Combustion," AIAA Paper 94-2913, 30th AIAA/ASME/SAE/ASEE Joint Propulsion Conference, Indianapolis, IN.
7. Coordinating Research Council, Inc. [1983]. *Handbook of Aviation Fuel Properties*, CRC Report Number 530. Atlanta: Coordinating Research Council.
8. Berlman, I.B. [1971]. *Handbook of Fluorescence Spectra of Aromatic Molecules*, 2nd Ed. New York: Academic Press.
9. Deur, J.M. [1996]. Personal Communication.
10. Santavicca, D.A. and R.L. Steinberger [1994]. Final Report to General Electric Aircraft Engines.
11. Deur, J.M. and M.C. Cline [1996]. "Analysis of Fuel Vaporization, Fuel-Air Mixing, and Combustion in Integrated Mixer-Flame Holders," HSR031, April 1996.
12. Seitzman, J.M., J.L. Palmer, A.L. Antonio, R.K. Hanson, P.A. DeBarber, and C.F. Hess [1993]. "Instantaneous Planar Thermometry of Shock-Heated Flows Using PLIF of OH," AIAA Paper 93-0802, 31st Aerospace Sciences Meeting, Reno, NV.
13. Paul, P.H., U.E. Meier, and R.K. Hanson [1991]. "Single-Shot, Multiple-Camera Planar Laser-Induced Fluorescence Imaging in Gaseous Flows," AIAA Paper 91-0459, 29th Aerospace Sciences Meeting, Reno, NV.
14. Gaydon, A.G. [1948]. *The Spectroscopy of Flames*, New York: John Wiley & Sons.

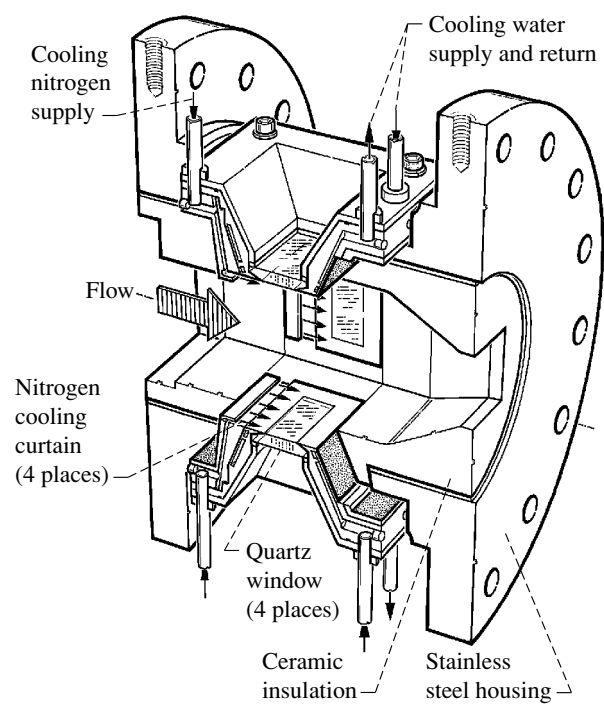


Figure 1. Sector combustion shell with quartz window assemblies.

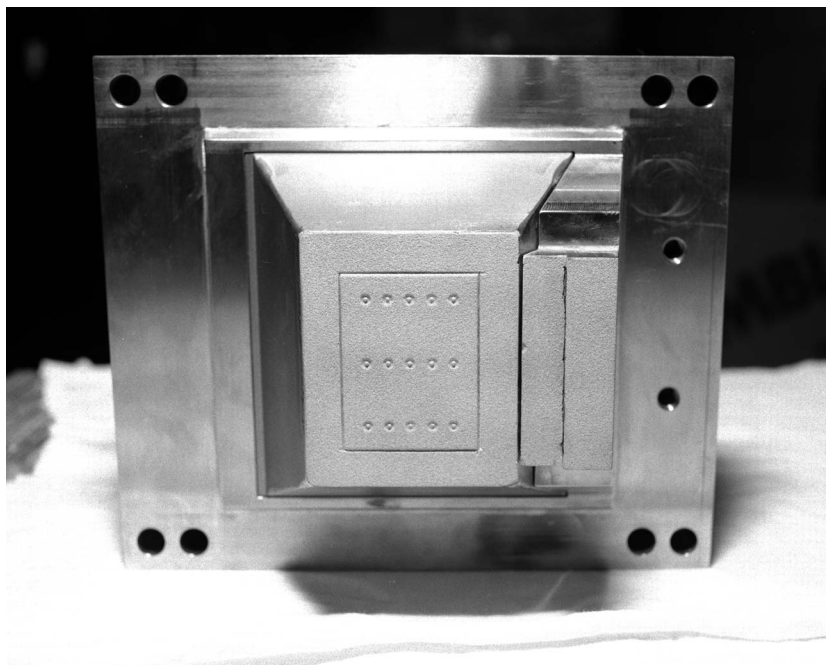


Figure 2. A window assembly which has a metal plug installed. The plug is instrumented with fifteen thermocouples.



Figure 3. Downstream - looking view of the sector combustor shell, showing the arrangement of the windows and of the gas sample probes.

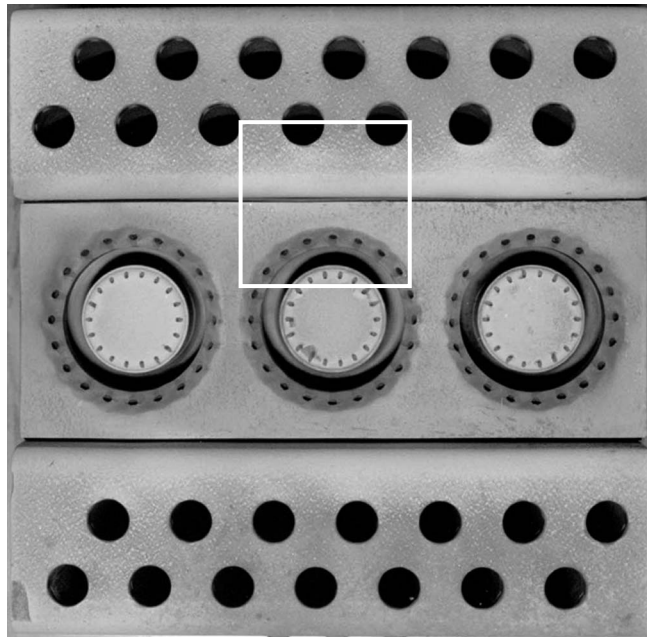


Figure 4. End view of the 3-cup flush configuration, B. Overlaid is the region accessible to the laser systems. These domes are also used in the 3-cup stepped dome configuration, A.

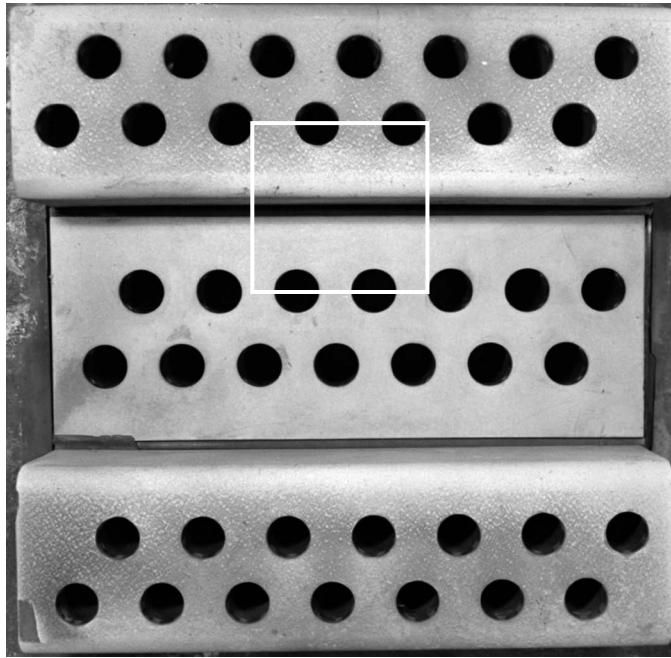


Figure 5. End view of the triple IMFH stepped dome configuration, C. Overlaid is the region accessible to the laser systems. These domes are also used in the triple IMFH "flush" configuration, D.

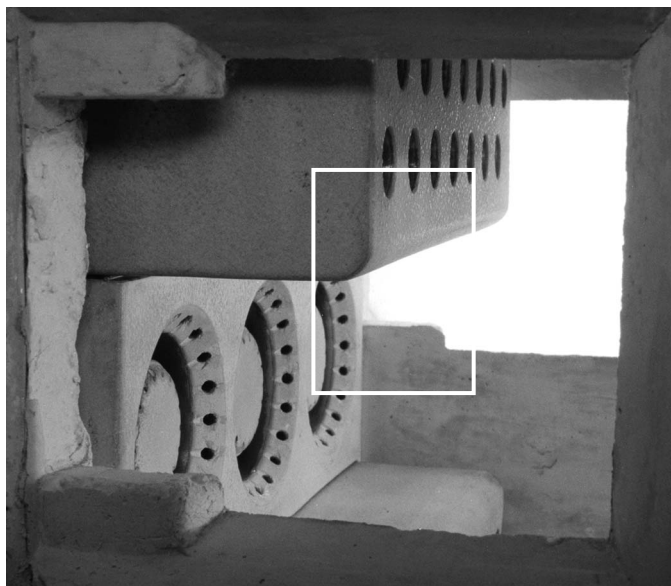


Figure 6. Off-angle view through a side window port with overlay of approximate window position.

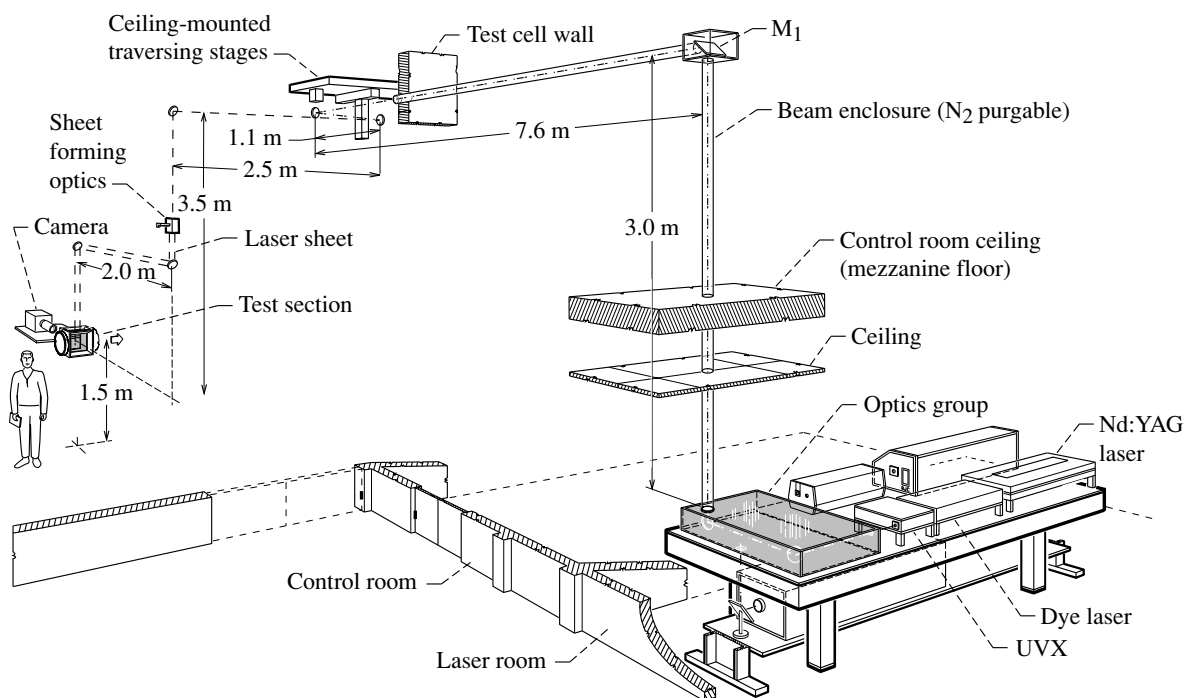
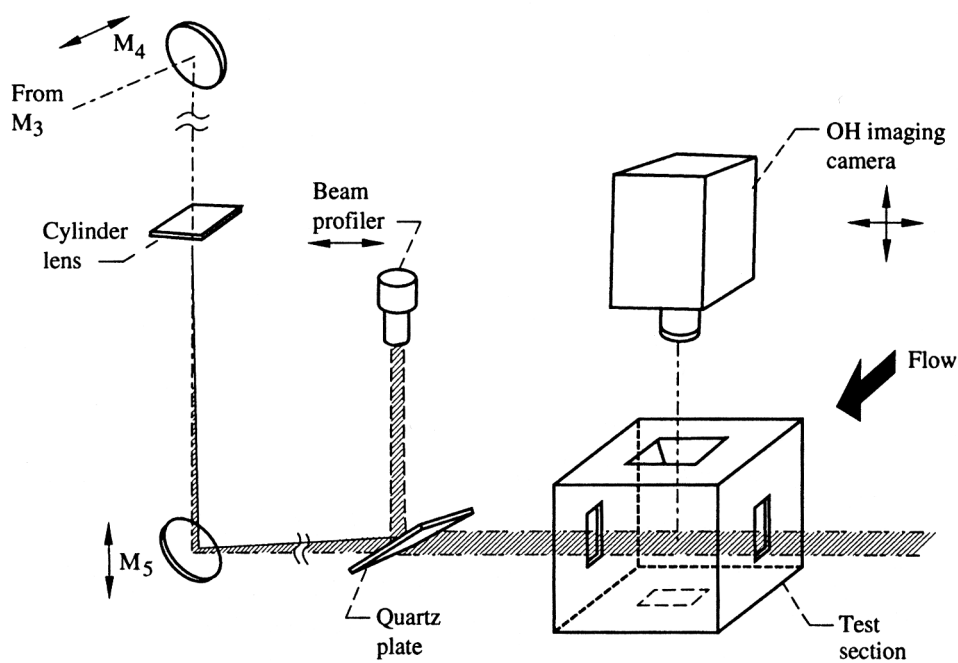
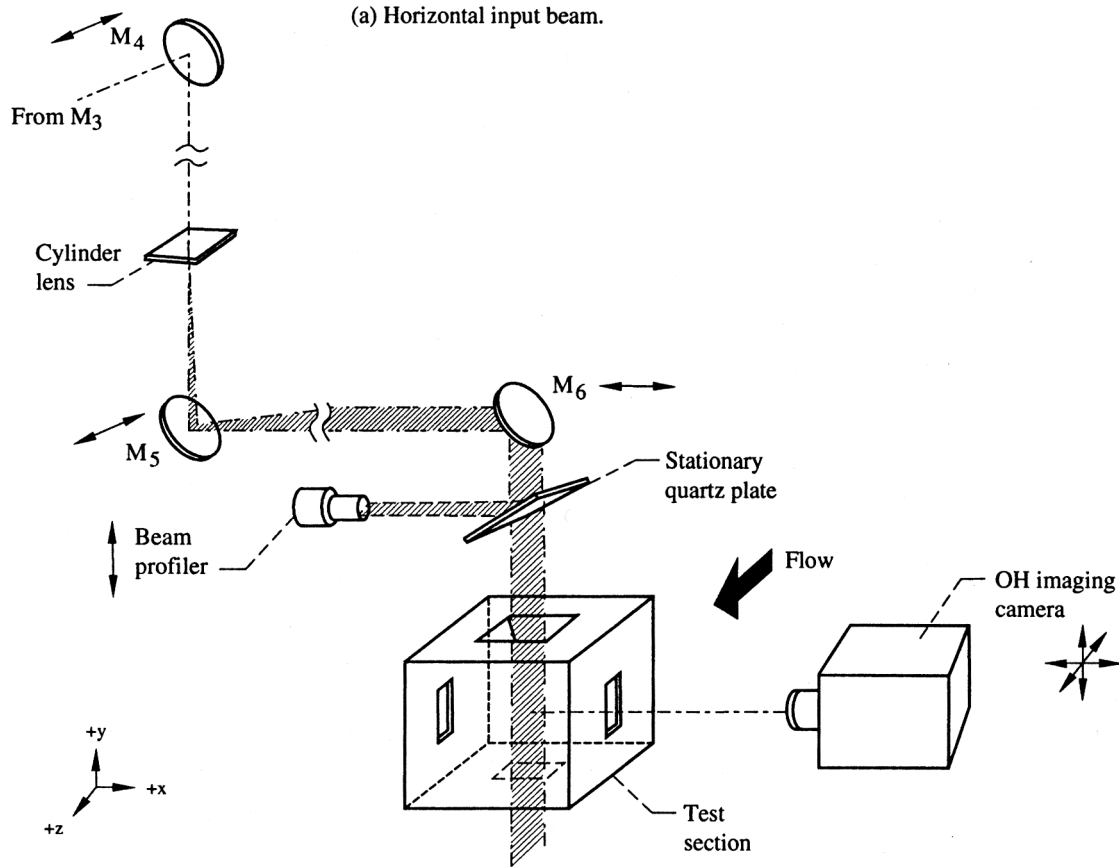


Figure 7. Laser beam path to sector test rig.



(a) Horizontal input beam.



(b) Vertical input beam.

Figure 8. Laser sheet implementation and camera configurations.

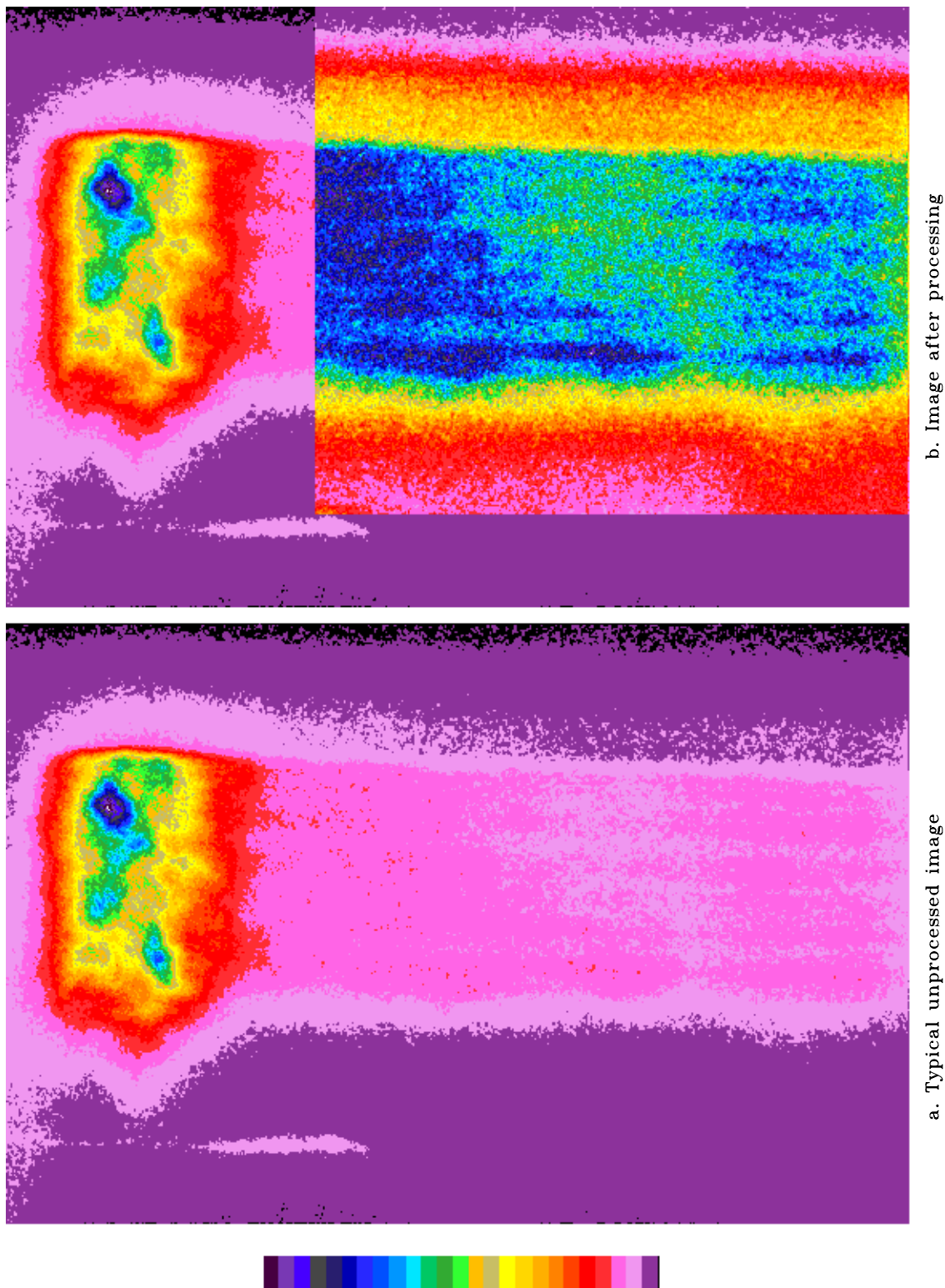


Figure 9. Example of scaling within an image.

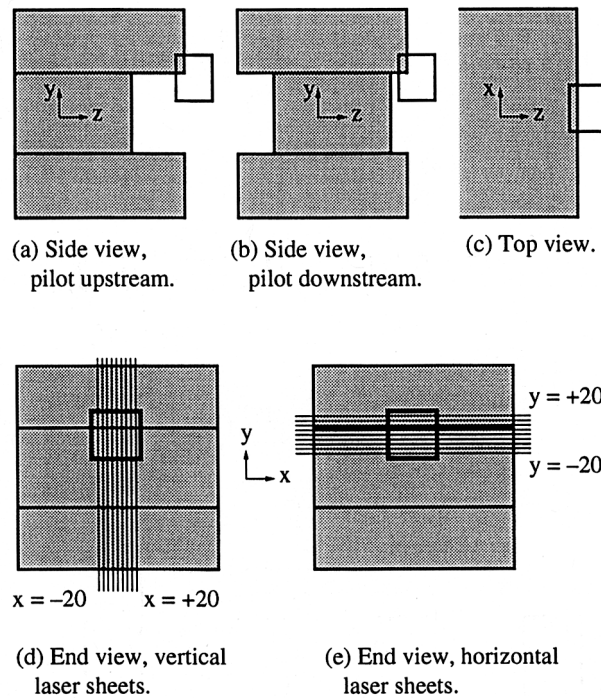
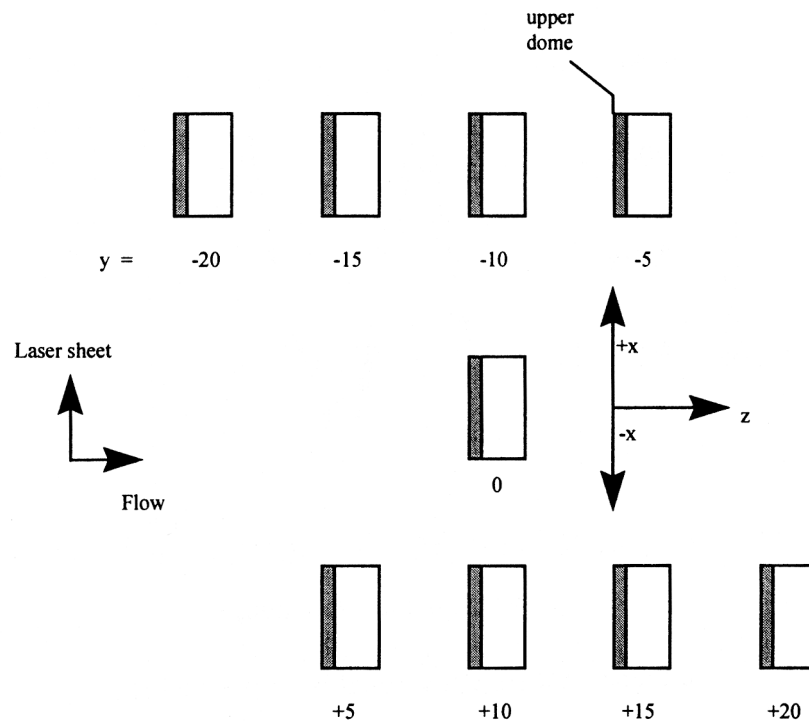
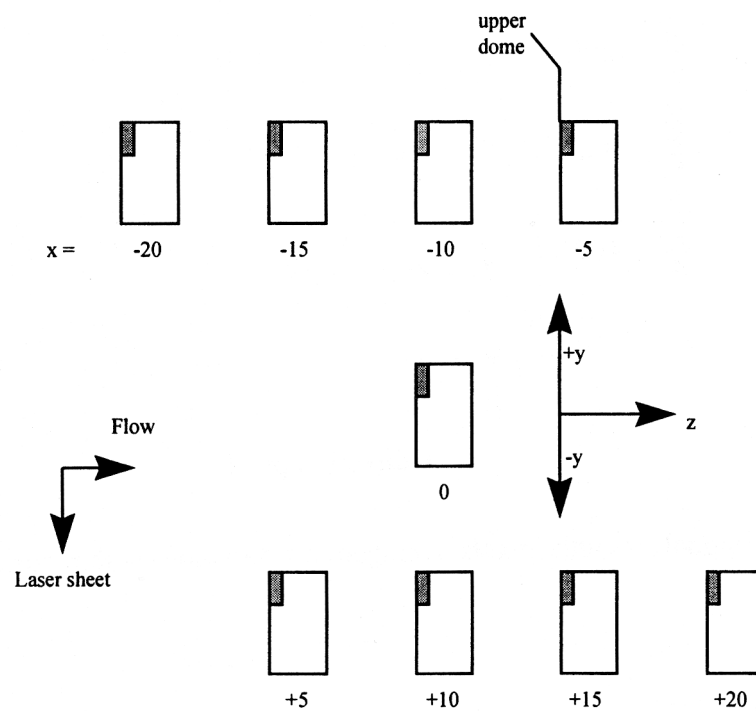


Figure 10. Arrangements of the windows and the three domes within the sector. Also shown are the fields of view, including laser sheet positions for horizontal and vertical implementation.

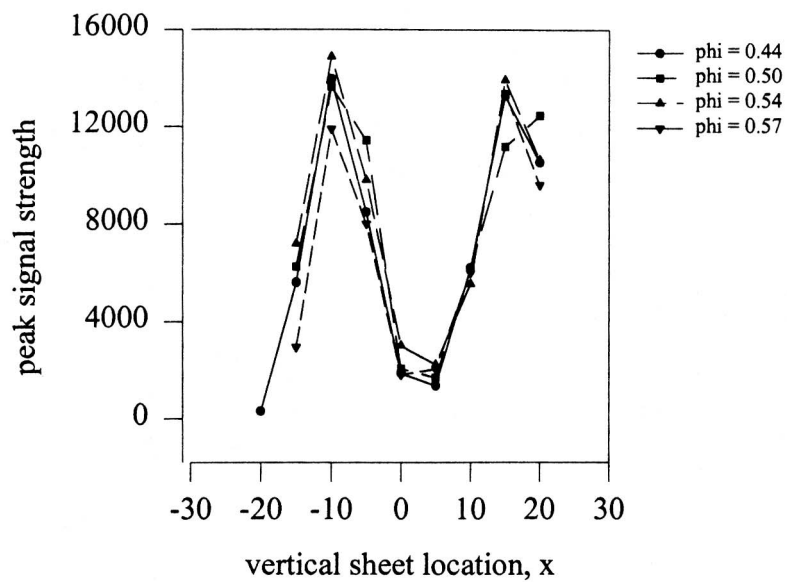


a. horizontal laser sheet

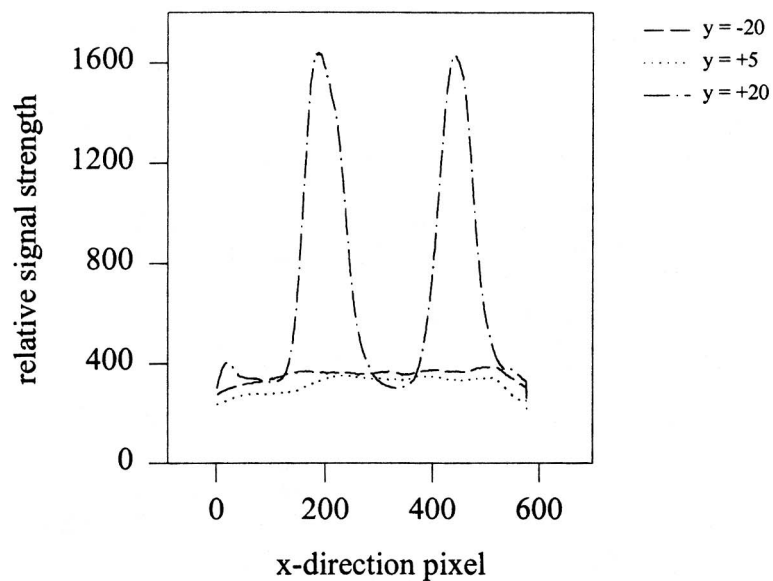


b. vertical laser sheet

Figure 11. Image layout for traversal of sector combustor.



a. Signal at different vertical laser sheet locations.



b. Average signal strength (pixels averaged in z direction) within horizontal planes.

Figure 12. Signal strength as a function of position in the 3-cup stepped configuration.

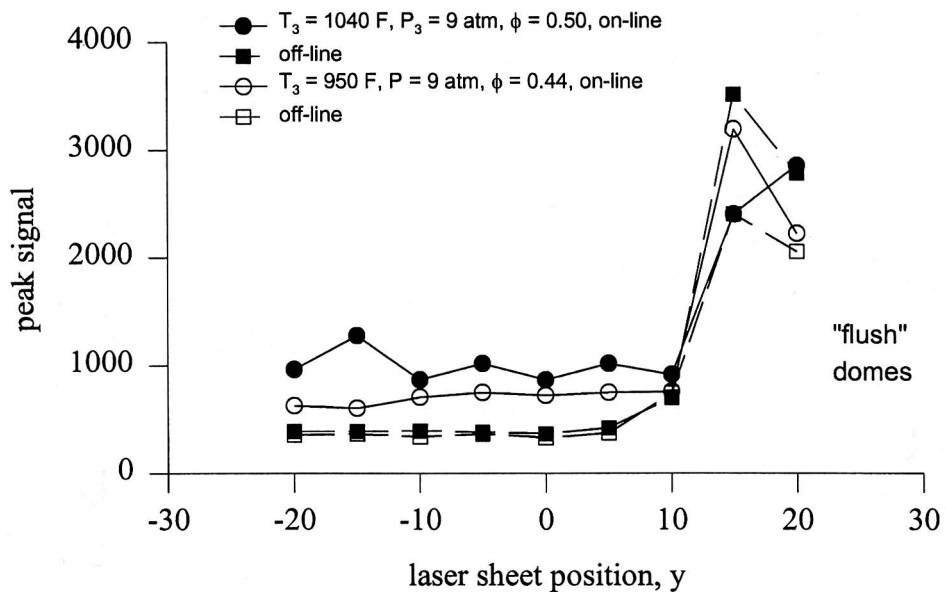
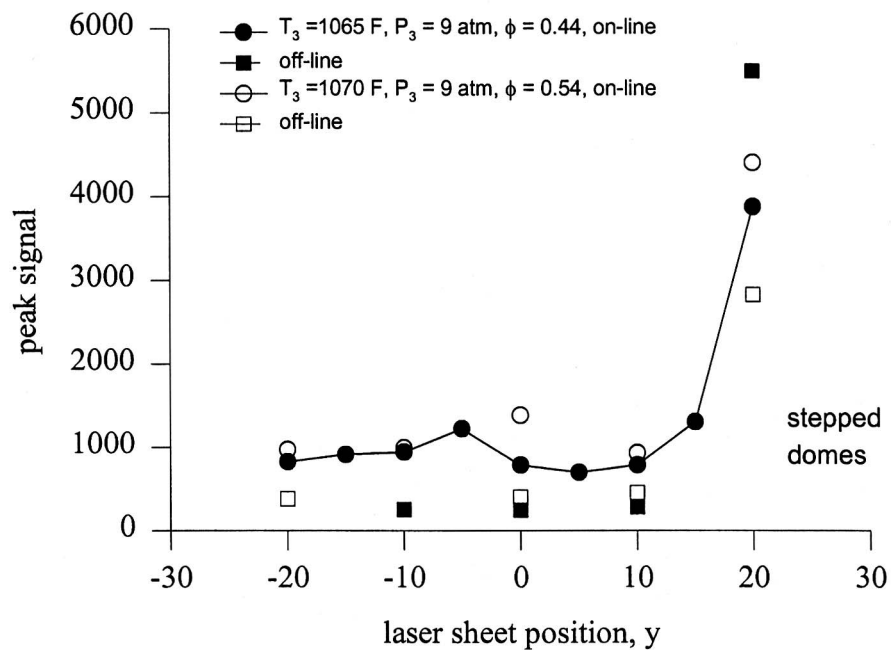


Figure 13. Peak signal for different horizontal laser sheet locations in the 3-cup dome configurations, stepped and "flush".

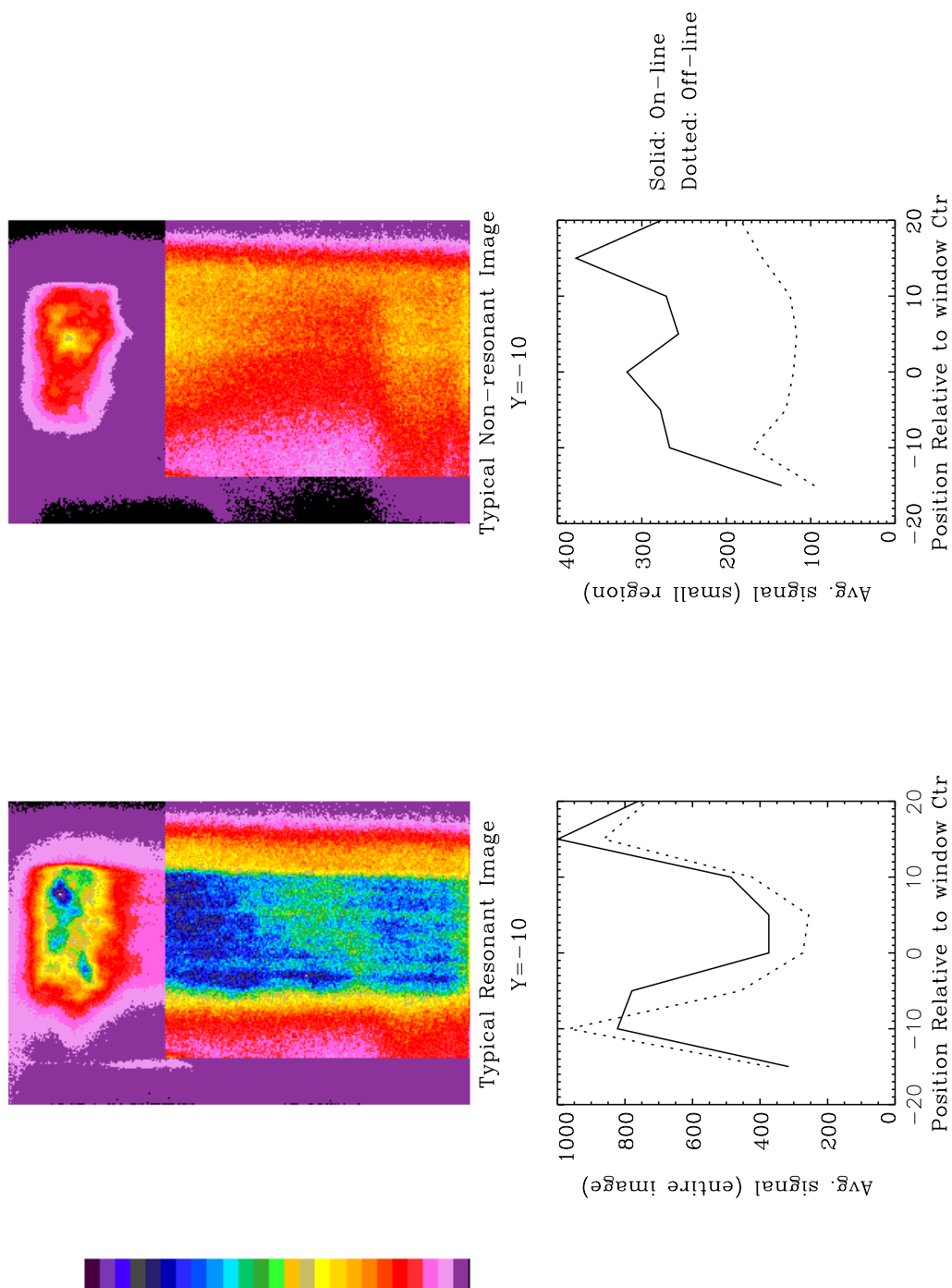


Figure 14. Discrimination between OH resonant and non-resonant signals within an image. Resonant excitation is $R_1(11)$; non-resonant is at $\lambda = 281.824$ nm. 3-cup stepped configuration, using a vertical laser sheet. $T_3 = 1040\text{F}$, $P_3 = 9$ atm, and $\phi = 0.44$.

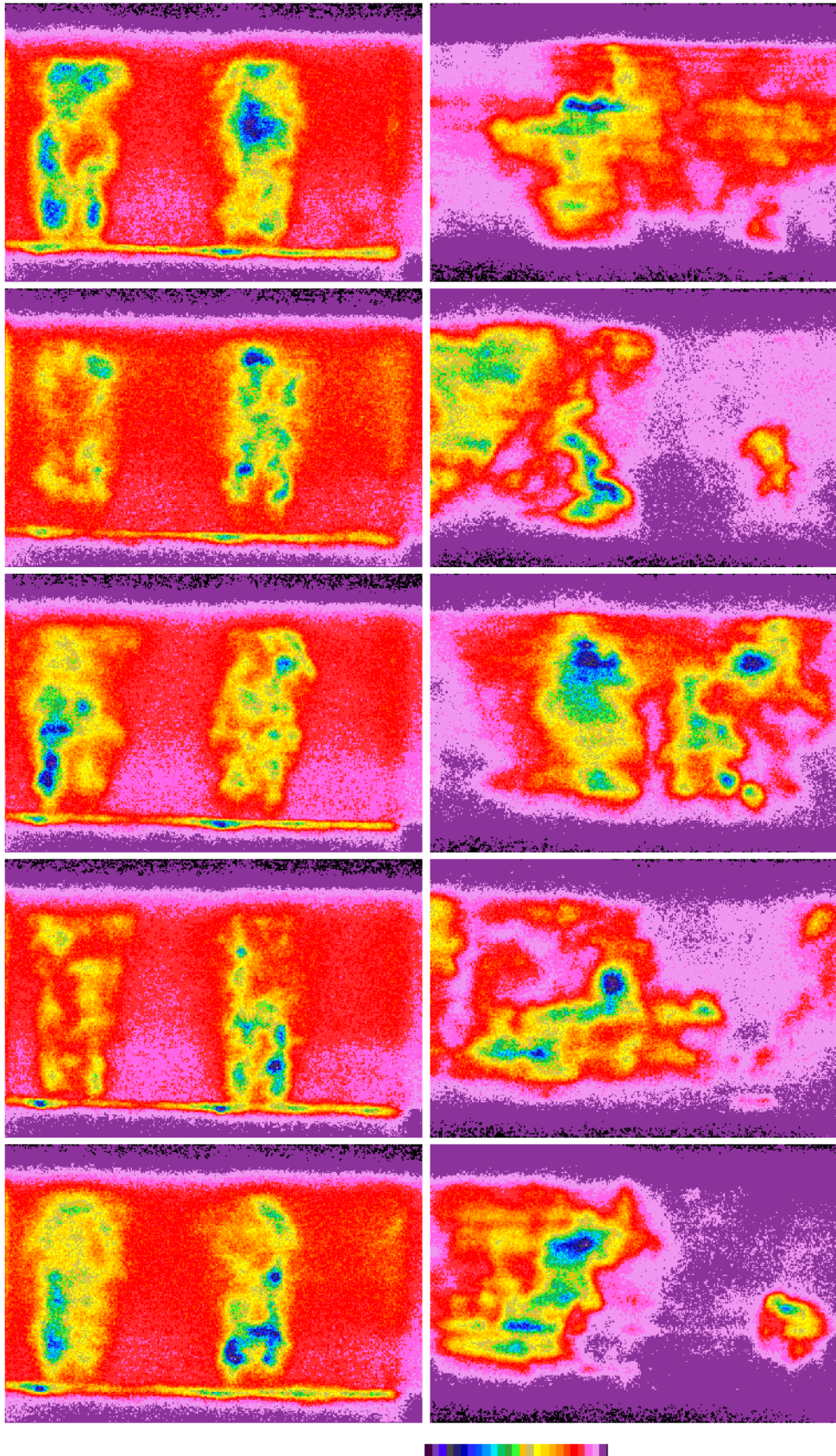


Figure 15. Shot-to-shot variation in flame structure for the triple IMFH stepped, using a horizontal laser sheet. Resonant excitation is $R_1(12)$. $T_3 = 865\text{F}$. Top Row: $P_3 = 14.5\text{ atm}$, $\phi = 0.57$, and $y = +20$. Bottom Row: $P_3 = 10.3\text{ atm}$, $\phi = 0.44$, and $y = -20$.

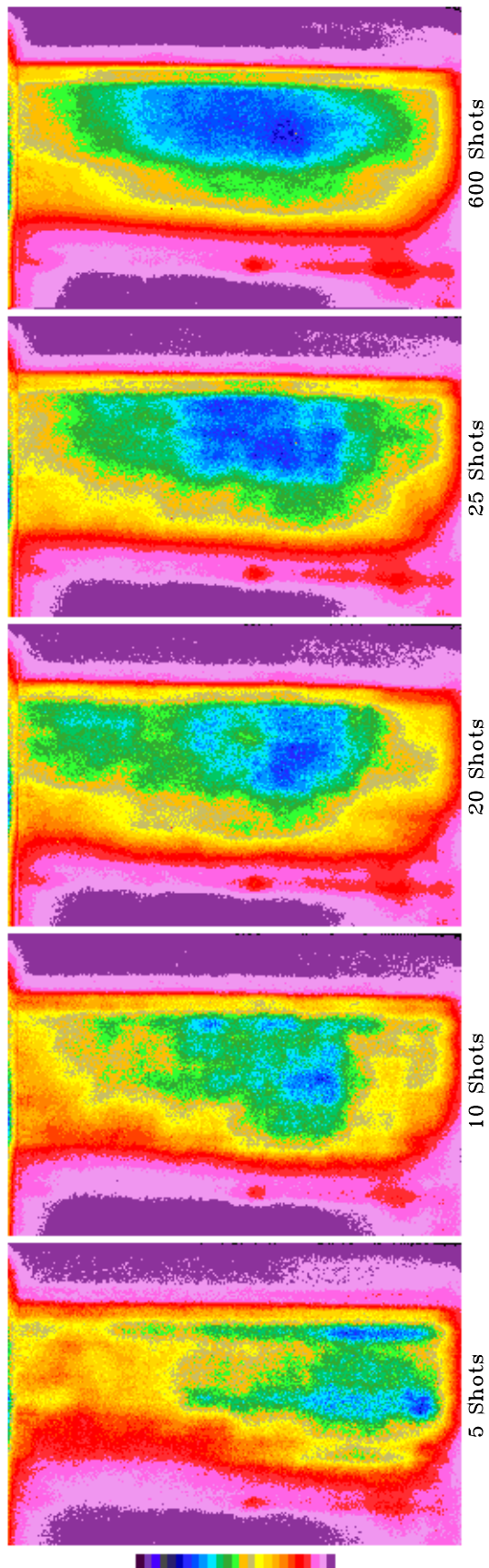


Figure 16. Effect on image appearance of averaging the fluorescence signal over time.
 $T_3 = 1010\text{F}$, $P_3 = 9.1\text{ atm}$, $\phi = 0.40$, and $y = 0$.
 Resonant excitation is $R_1(12)$. The laser sheet is horizontal.

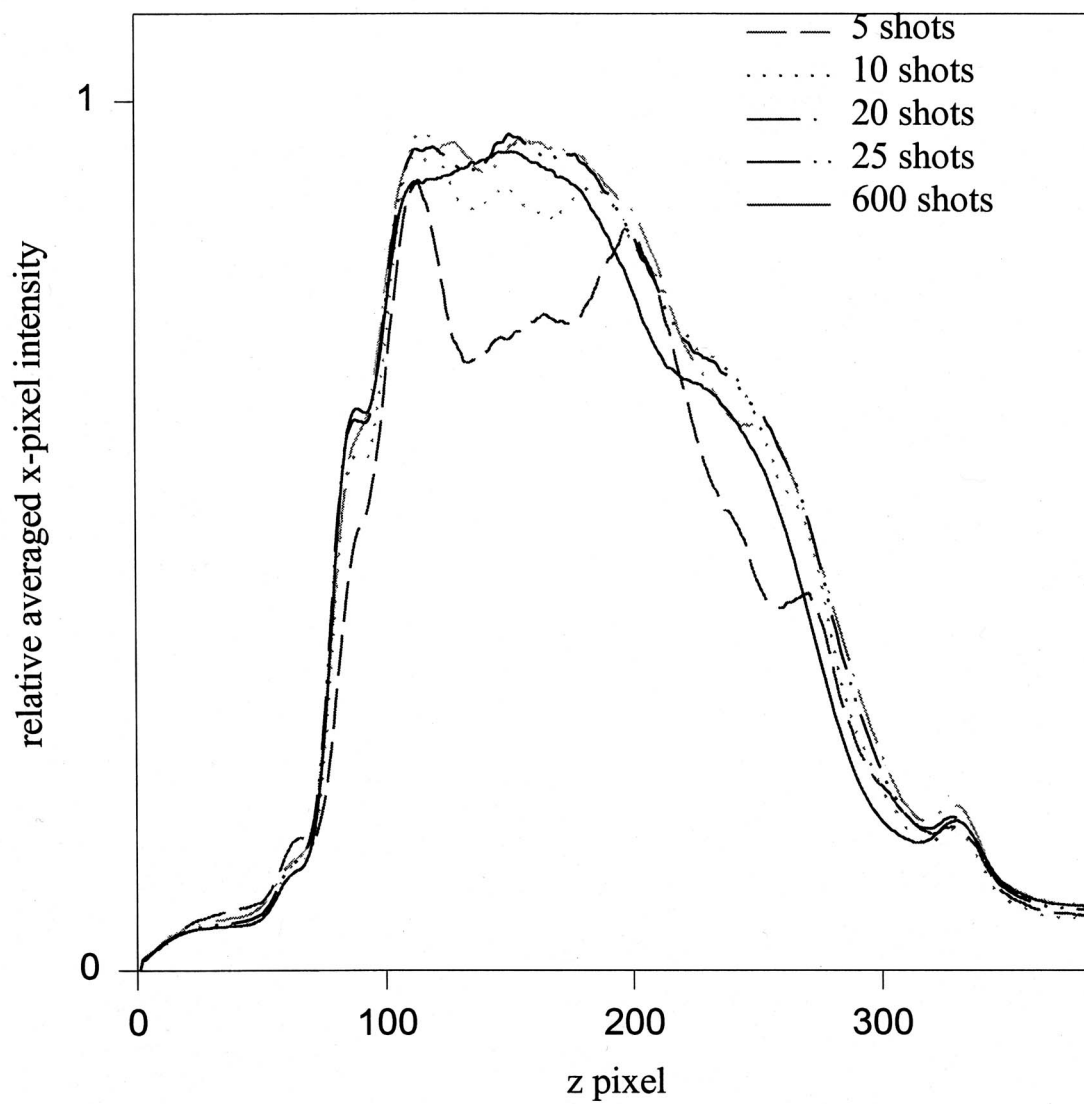


Figure 17. Effect of number of laser shots on image cross-sectional structure, for the images of Figure 16.

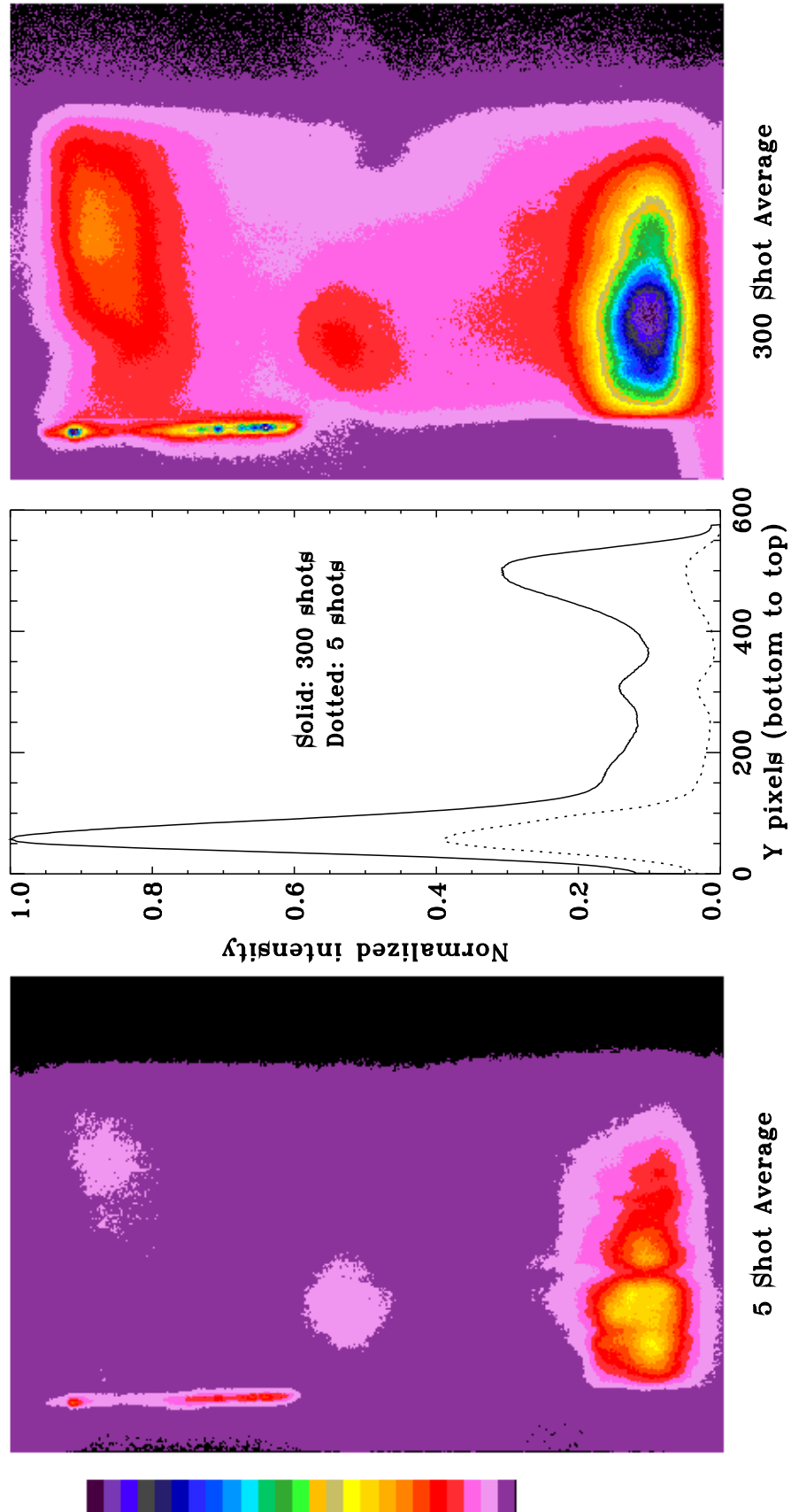


Figure 18 Effect of the number of shots averaged on image cross sectional structure. $T_3 = 1020$ F, $P_3 = 9.1$ atm, $\phi = 0.44$., and $x=+5$. Resonant excitation is $Q_1(9)$. The laser sheet is vertical.

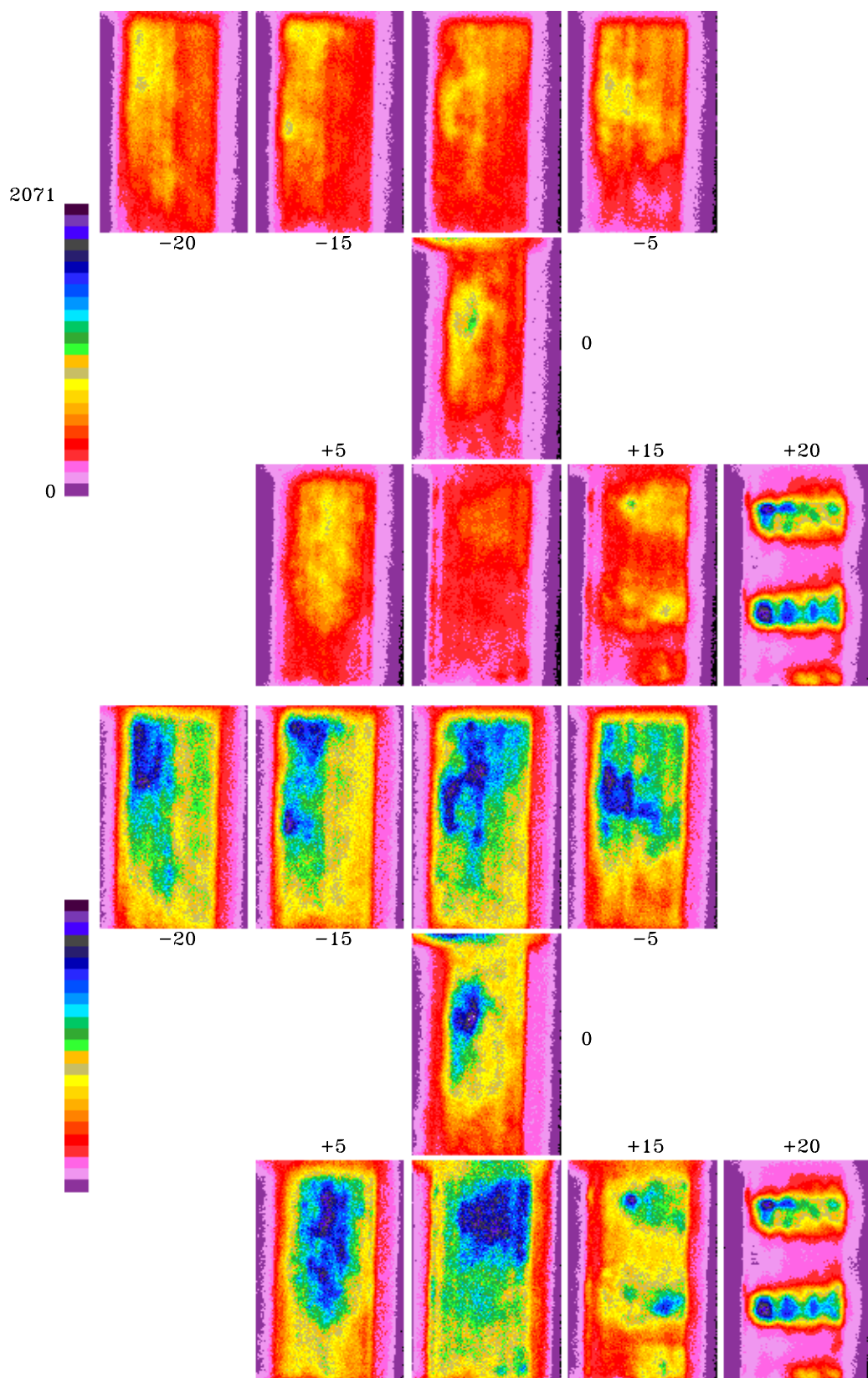


Figure 19. Images from the 3-cup stepped configuration using a horizontal laser sheet. Resonant excitation is $R_1(10)$. $T_3=1040$ F, $P_3=9.1$ atm, $\phi = 0.44$, and $x = +5$. Top: Images on same scale. Bottom: Images individually scaled.

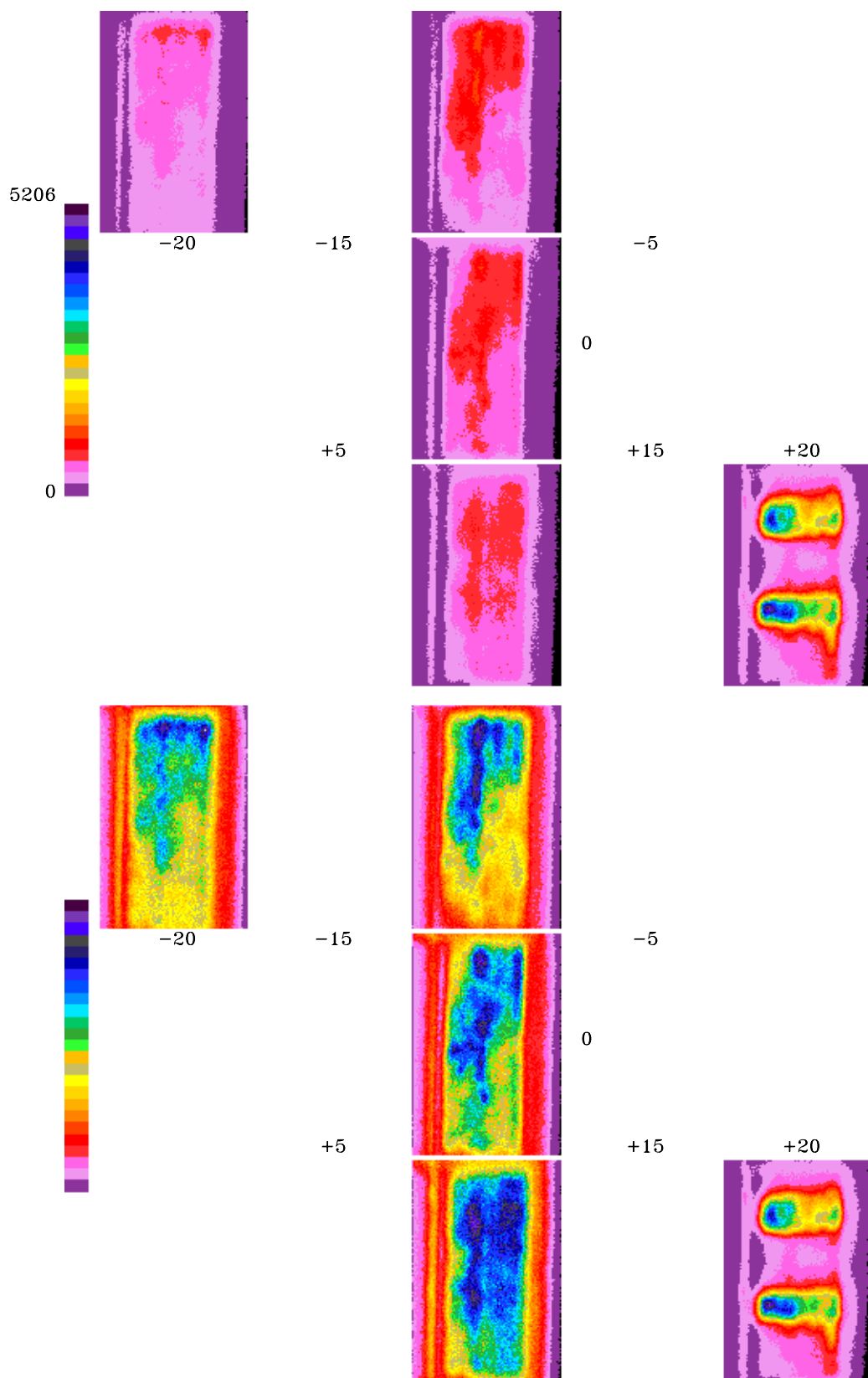


Figure 20. Images from the 3-cup stepped configuration using a horizontal laser sheet. Resonant excitation is $R_1(10)$. $T_3=1040$ F, $P_3=9.1$ atm, $\phi = 0.50$, and $x = +5$. Top: Images on same scale. Bottom: Images individually scaled.

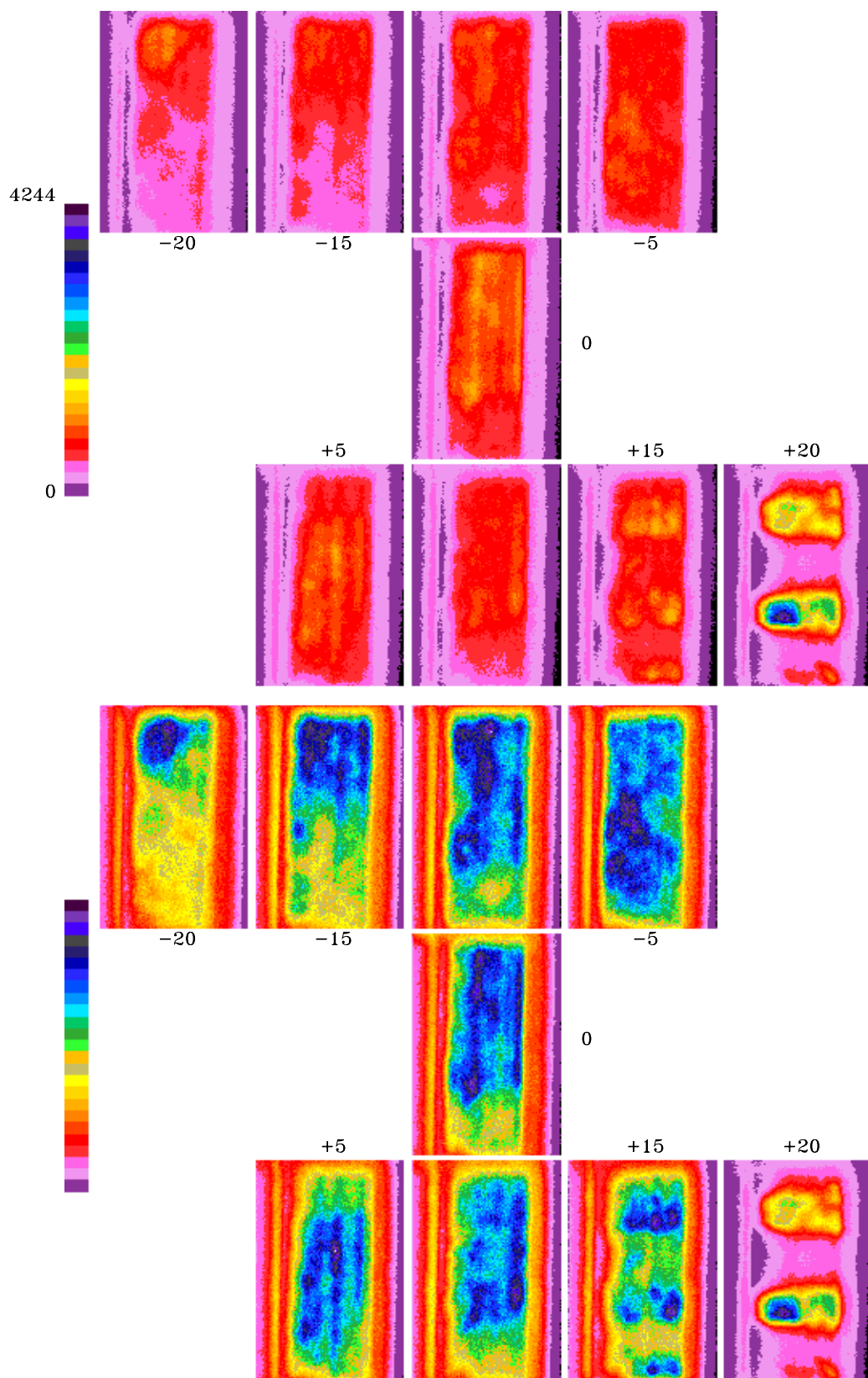


Figure 21. Images from the 3 cup stepped configuration using a horizontal laser sheet. Resonant excitation is $R_1(10)$. $T_3=1040$ F, $P_3=9.1$ atm, $\phi = 0.54$, and $x = +5$.
 Top: Images on same scale. Bottom: Images individually scaled.

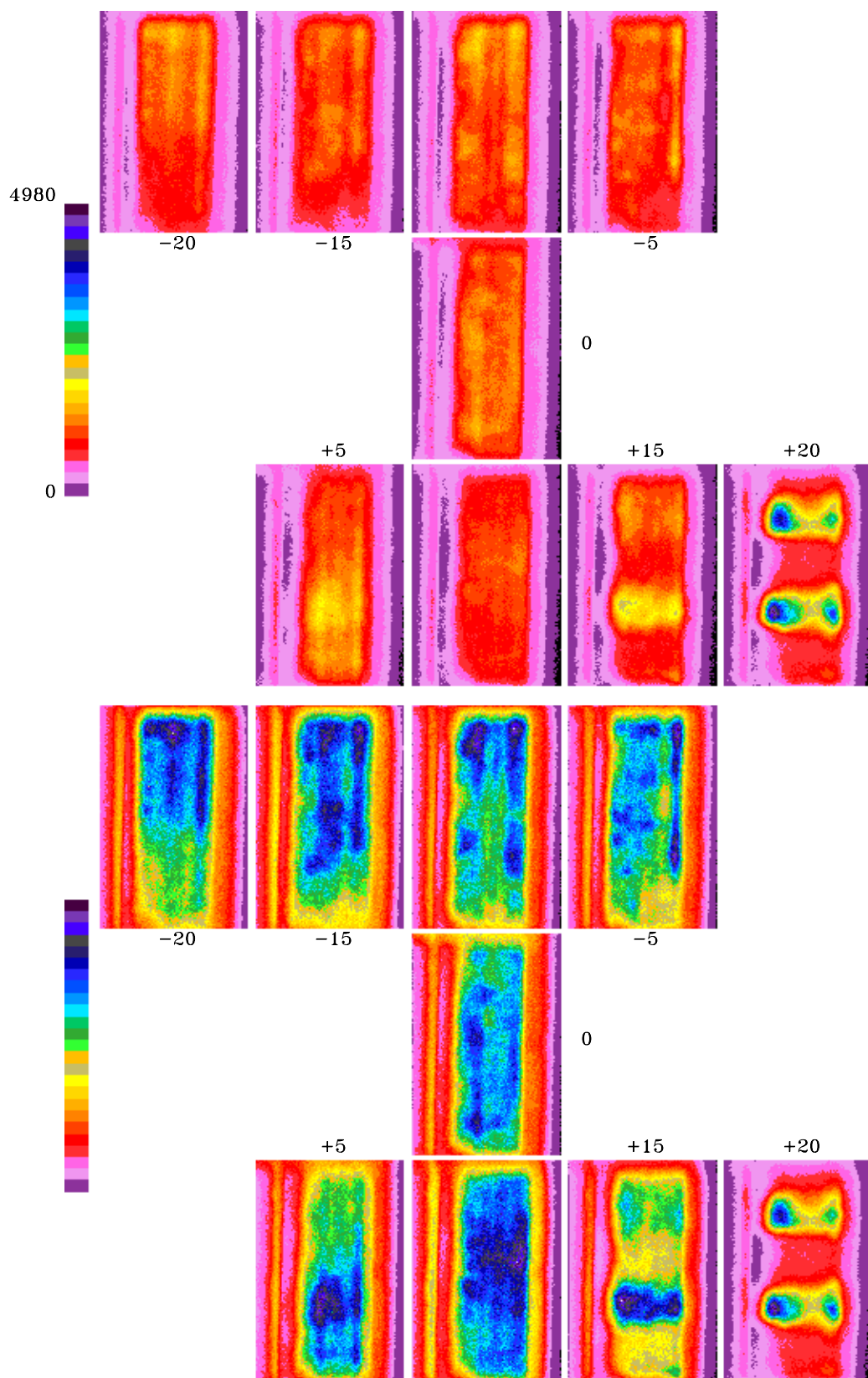


Figure 22. Images from the 3 cup stepped configuration using a horizontal laser sheet. Resonant excitation is $R_1(10)$. $T_3=1040$ F, $P_3=9.1$ atm, $\phi = 0.54$, and $x = +5$. Top: Images on same scale. Bottom: Images individually scaled.

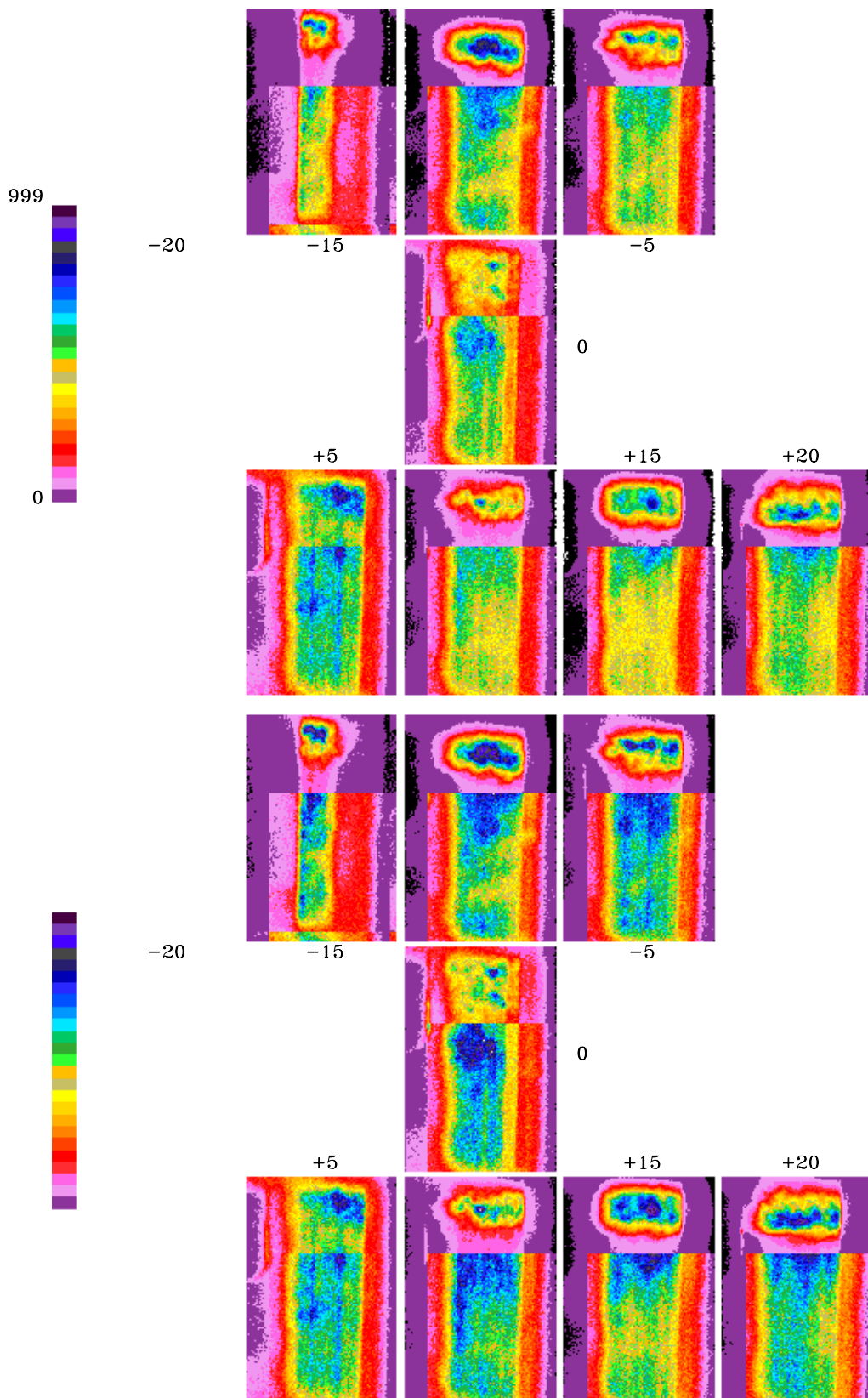


Figure 23. Images from the 3-cup stepped configuration using a vertical laser sheet. Resonant excitation is $R_1(10)$. $T_3=1040\text{F}$, $P_3=9.1\text{ atm}$, and $\phi = 0.44$. Top: Images on same scale. Bottom: Images individually scaled.

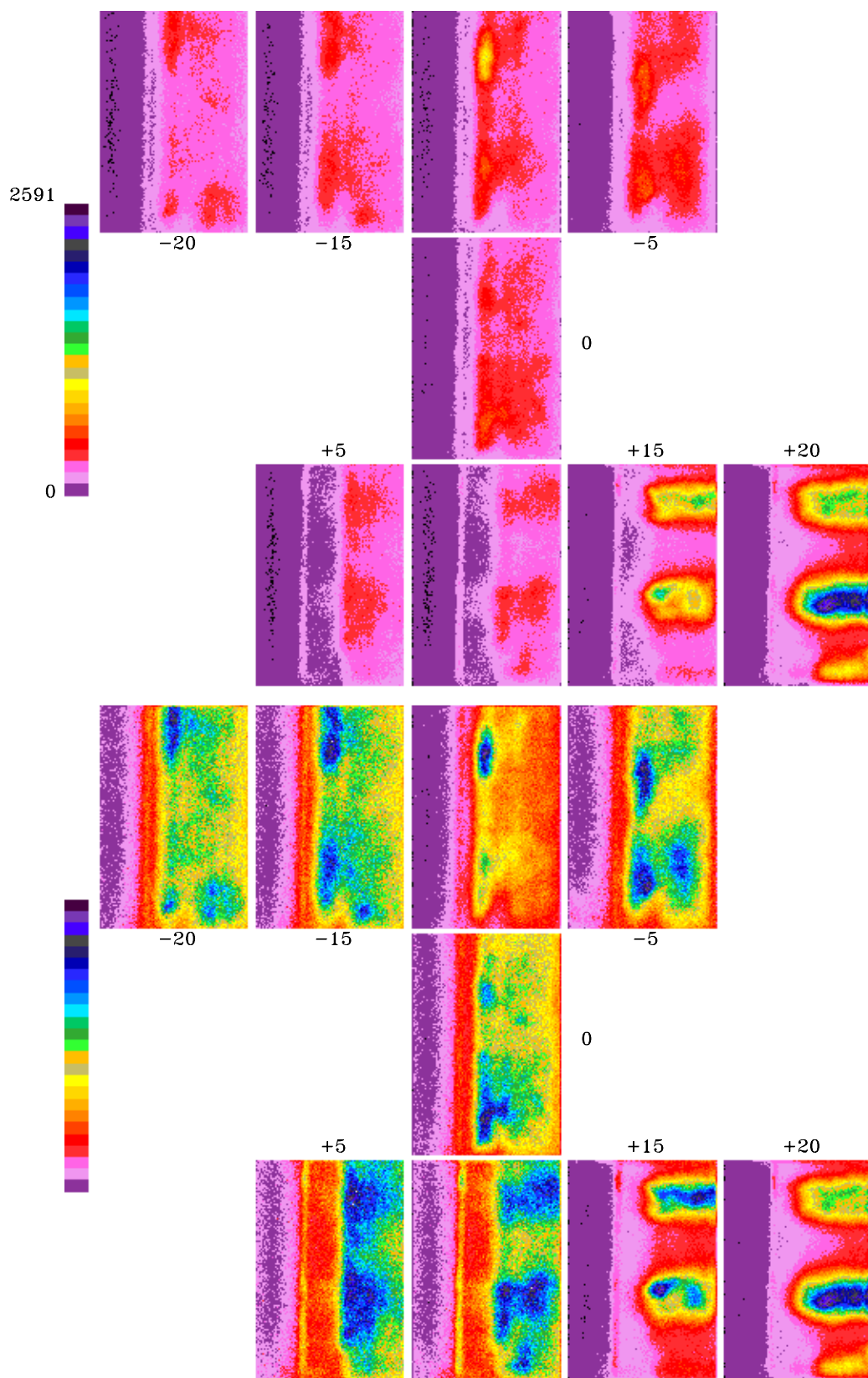


Figure 24. Images from the 3-cup "flush" configuration using a horizontal laser sheet. Resonant excitation is $R_1(12)$. $T_3=1023\text{F}$, $P_3=9.1\text{ atm}$, and $\phi = 0.44$. Top: Images on same scale. Bottom: Images individually scaled.

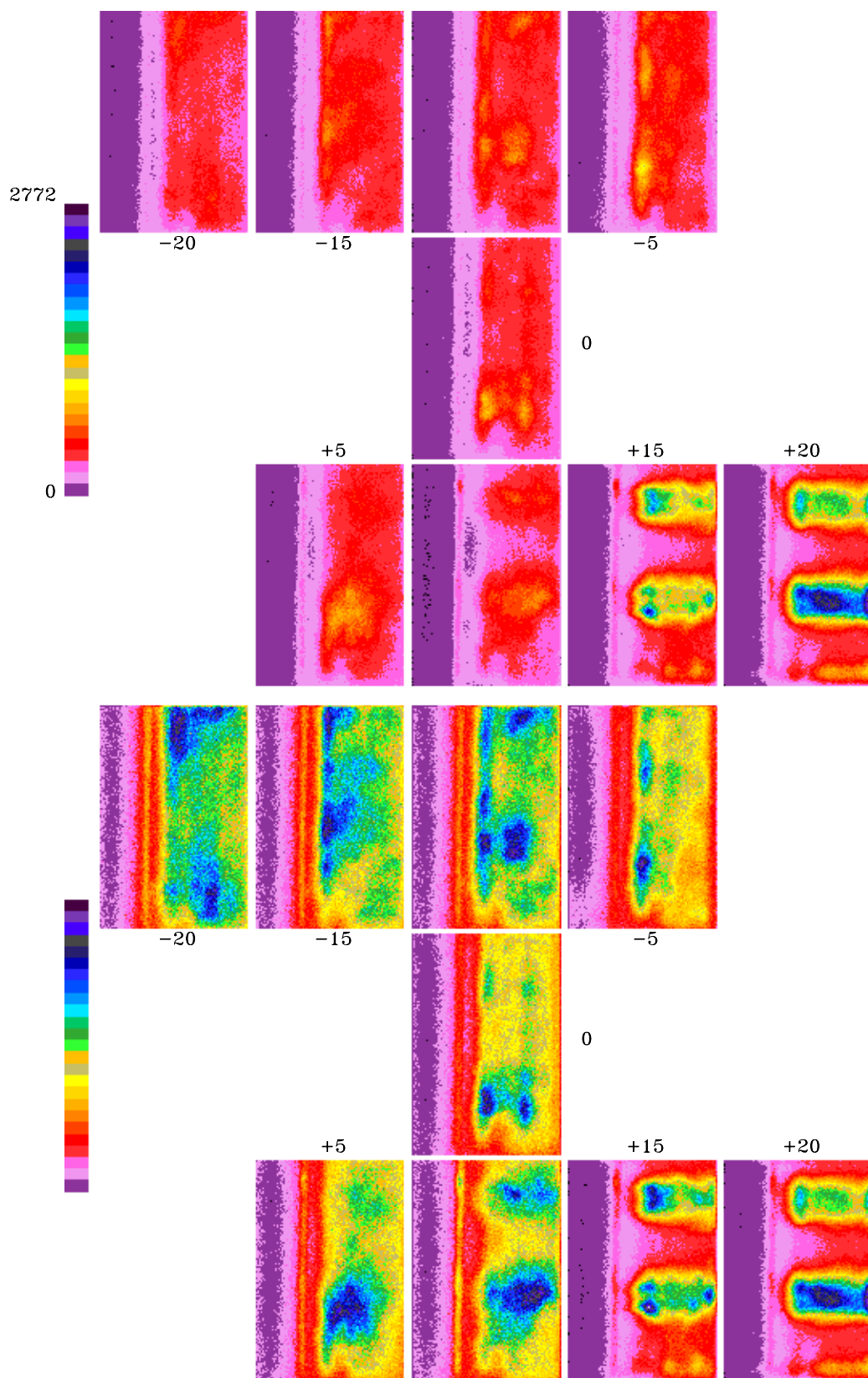


Figure 25. Images from the 3-cup "flush" configuration using a horizontal laser sheet. Resonant excitation is $R_1(12)$. $T_3=1023\text{F}$, $P_3=9.1\text{ atm}$, and $\phi = 0.50$. Top: Images on same scale. Bottom: Images individually scaled.

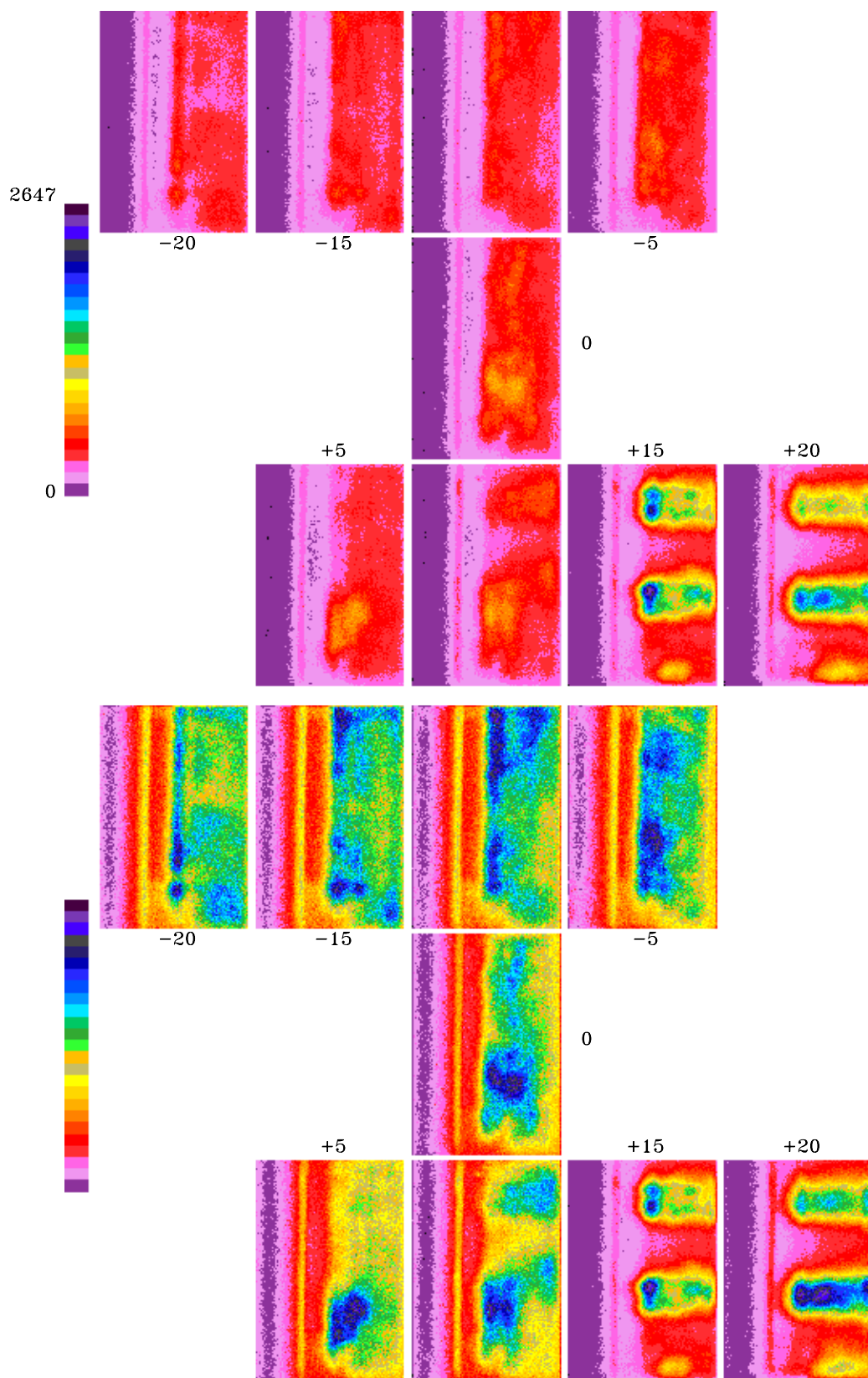


Figure 26. Images from the 3-cup "flush" configuration using a horizontal laser sheet. Resonant excitation is $R_1(12)$. $T_3=1023\text{F}$, $P_3=9.1\text{ atm}$, and $\phi = 0.54$. Top: Images on same scale. Bottom: Images individually scaled.

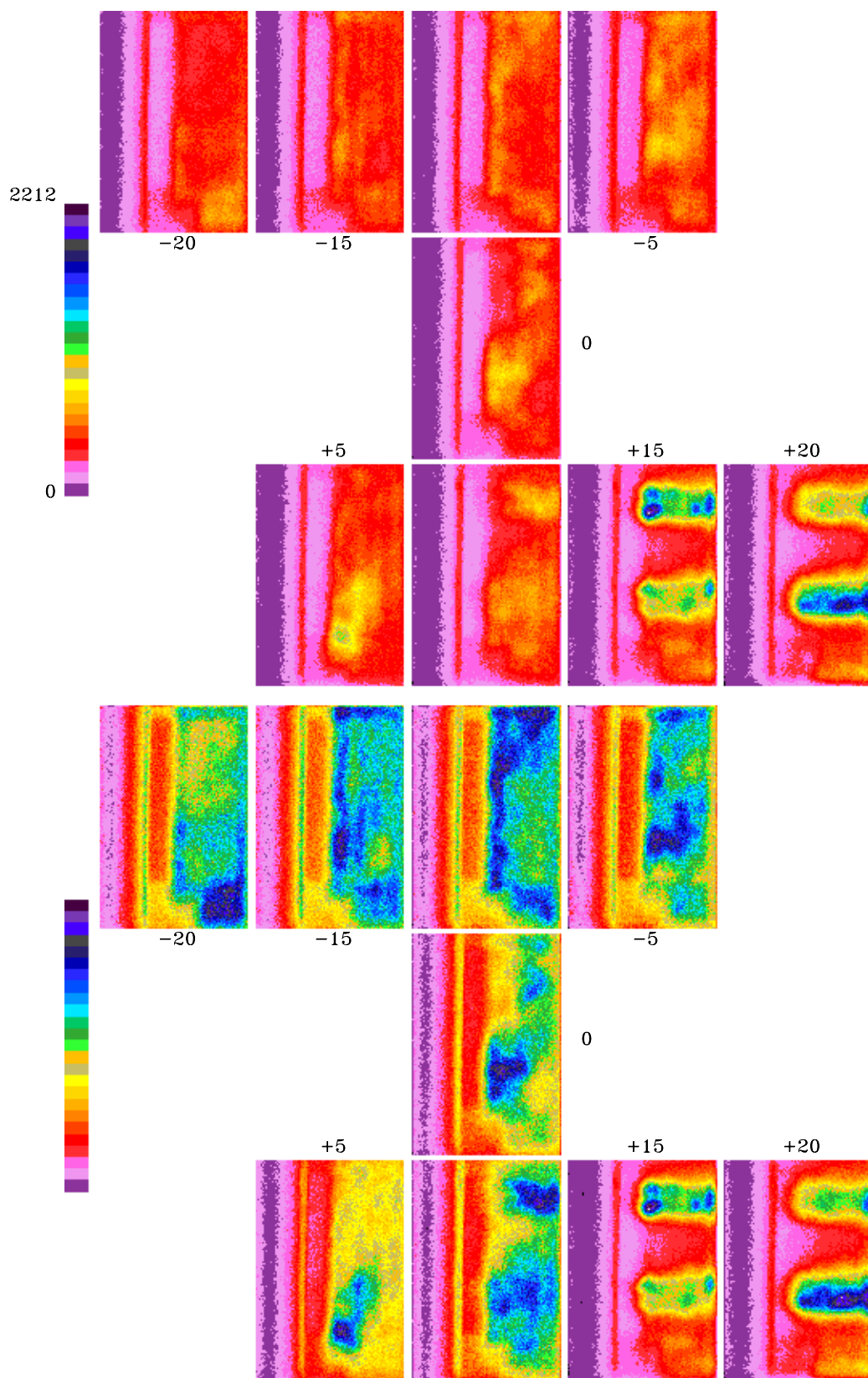


Figure 27. Images from the 3-cup "flush" configuration using a horizontal laser sheet. Resonant excitation is $R_1(12)$. $T_3=1023\text{F}$, $P_3=9.1\text{ atm}$, and $\phi = 0.57$. Top: Images on same scale. Bottom: Images individually scaled.

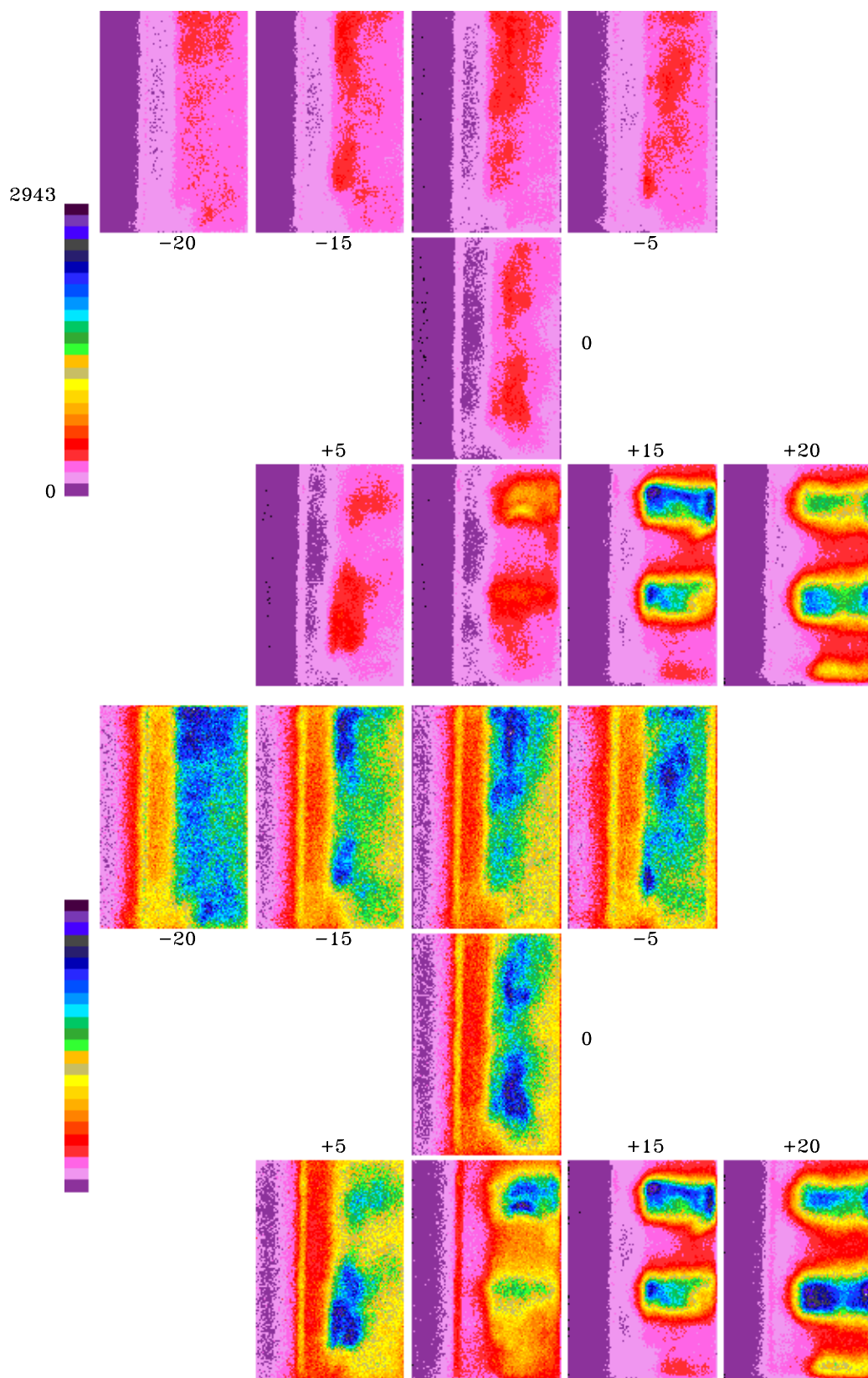


Figure 28. Images from the 3-cup "flush" configuration using a horizontal laser sheet. Resonant excitation is $R_1(12)$. $T_3=930$ F, $P_3=8.1$ atm, and $\phi = 0.50$. Top: Images on same scale. Bottom: Images individually scaled.

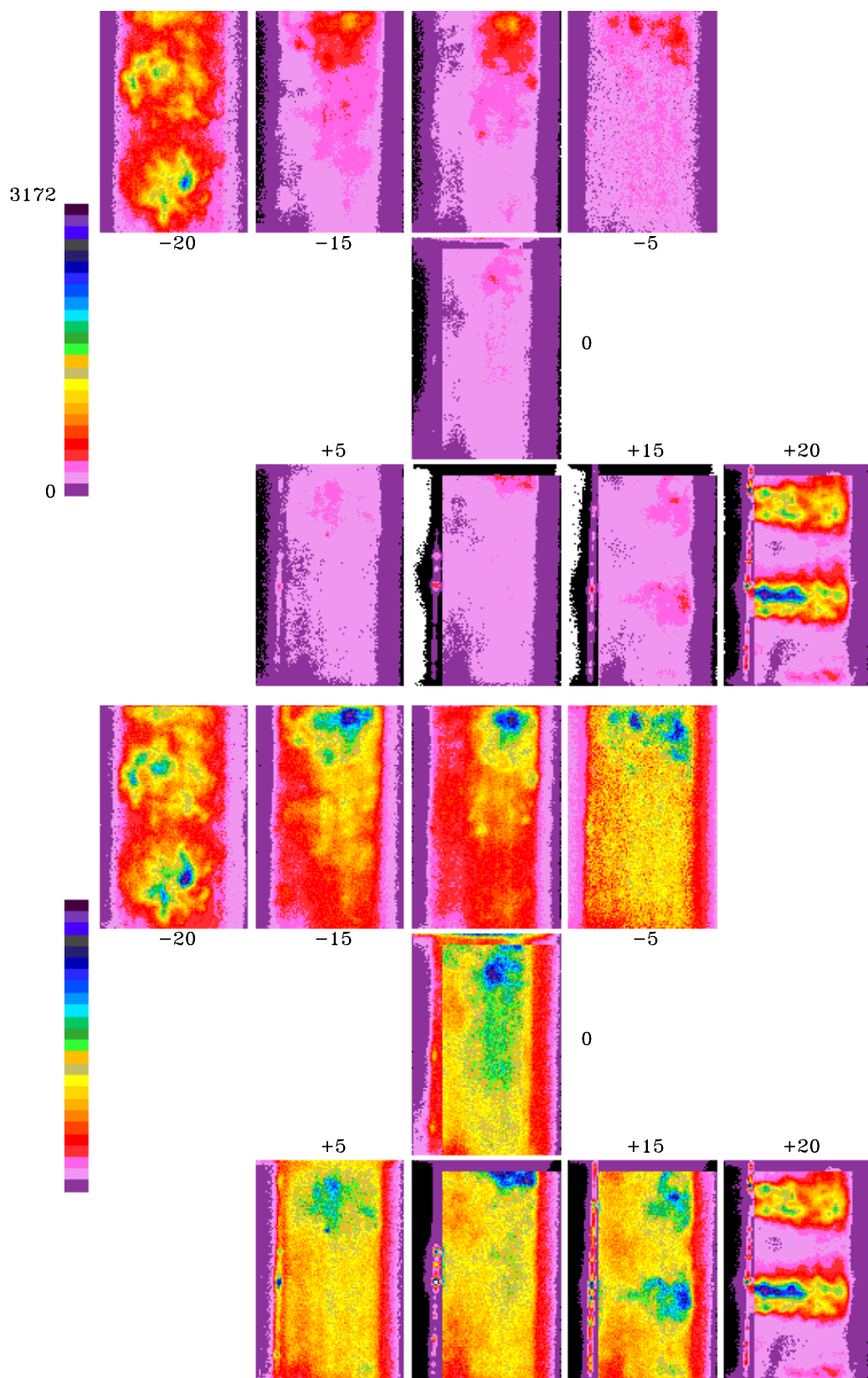


Figure 29. Images from the triple IMFH stepped configuration using a horizontal laser sheet. Resonant excitation is $R_1(12)$. $T_3=1020$ F, $P_3=9.1$ atm, and $\phi = 0.44$. Top: Images on same scale. Bottom: Images individually scaled.

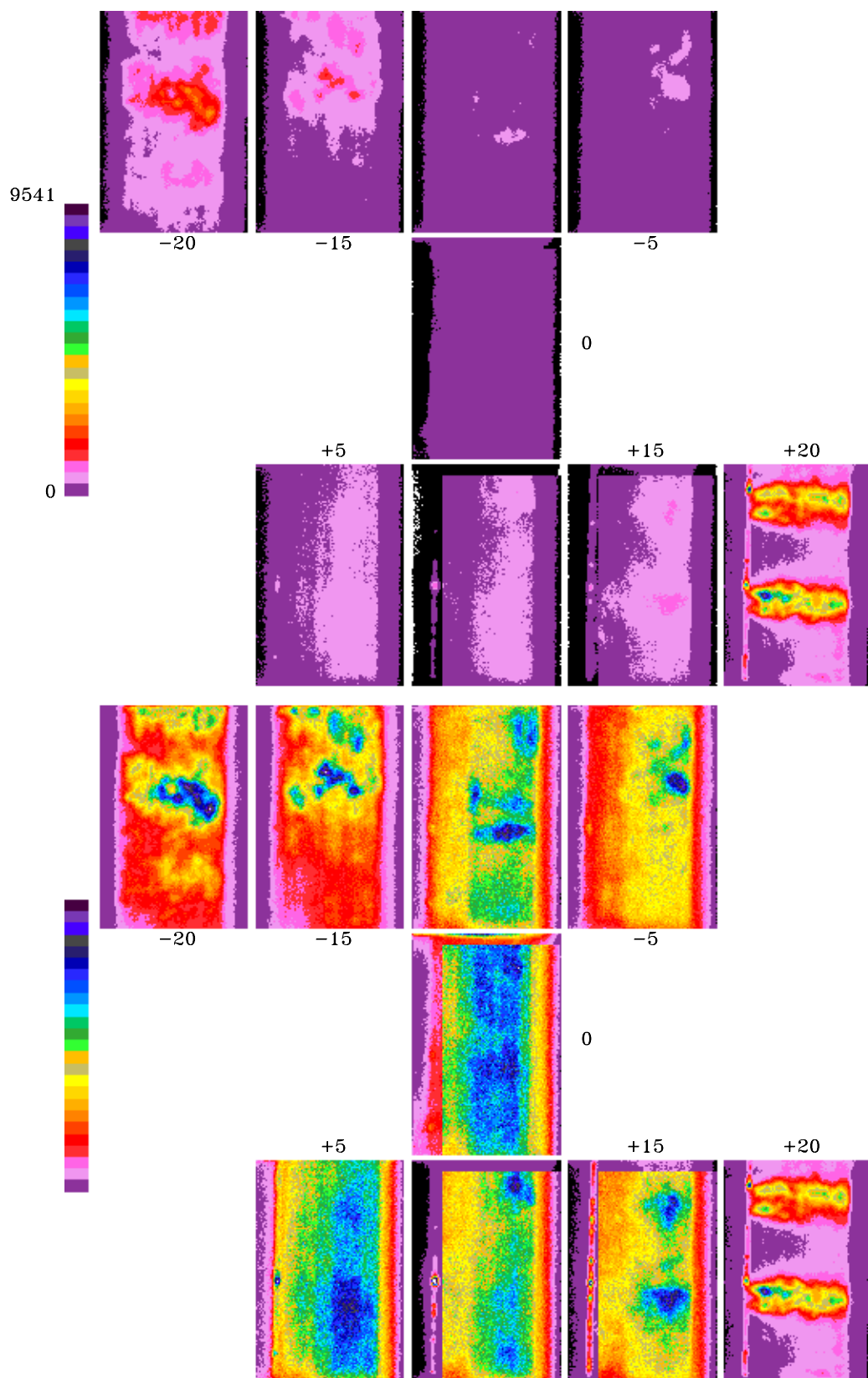


Figure 30. Images from the triple IMFH stepped configuration using a horizontal laser sheet. Resonant excitation is $R_1(12)$. $T_3=1020$ F, $P_3=9.1$ atm, and $\phi = 0.50$. Top: Images on same scale. Bottom: Images individually scaled.

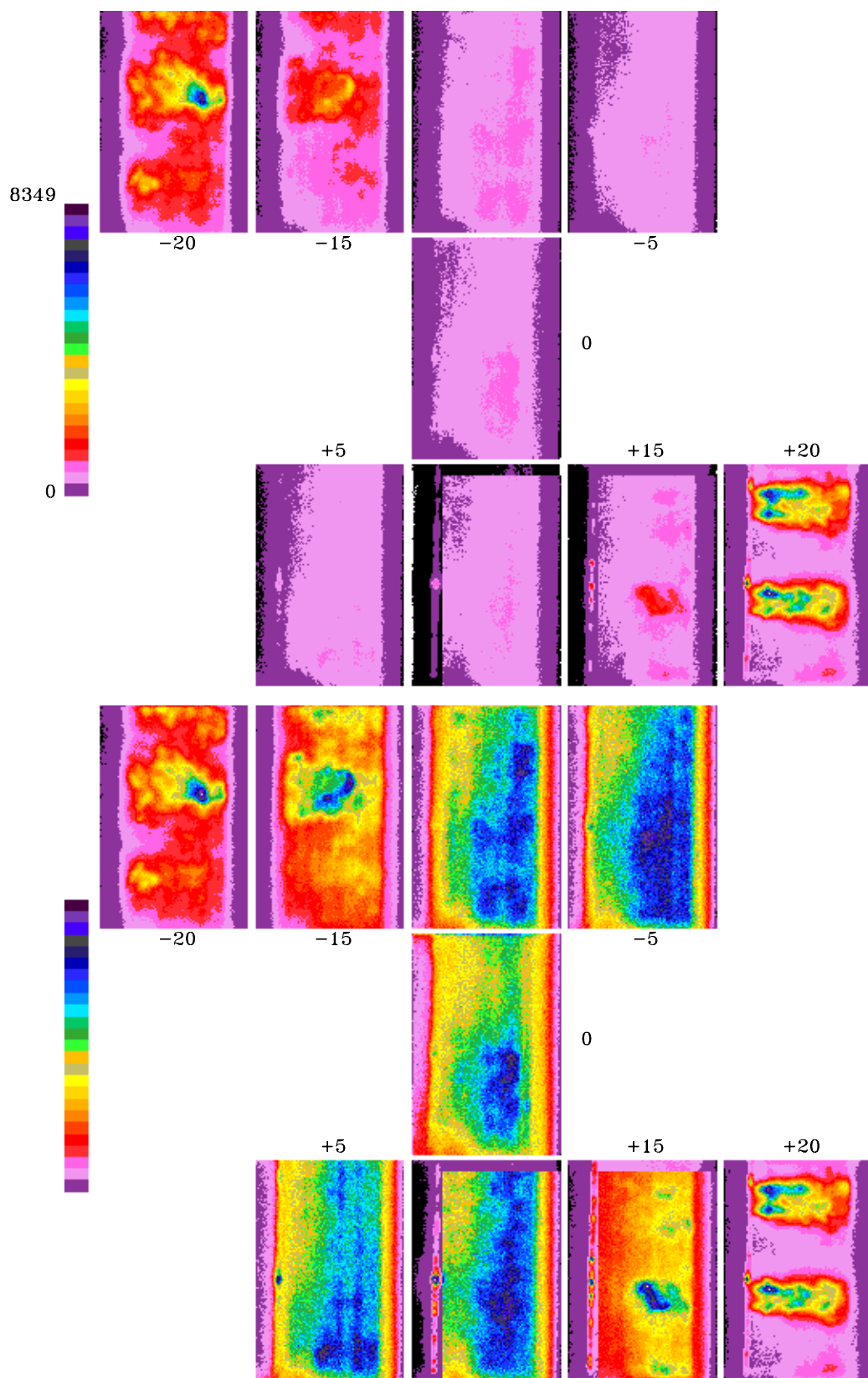


Figure 31. Images from the triple IMFH stepped configuration using a horizontal laser sheet. Resonant excitation is $R_1(12)$. $T_3=1020$ F, $P_3=9.1$ atm, and $\phi = 0.54$. Top: Images on same scale. Bottom: Images individually scaled.

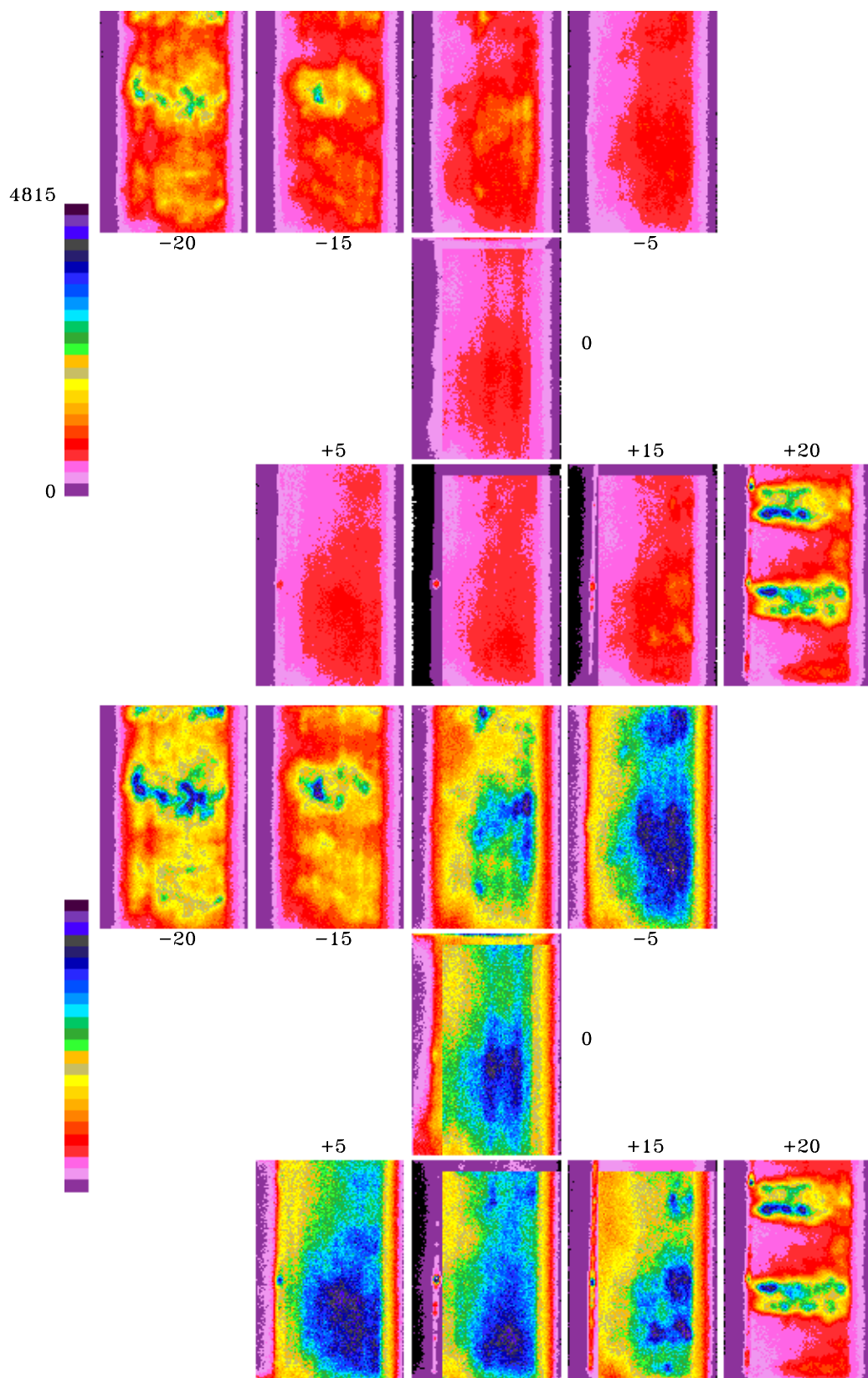


Figure 32. Images from the triple IMFH stepped configuration using a horizontal laser sheet. Resonant excitation is $R_1(12)$. $T_3=1020$ F, $P_3=9.1$ atm, and $\phi = 0.57$. Top: Images on same scale. Bottom: Images individually scaled.

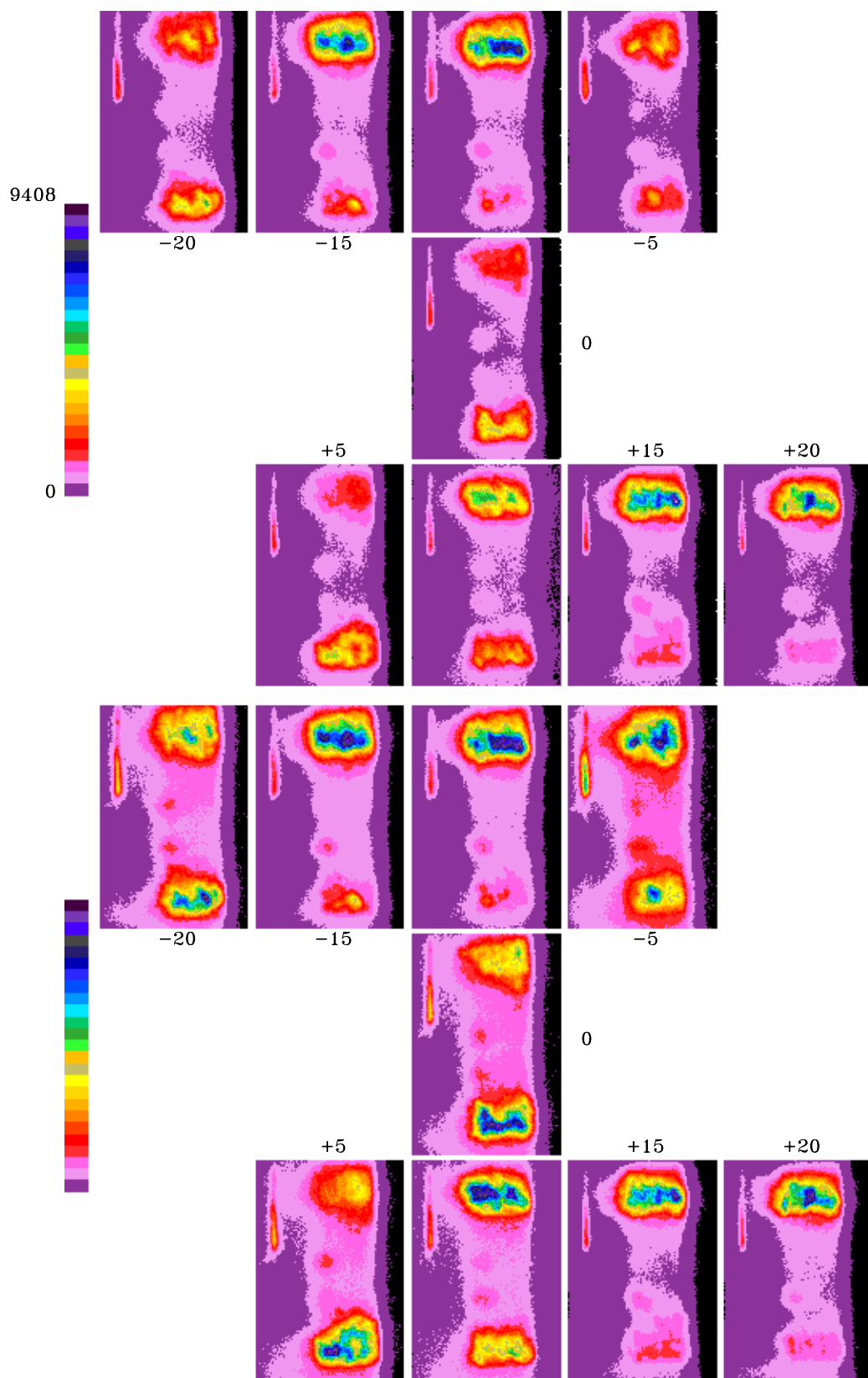


Figure 33. Images from the triple IMFH stepped configuration using a vertical laser sheet. Resonant excitation is $R_1(12)$. $T_3=1020$ F, $P_3=9.1$ atm, and $\phi = 0.53$. Top: Images on same scale. Bottom: Images individually scaled.

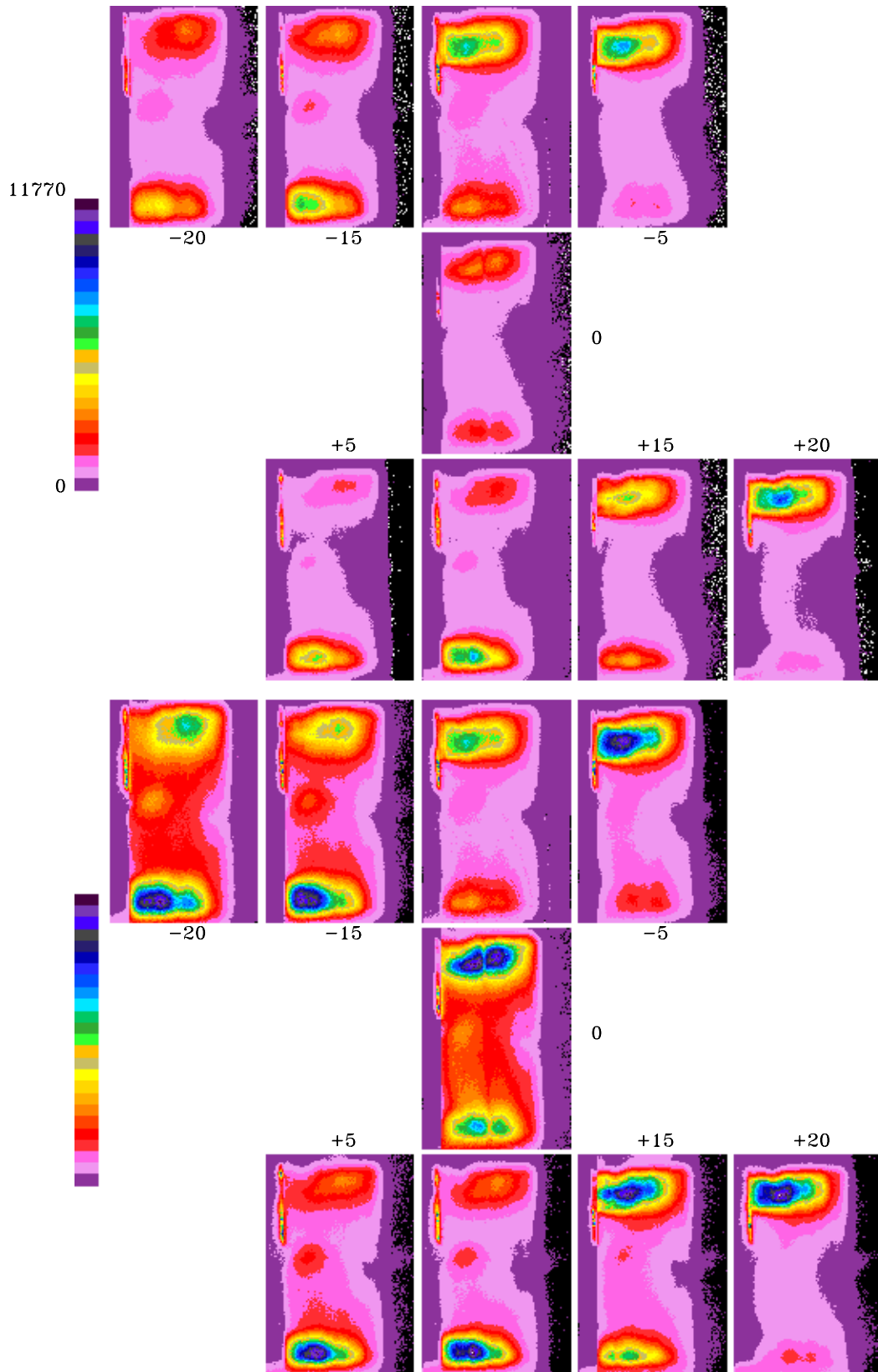


Figure 34. Images from configuration D using a vertical laser sheet. Resonant excitation is $Q_1(9)$. $T_3=1020$ F, $P_3=9.1$ atm, and $\phi = 0.49$. Top: Images on same scale. Bottom: Images individually scaled.

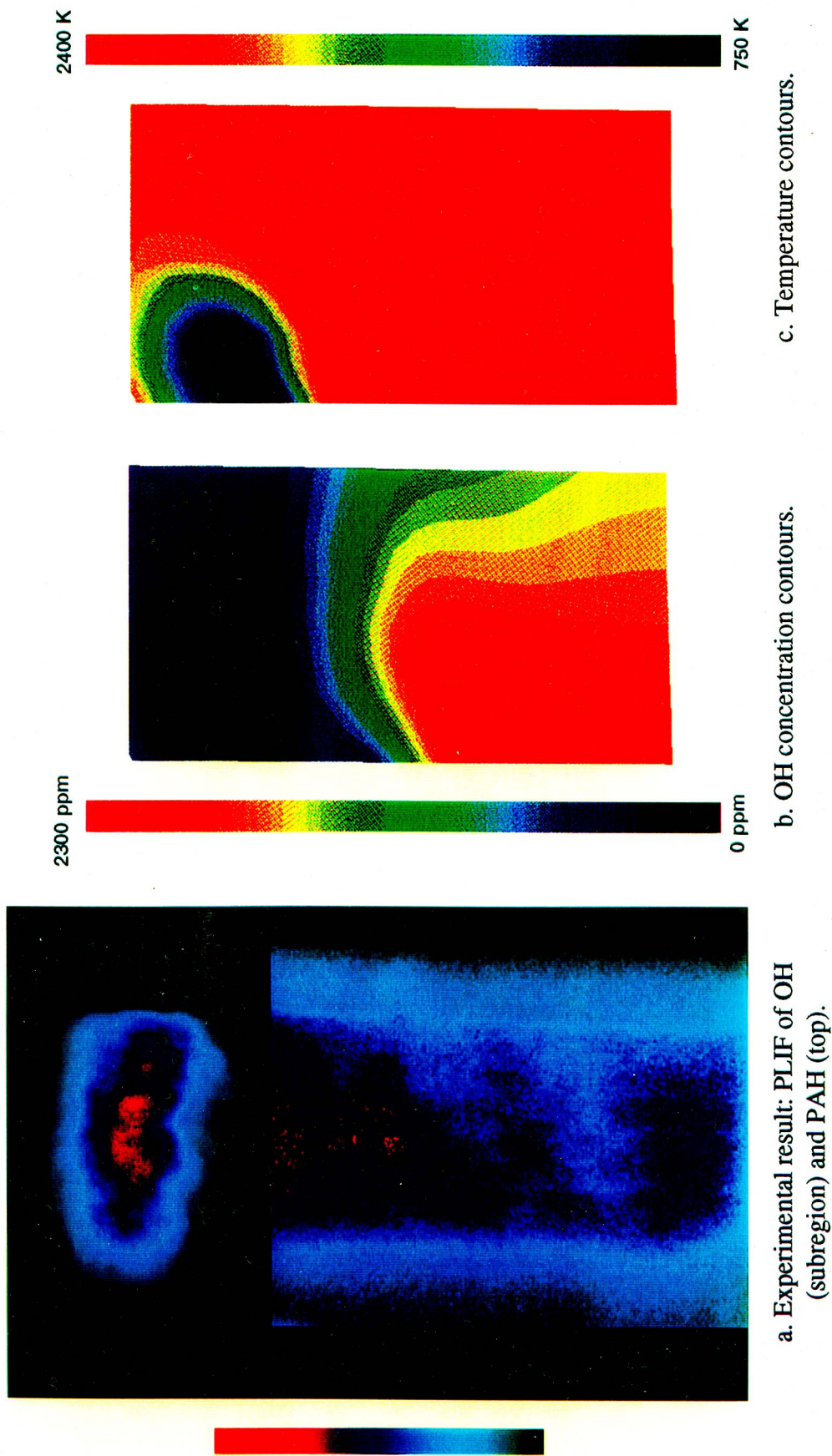


Figure 35. Comparison of experimental and CFD results. Experimental inlet conditions: $T_3 = 1040$ F, $P_3 = 9.1$ atm, $\phi = 0.44$. CFD inlet conditions: $T_3 = 1100$ F, $P_3 = 10.3$ atm, $\phi = 0.58$.

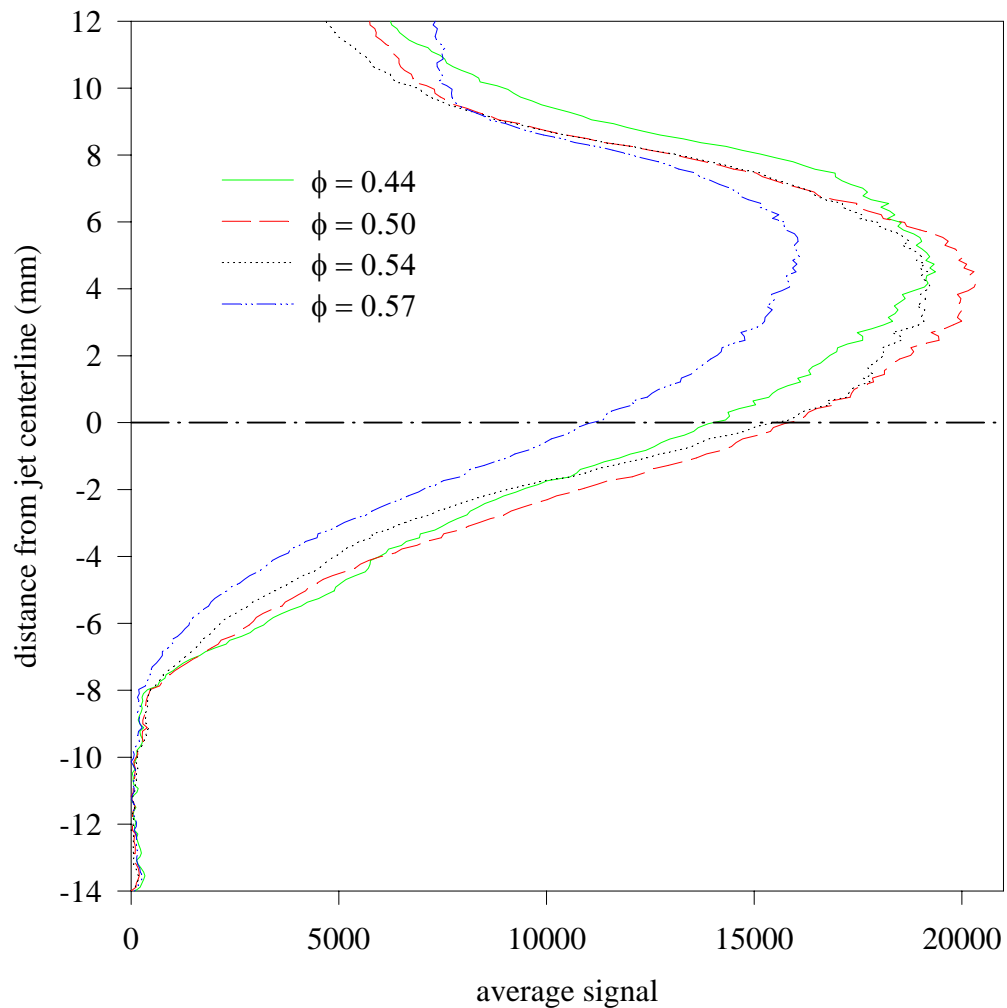
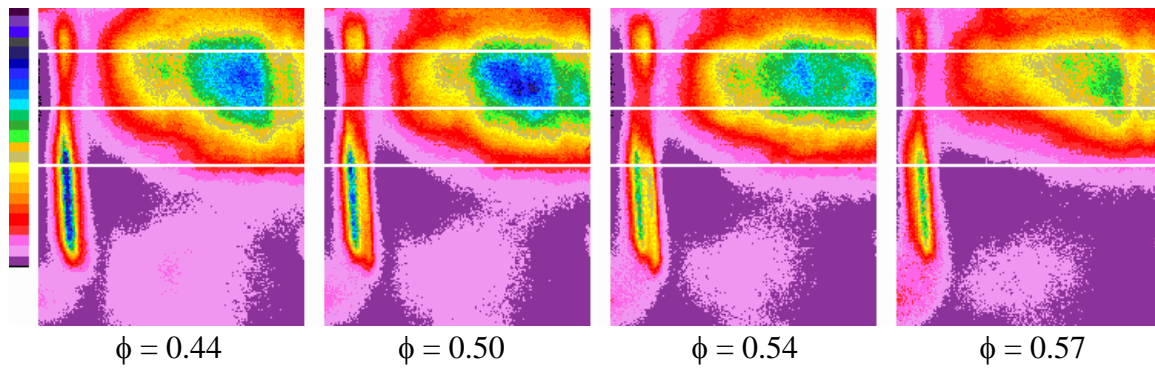


Figure 36. Images showing fuel in the IMFH jet region in configuration A for different equivalence ratios using a vertical laser sheet positioned at $x = 0$ mm. Non-resonant excitation at 283.873 nm. $T_3 = 1040$ F, $P_3 = 9$ atm. Plots show the average across-jet (transverse) cross section for each image.

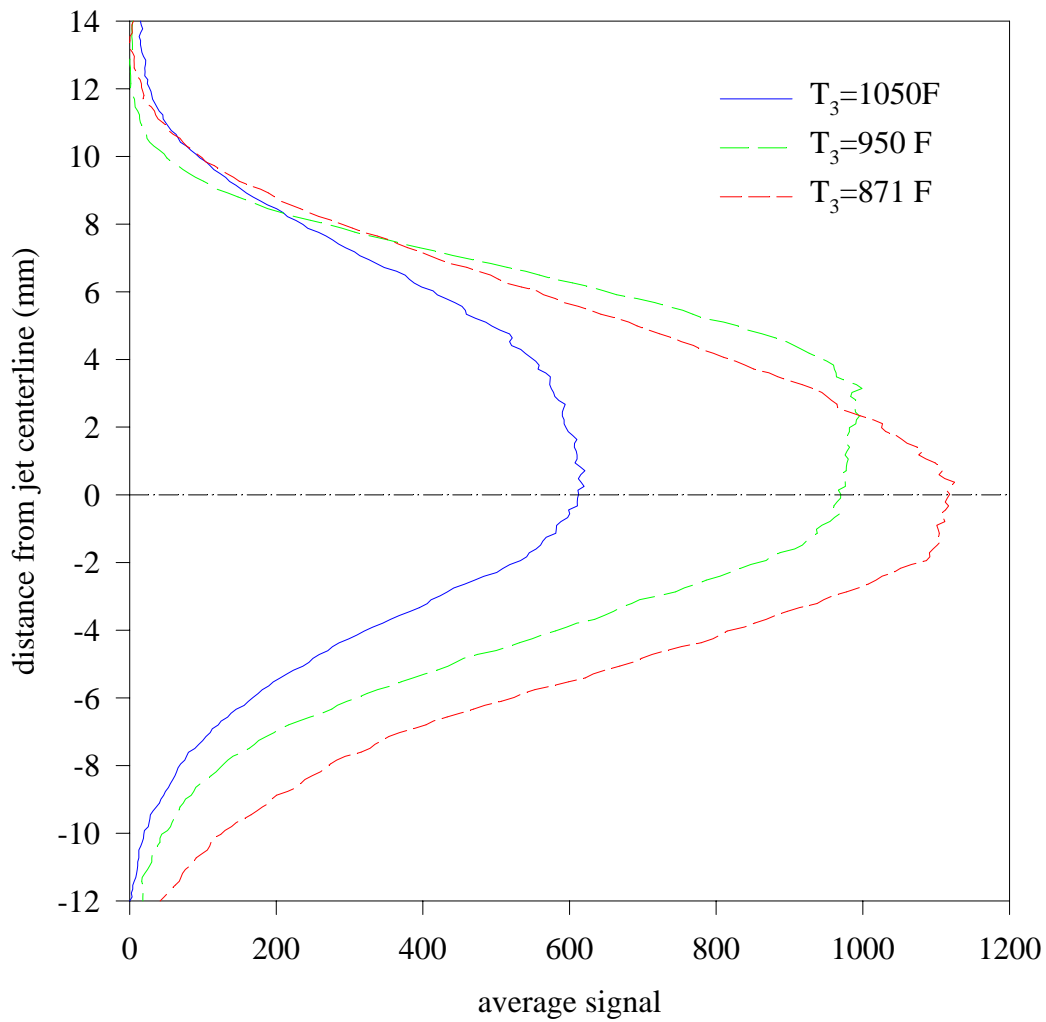
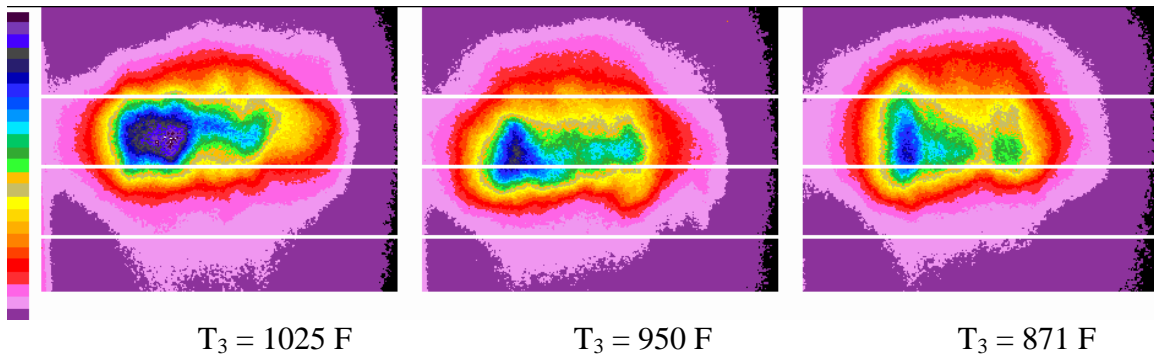


Figure 37. Images showing fuel in the IMFH jet region in configuration B for different inlet temperatures using a vertical laser sheet positioned at $x = -10 \text{ mm}$. Laser excitation is $R_1(12)$, $P_3 = 10.2 \text{ atm}$, and $\phi = 0.44$. Plots show the average across-jet (transverse) cross section for each image.

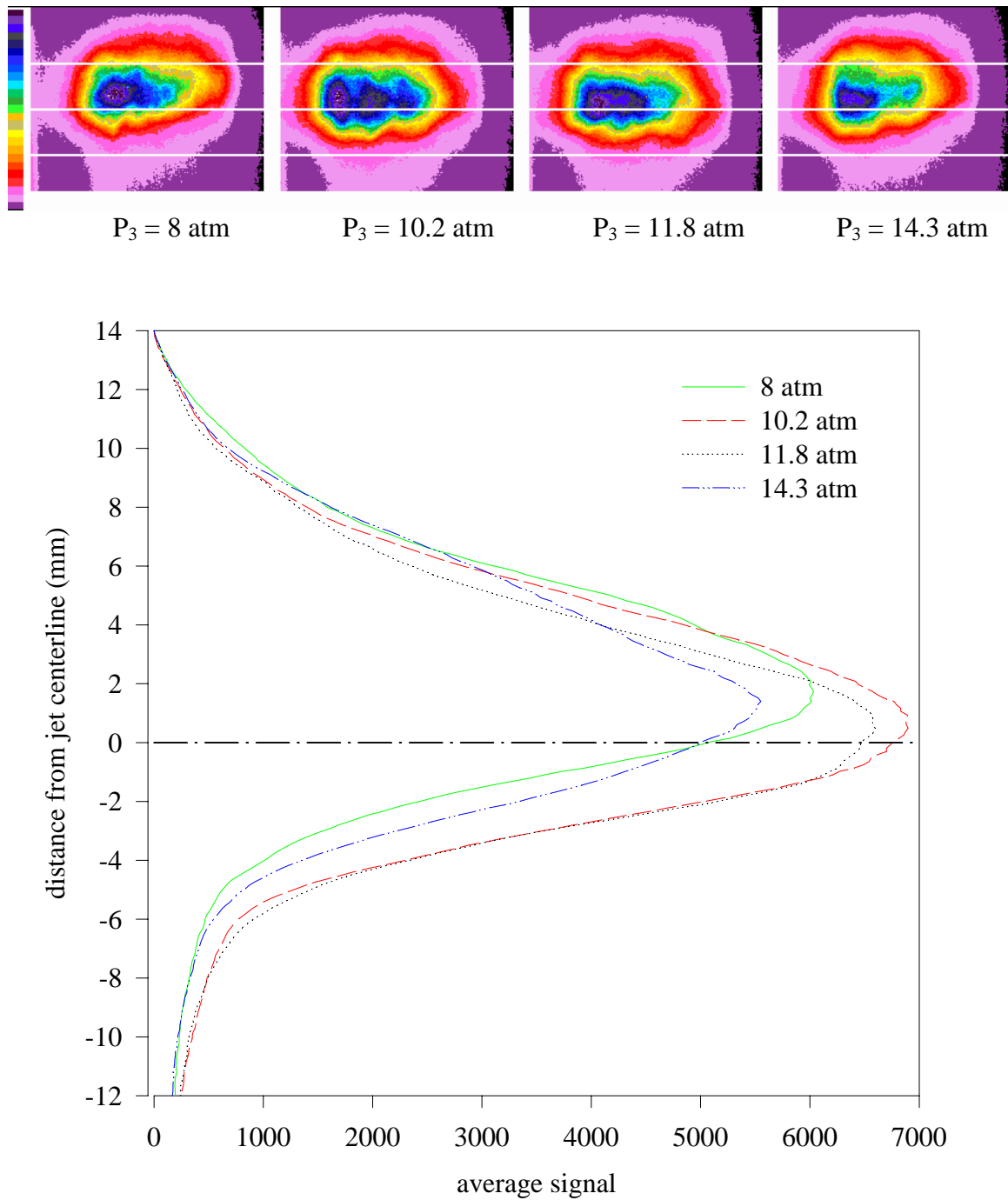


Figure 38. Images showing fuel in the IMFH jet region in configuration B for different inlet pressures using a vertical laser sheet positioned at $x = -10 \text{ mm}$. Laser excitation is $R_1(12)$, $T_3 = 871 \text{ F}$, and $\phi = 0.515$. Plots show the average across-jet (transverse) cross section for each image.

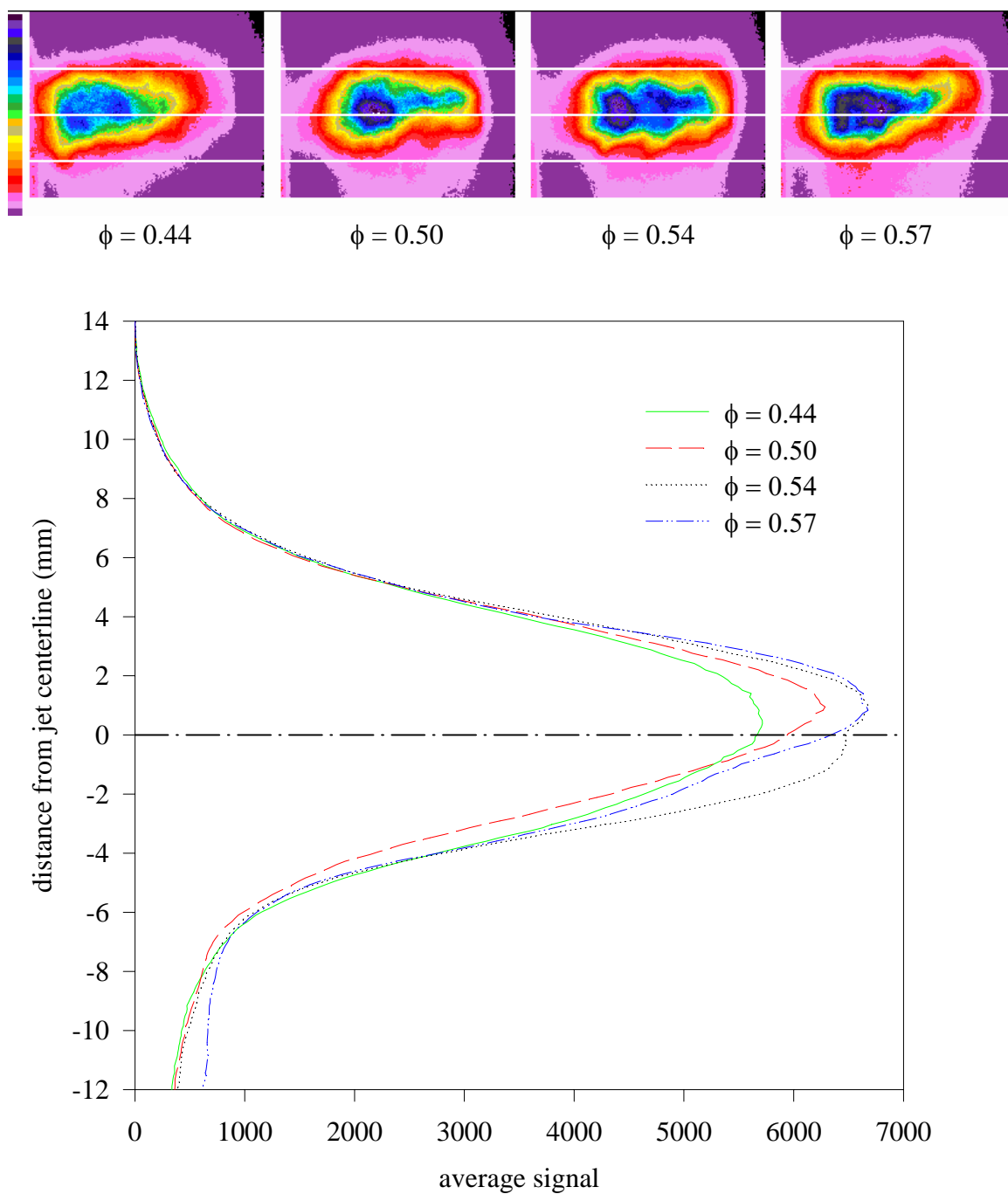


Figure 39. Images showing fuel in the IMFH jet region in configuration B for different equivalence ratios using a vertical laser sheet positioned at $x = -10$ mm. Laser excitation is $R_1(12)$, $T_3 = 1020$ F, and $P_3 = 9$ atm. Plots show the average across-jet (transverse) cross section for each image.

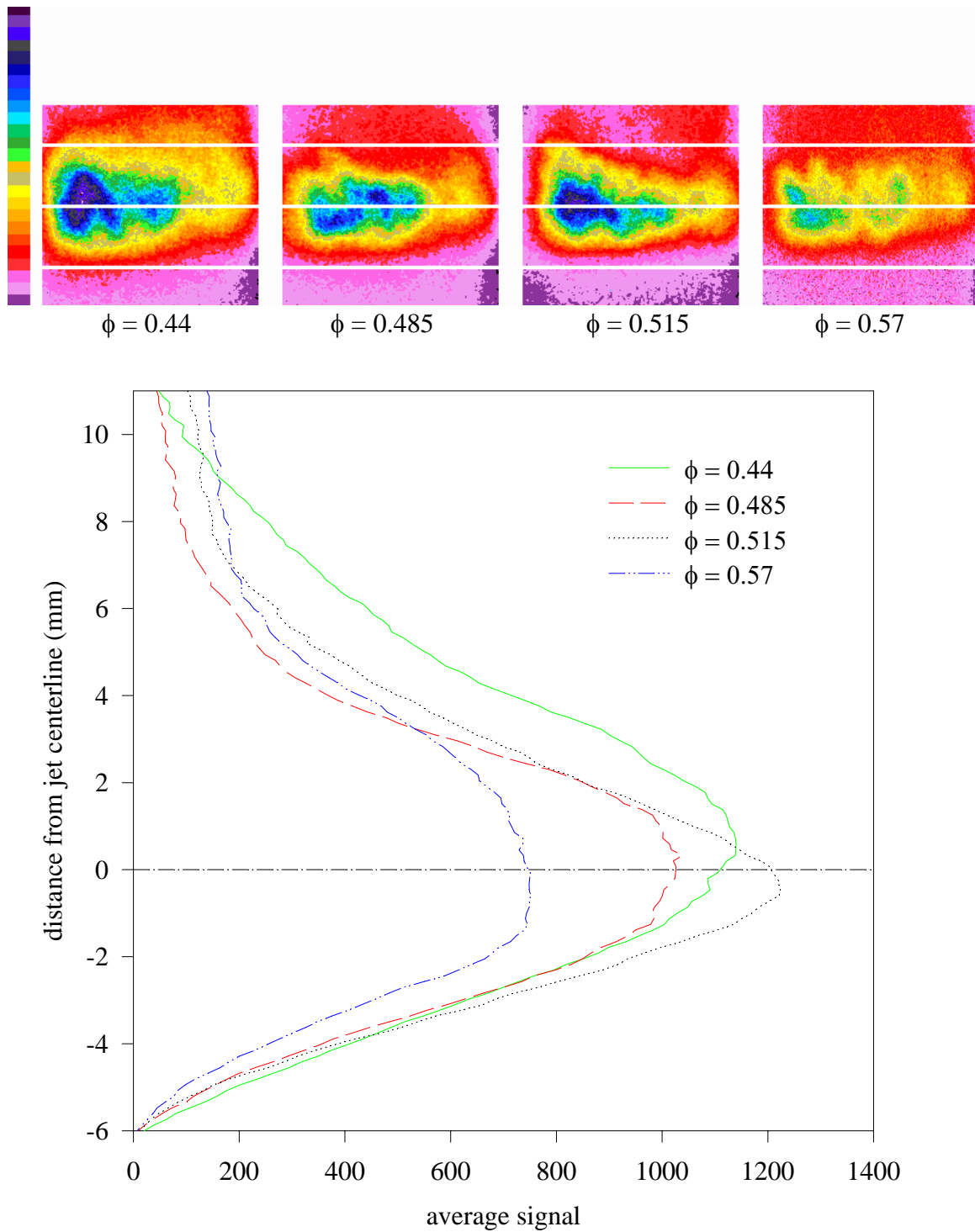


Figure 40. Images showing fuel in the IMFH jet region for different equivalence ratios in dome configuration C using a vertical laser sheet positioned at $x = +5$ mm. The area imaged spans 2.9 - 4.3 diameters downstream of a center dome injector exit. Laser excitation is $R_1(12)$, $T_3 = 870$ F, $P_3 = 14.3$ atm. Plots show the average across-jet (transverse) cross section for each image.

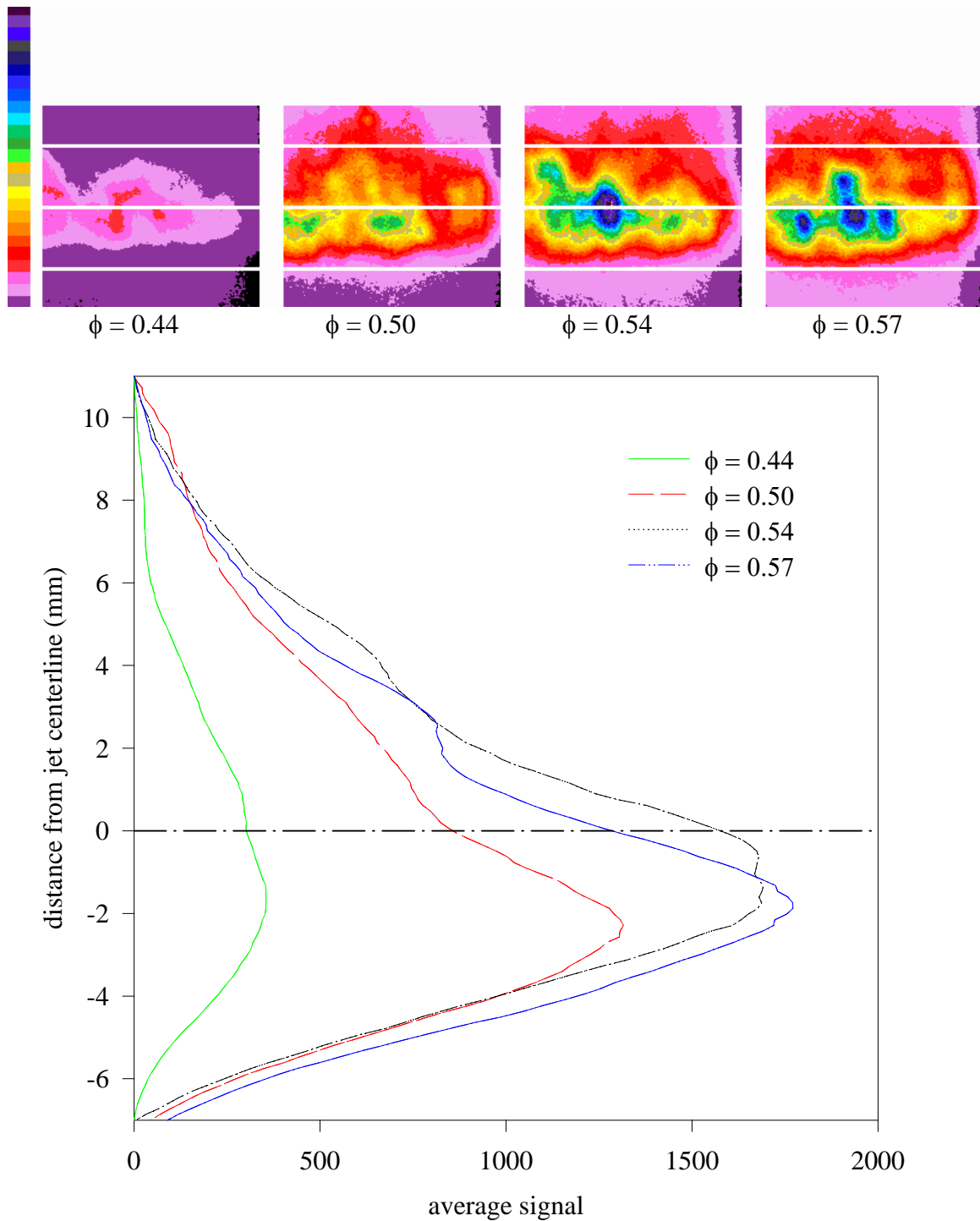


Figure 41. Images showing fuel in the IMFH jet region for different equivalence ratios in dome configuration C using a vertical laser sheet positioned at $x = +5$ mm. The area imaged spans 2.9 - 4.3 diameters downstream of a center dome injector exit. Laser excitation is $R_1(12)$, $T_3 = 1050$ F, $P_3 = 9$ atm. Plots show the average across-jet (transverse) cross section for each image.

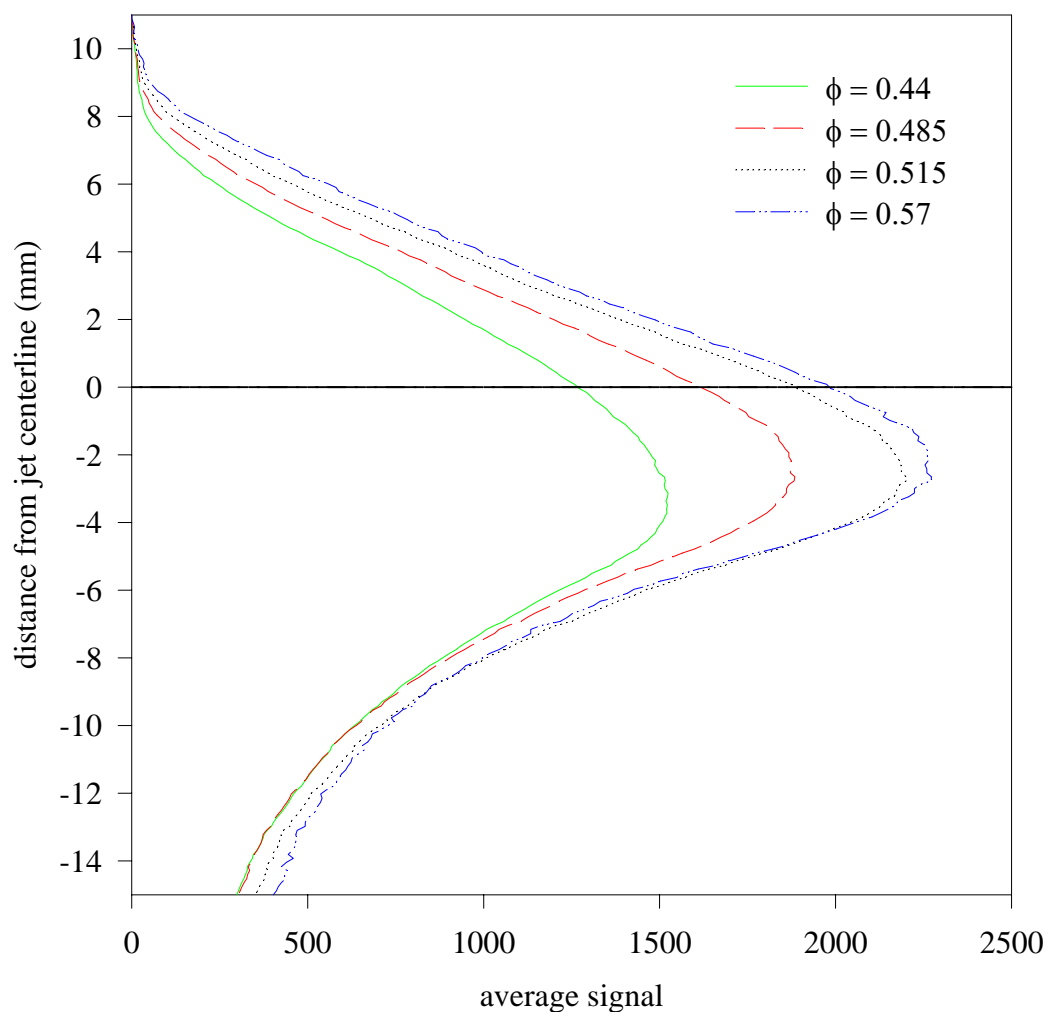
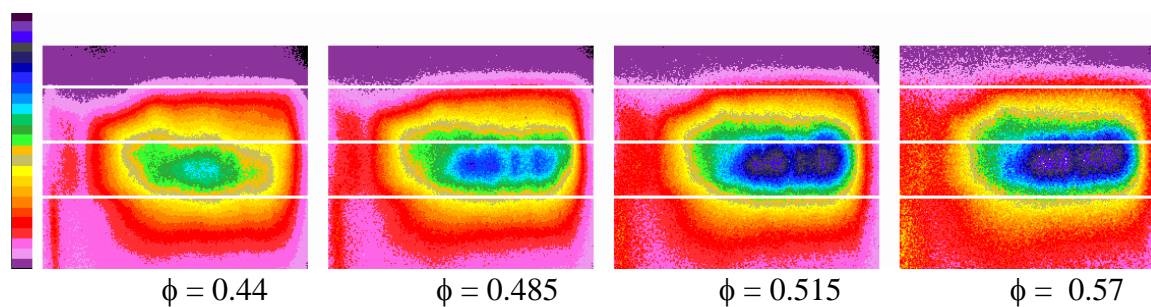


Figure 42. Images showing fuel in the IMFH jet region (top dome) in configuration D for different equivalence ratios using a vertical laser sheet positioned at $x = +20$ mm. Laser excitation is $Q_1(9)$, $T_3 = 870$ F, $P_3 = 14.3$ atm. Plots show the average across-jet (transverse) cross section for each image.

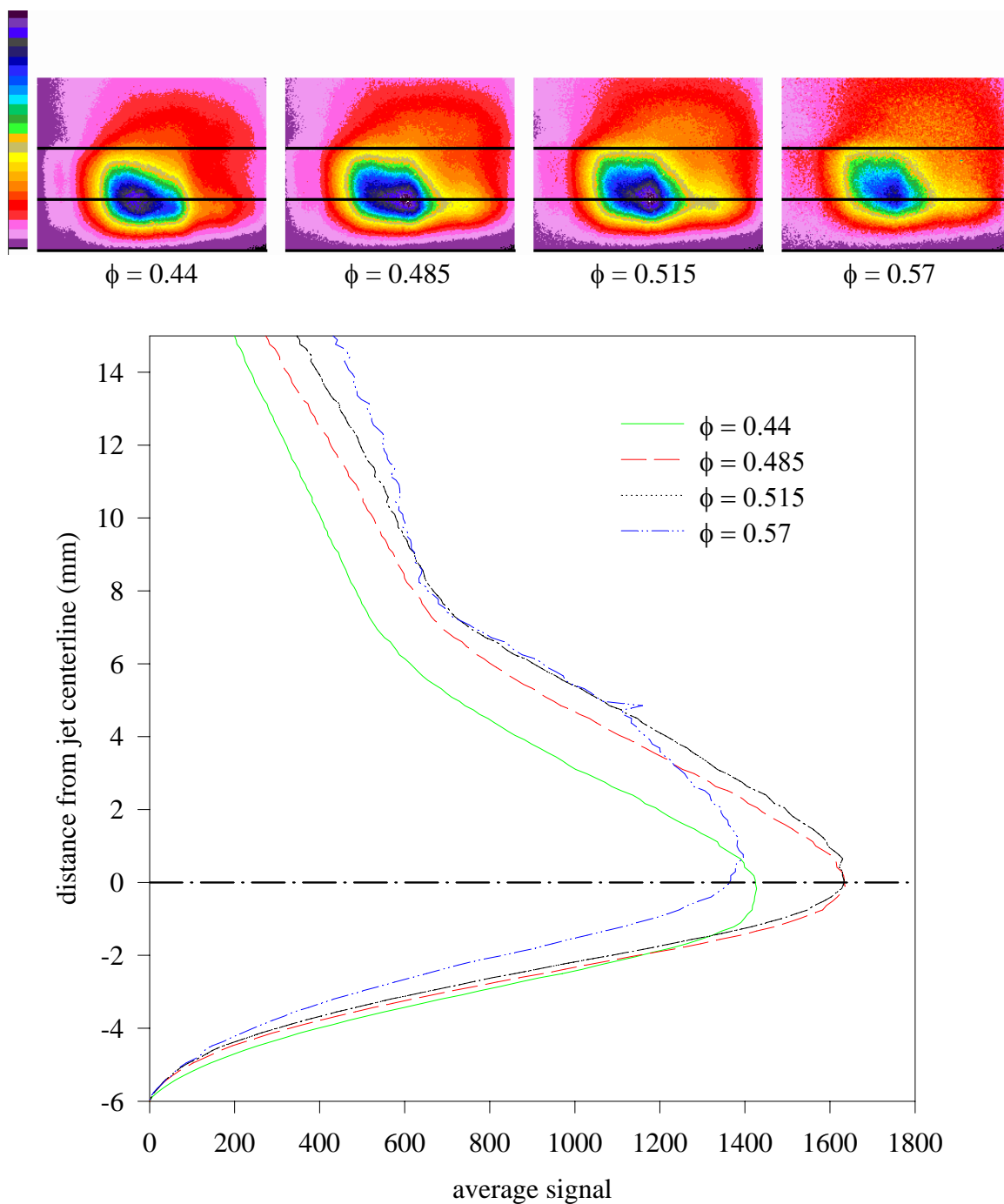


Figure 43. Images showing fuel in the IMFH jet region (center dome) in configuration D for different equivalence ratios using a vertical laser sheet positioned at $x = +20$ mm. Laser excitation is $Q_1(9)$, $T_3 = 870$ F, $P_3 = 14.3$ atm. Plots show the average across-jet (transverse) cross section for each image.

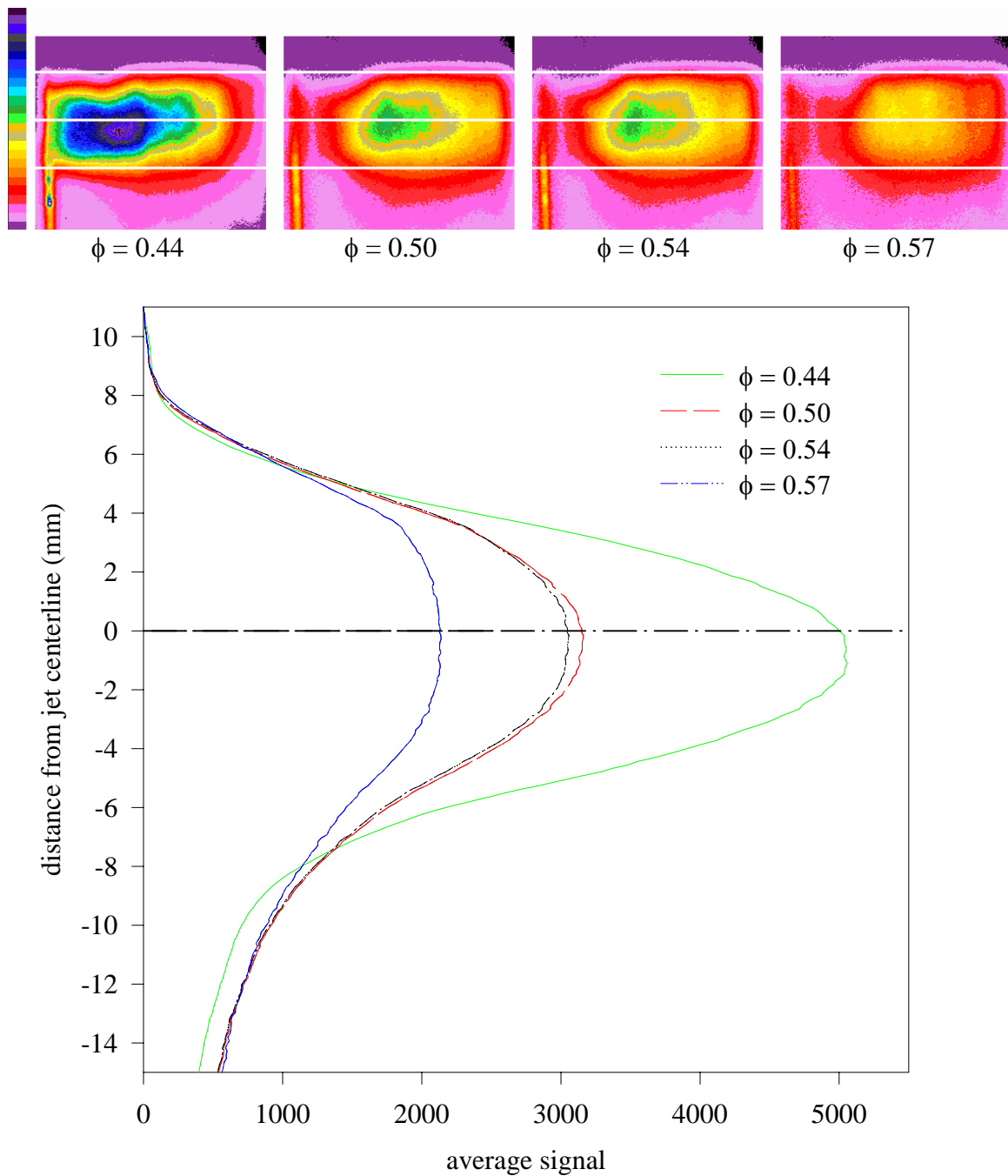


Figure 44. Images showing fuel in the IMFH jet region (top dome) in configuration D for different equivalence ratios using a vertical laser sheet positioned at $x = +20$ mm. Laser excitation is $Q_1(9)$, $T_3 = 1040$ F, $P_3 = 9$ atm. Plots show the average across-jet (transverse) cross section for each image.

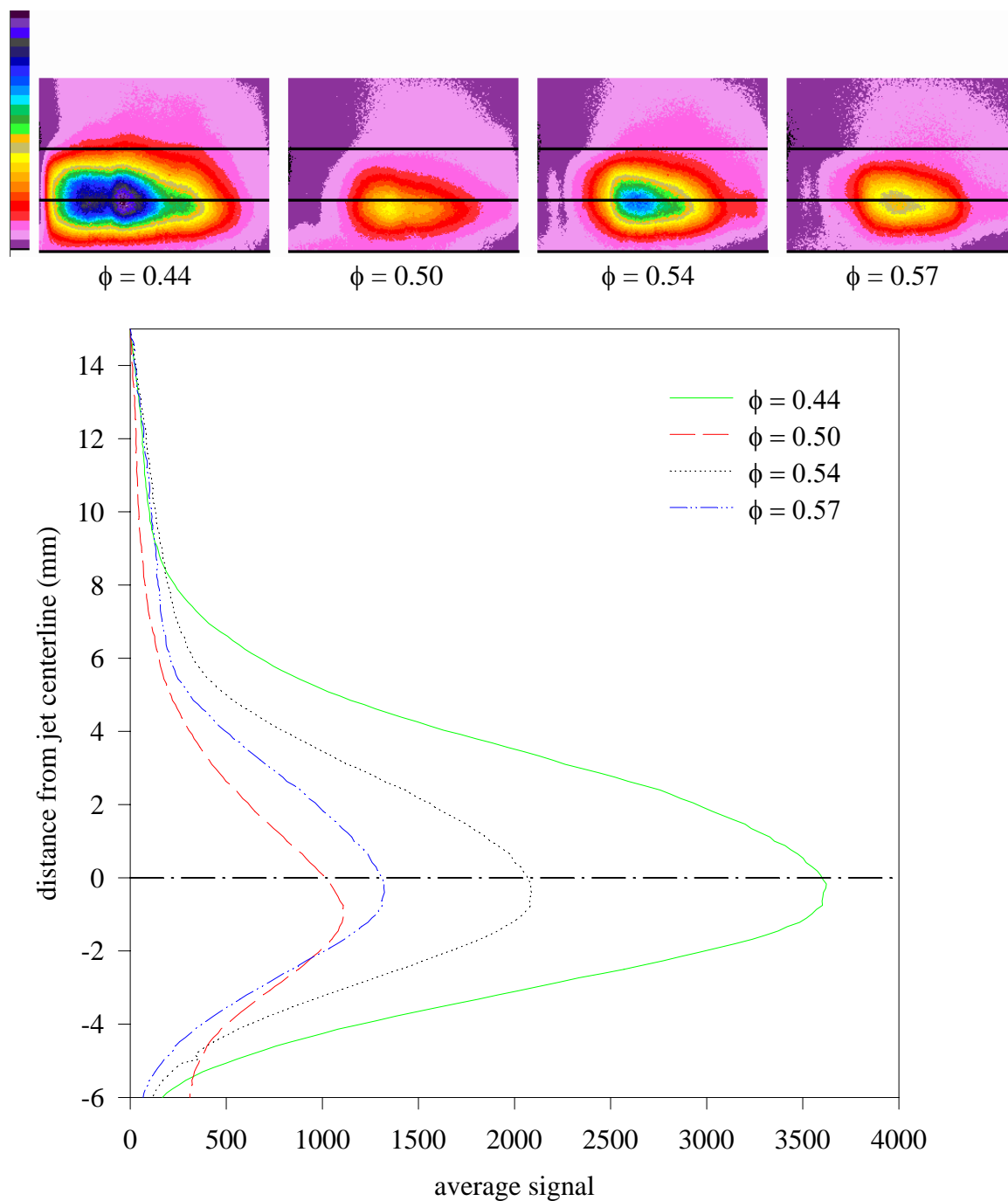


Figure 45. Images showing fuel in the IMFH jet region (center dome) in configuration D for different equivalence ratios using a vertical laser sheet positioned at $x = +10$ mm. Laser excitation is $Q_1(9)$, $T_3 = 1040$ F, $P_3 = 9$ atm. Plots show the average across-jet (transverse) cross section for each image.

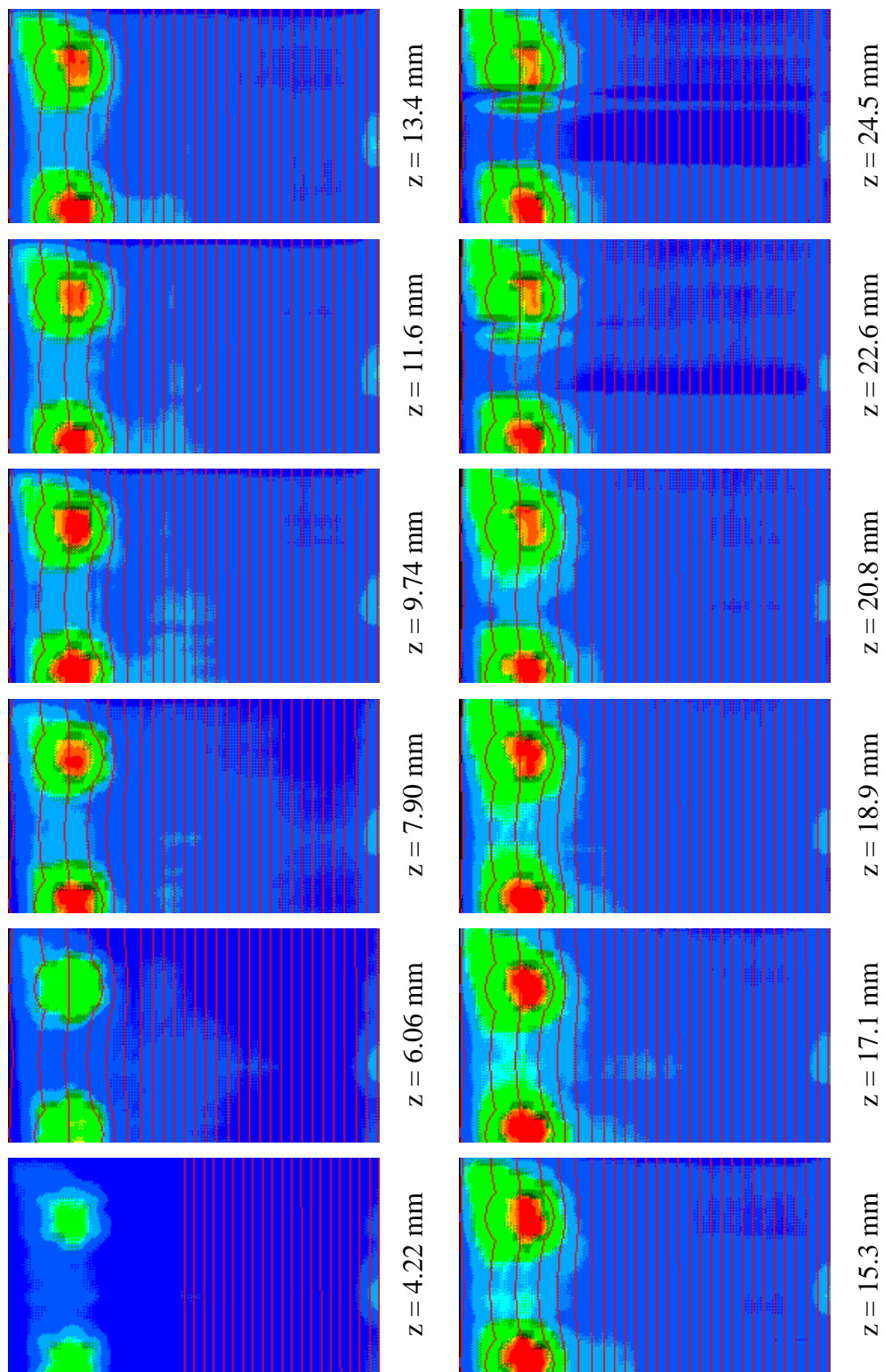


Figure 46. Images showing the fuel distribution in the x-y plane at different distances downstream from the IMFH injector exit plane. $T_3 = 1040\text{F}$, $P_3 = 9\text{ atm}$, $\phi = 0.44$, laser excitation is $Q_1(7)$.

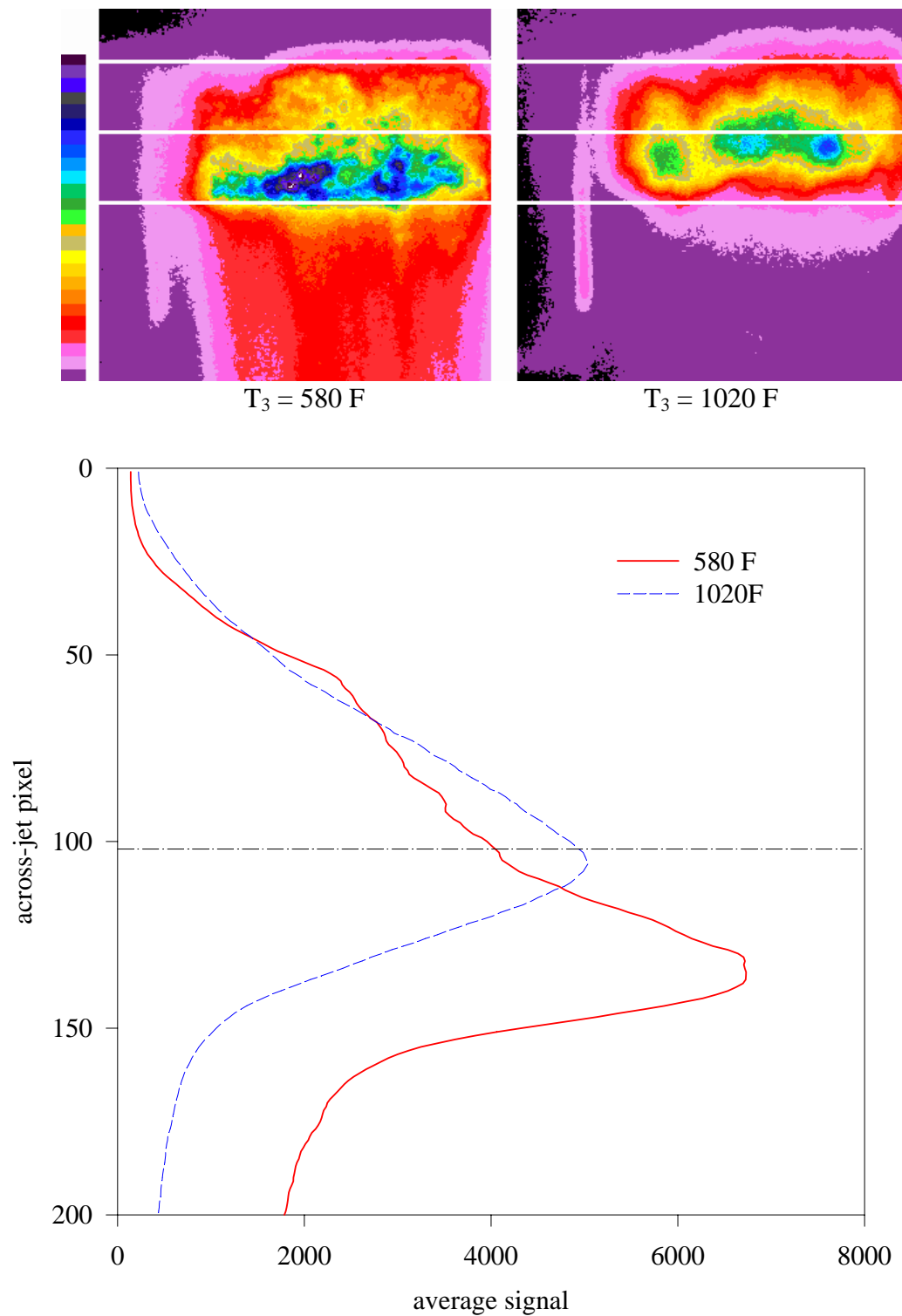


Figure 47. Images showing fuel in the IMFH jet regions for different inlet temperatures in the top dome of configuration C using a vertical laser sheet positioned at $x = +15 \text{ mm}$. Laser excitation is $R_1(12)$, $P_3 = 9 \text{ atm}$, and the equivalence ratio is 0.44.

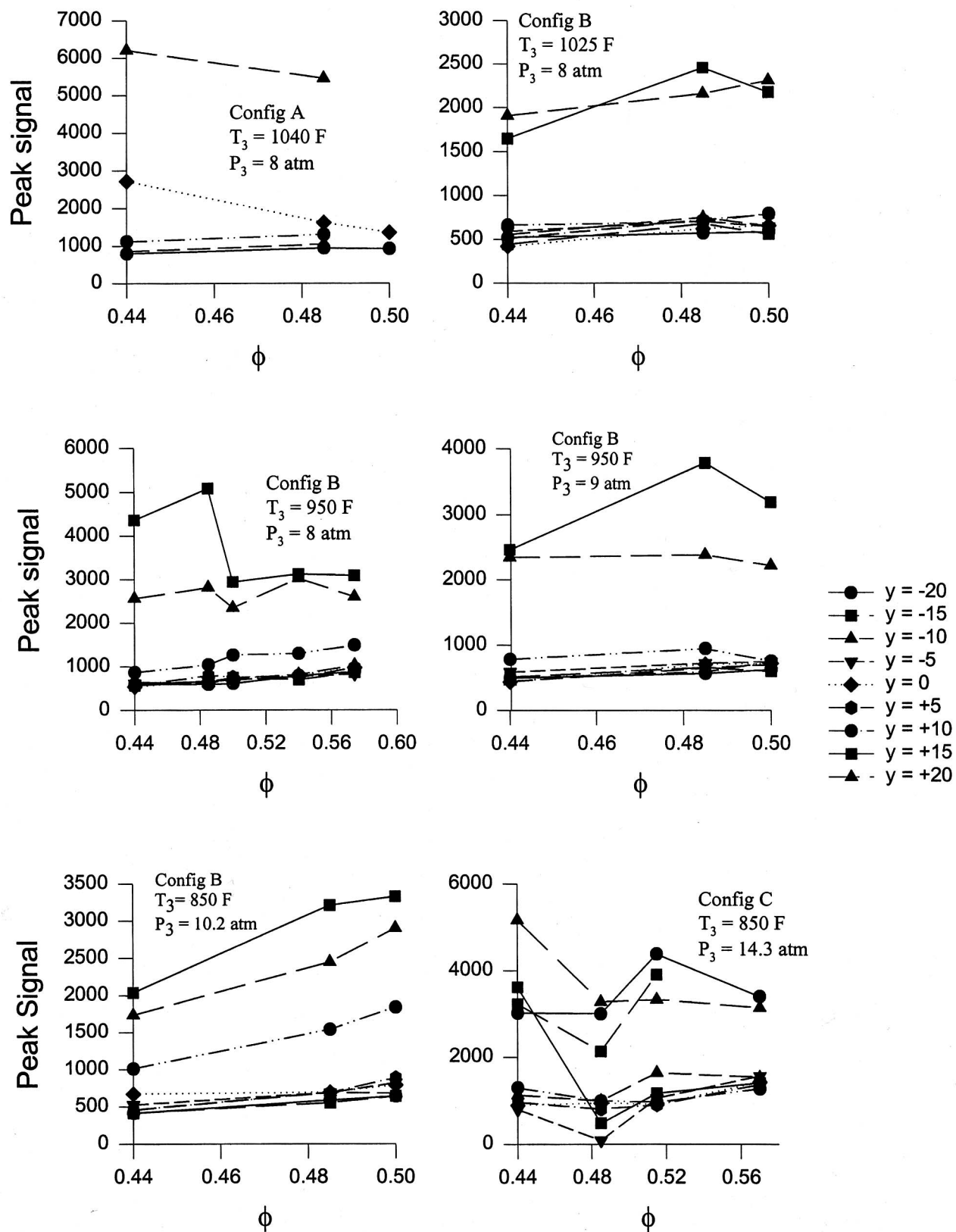


Figure 48. Representative plots of fluorescence signal from horizontal laser sheets as a function of equivalence ratio and position for dome configurations A, B, and C.

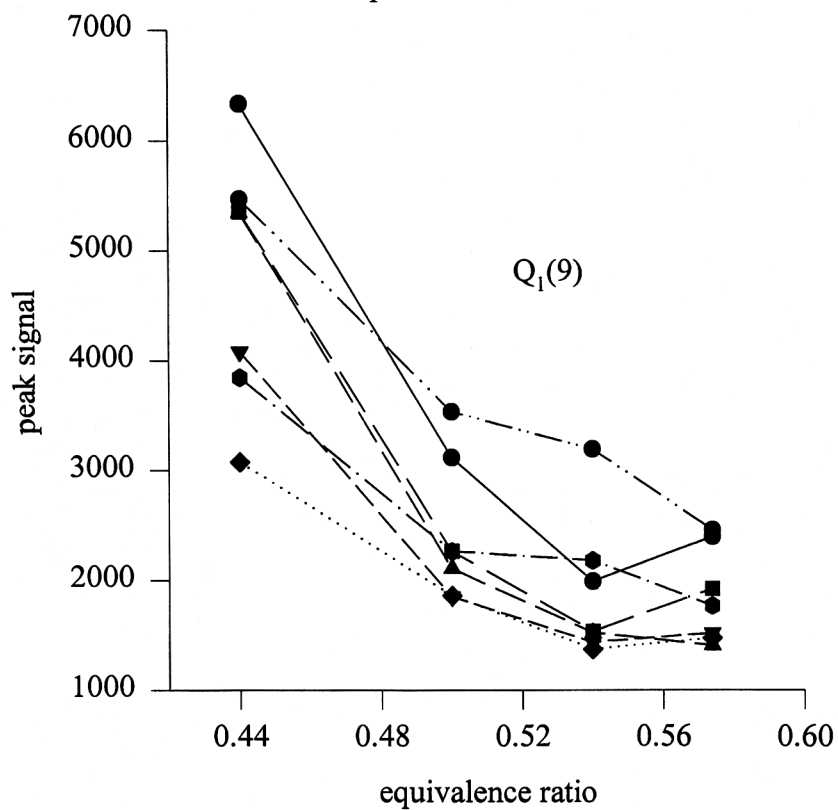
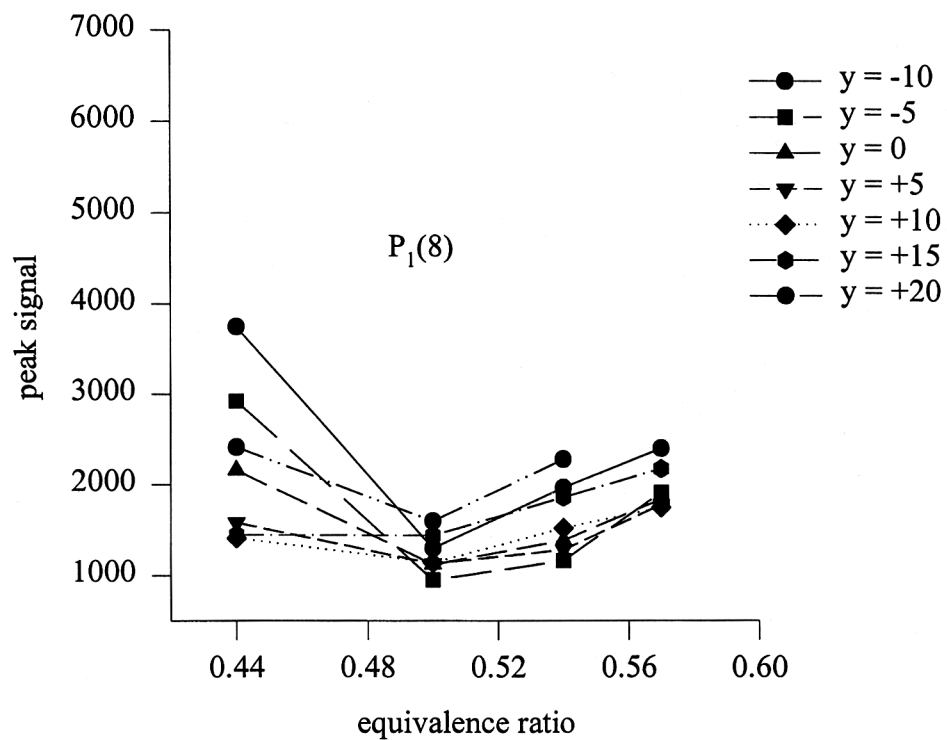


Figure 49. Fluorescence signal vs. equivalence ratio the triple IMFH "flush" configuration using a horizontal laser sheet. $T_3 = 935$ F and $P_3 = 8.1$ atm.

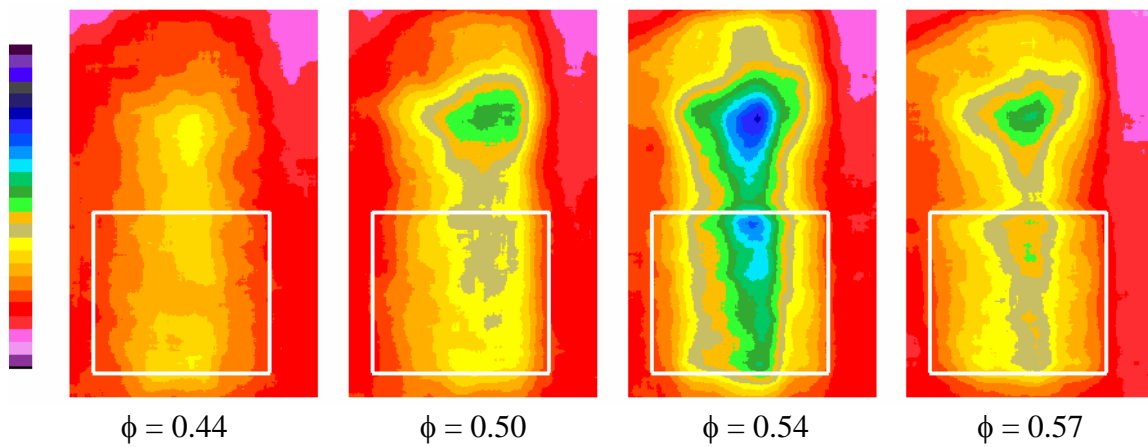


Figure 50. Comparison of NO PLIF images for different equivalence ratios in dome configuration A using a vertical laser sheet. $T_3 = 833\text{K}$, $P_3 = 9\text{ atm}$. Laser excitation is at 225.386 nm

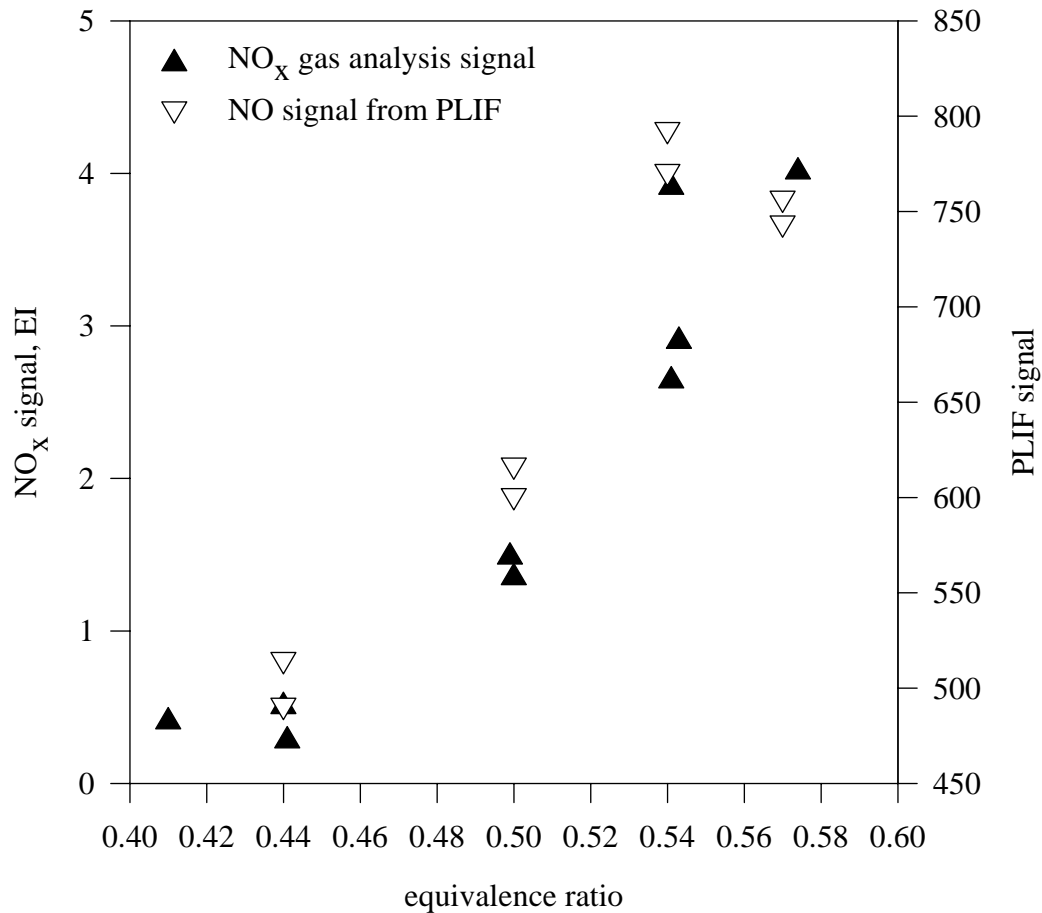


Figure 51. Plots of the NO PLIF and gas sample NO_x signals taken in dome configuration A. $T_3 = 833\text{K}$, $P_3 = 9\text{ atm}$.

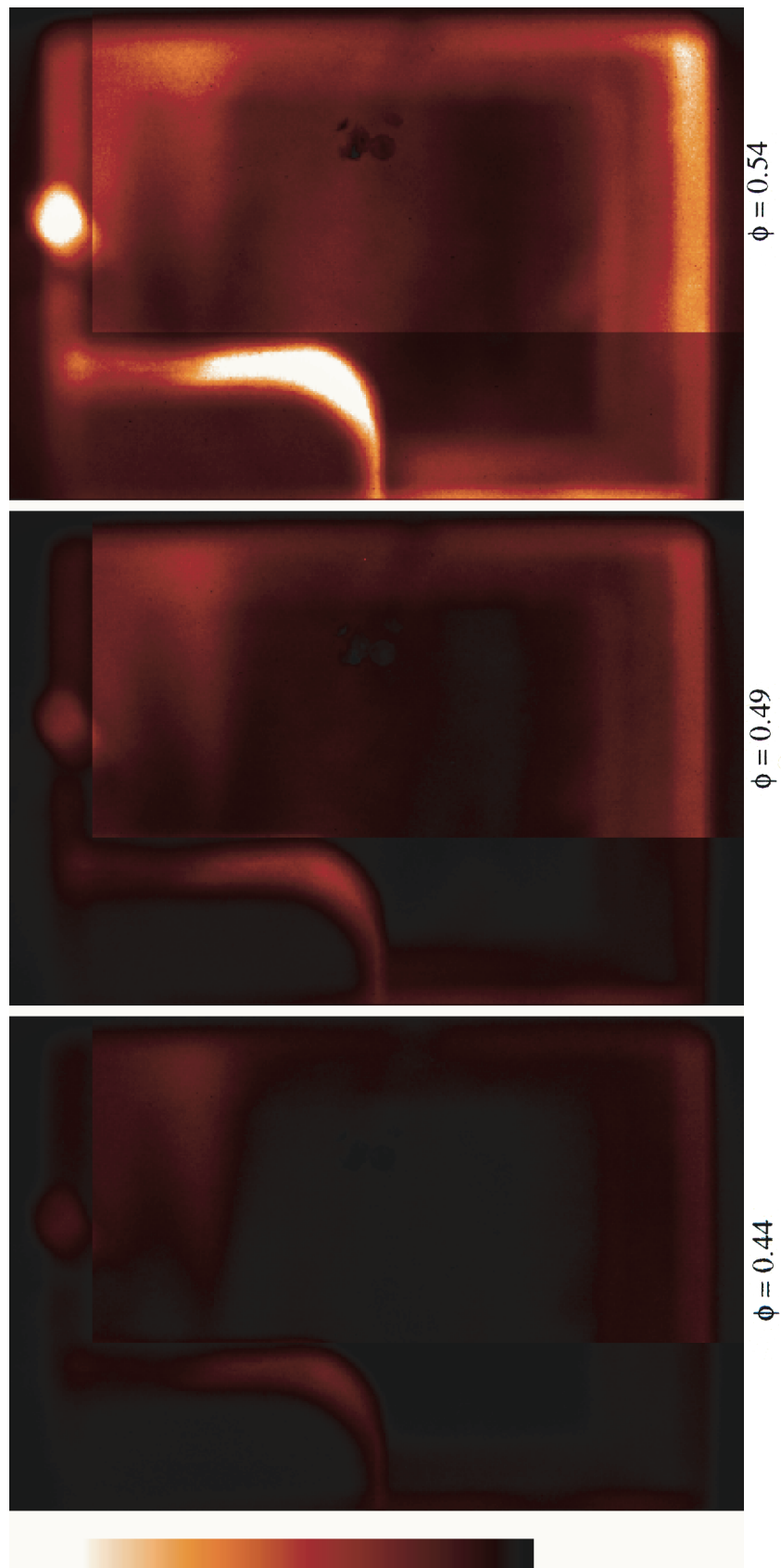


Figure 52. Images from the 3-cup stepped configuration that show naturally occurring fluorescence from C_2 . Light was collected at $\lambda = 532$ nm. $T_3 = 1040$ F, $P_3 = 9.1$ atm.

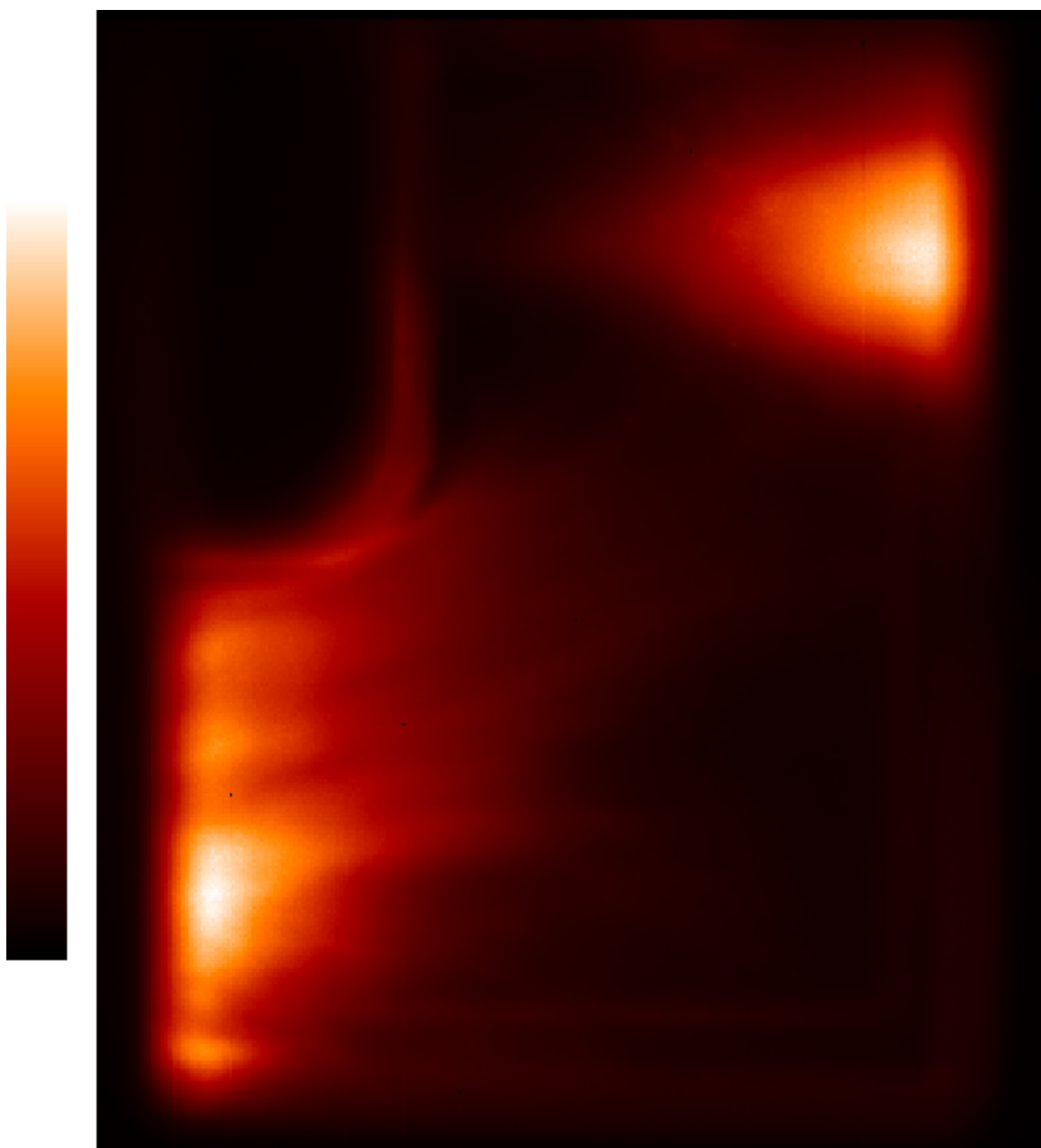


Figure 53. Image from the 3-cup stepped configuration showing naturally occurring fluorescence from C_2 . The image was taken just after combustor lightoff. Light was collected at $\lambda = 532\text{nm}$. $T_3 = 1040\text{ F}$, $P_3 = 9.1\text{ atm}$.

REPORT DOCUMENTATION PAGE			Form Approved OMB No. 0704-0188	
Public reporting burden for this collection of information is estimated to average 1 hour per response, including the time for reviewing instructions, searching existing data sources, gathering and maintaining the data needed, and completing and reviewing the collection of information. Send comments regarding this burden estimate or any other aspect of this collection of information, including suggestions for reducing this burden, to Washington Headquarters Services, Directorate for Information Operations and Reports, 1215 Jefferson Davis Highway, Suite 1204, Arlington, VA 22202-4302, and to the Office of Management and Budget, Paperwork Reduction Project (0704-0188), Washington, DC 20503.				
1. AGENCY USE ONLY (Leave blank)		2. REPORT DATE March 2005		3. REPORT TYPE AND DATES COVERED Technical Memorandum
4. TITLE AND SUBTITLE Laser-Based Flowfield Imaging in a Lean Premixed Prevaporized Sector Combustor			5. FUNDING NUMBERS WBS-22-714-09-46	
6. AUTHOR(S) Yolanda R. Hicks, Randy J. Locke, and Robert C. Anderson				
7. PERFORMING ORGANIZATION NAME(S) AND ADDRESS(ES) National Aeronautics and Space Administration John H. Glenn Research Center at Lewis Field Cleveland, Ohio 44135-3191			8. PERFORMING ORGANIZATION REPORT NUMBER E-14909	
9. SPONSORING/MONITORING AGENCY NAME(S) AND ADDRESS(ES) National Aeronautics and Space Administration Washington, DC 20546-0001			10. SPONSORING/MONITORING AGENCY REPORT NUMBER NASA TM-2005-213402	
11. SUPPLEMENTARY NOTES This research was originally published internally as HSR051 in February 1997. Yolanda R. Hicks and Robert C. Anderson, NASA Glenn Research Center; and Randy J. Locke, NYMA, Inc., Brook Park, Ohio 44142 (presently with QSS Group, Inc., Cleveland, Ohio 44135). Responsible person, Diane Chapman, Ultra-Efficient Engine Technology Program Office, NASA Glenn Research Center, organization code PA, 216-433-2309.				
12a. DISTRIBUTION/AVAILABILITY STATEMENT Unclassified - Unlimited Subject Categories: 07 and 35 Available electronically at http://gltrs.grc.nasa.gov This publication is available from the NASA Center for AeroSpace Information, 301-621-0390.			12b. DISTRIBUTION CODE	
13. ABSTRACT (Maximum 200 words) OH and fuel planar laser-induced fluorescence (PLIF) is used qualitatively in this study to observe the flame structure resultant from different fuel injector dome configurations within the 3-cup sector combustor test rig. The fluorescence images are compared with some computational fluid dynamics (CFD) results. Interferences in obtaining OH fluorescence signals due to the emission of other species are assessed. NO PLIF images are presented and compared to gas analysis results. The comparison shows that PLIF NO can be an excellent method for measuring NO in the flame. Additionally, we present flow visualization of the molecular species C ₂ .				
14. SUBJECT TERMS Laser induced fluorescence; In situ measurement; Combustion physics; Laser applications; Turbojet engines			15. NUMBER OF PAGES 73	
			16. PRICE CODE	
17. SECURITY CLASSIFICATION OF REPORT Unclassified	18. SECURITY CLASSIFICATION OF THIS PAGE Unclassified	19. SECURITY CLASSIFICATION OF ABSTRACT Unclassified	20. LIMITATION OF ABSTRACT	

